IDŐJÁRÁS

QUARTERLY JOURNAL
OF THE HUNGARIAN METEOROLOGICAL SERVICE

CONTENTS

VOL. 121 * NO. 3 * JULY – SEPTEMBER 2017

IDŐJÁRÁS

Quarterly Journal of the Hungarian Meteorological Service

Editorial Office: Kitaibel P.u. 1, H-1024 Budapest, Hungary
P.O. Box 38, H-1525 Budapest, Hungary
E-mail: journal.idojaras@met.hu
Fax: (36-1) 346-4669

Indexed and abstracted in Science Citation Index Expanded™ and Journal Citation Reports/Science Edition
Covered in the abstract and citation database SCOPUS®
Included in EBSCO's databases

Subscription by mail:
IDŐJÁRÁS, P.O. Box 38, H-1525 Budapest, Hungary
E-mail: journal.idojaras@met.hu

IDŐJÁRÁS

Quarterly Journal of the Hungarian Meteorological Service
Vol. 121, No. 3, July – September, 2017, pp. 209–241

Satellite retrieval of severe storms based on the cloud microphysical profile over Central Europe

Michal Pokorny* and **Michal Zak**

Faculty of Mathematics and Physics, Charles University,
V Holesovickach 2, Prague 8, 180 00, Czech Republic

**Corresponding author E-mail: mich.pok@seznam.cz*

(Manuscript received in final form August 31, 2016)

Abstract—The analysis of profiles of temperature (*T*) with regard to the effective radius (*re*) of cloud particles shows the vertical distribution of the effective particle size in clouds. The profiles are computed and constructed from satellite retrieved data and show graphically the distribution of the cloud particle size focused on convective clouds and convective storms subsequently. This special technique of severe storm analysis and forecasting, developed by *Rosenfeld et al.* (1998), has been tested in several countries around the world. Forecasting and predicting dangerous phenomena such as hailstorms or tornadoes that occur in severe storms is the main objective of this technique. This nowcasting tool is now also being tested in Central Europe for the first time. The basic description of the theory is presented in this paper including the results of our research, which confirms application of the theory in Central Europe in severe storm nowcasting. One typical severe and one nonsevere storm event in the Czech Republic and their vicinity are selected and described to show the main difference of *T-re* profiles in distinguishing of severe weather forecast. Furthermore, this paper discusses the possible benefits of this method for the Czech Weather Service, because it clearly reveals severe storm development in the monitored area.

Key-words: *T-re* profiles, severe storm, cloud particles, satellite observation, storm nowcasting

1. Introduction

Severe convective storms occur over Central Europe mostly in the warm season, and in some regions their reports become more frequent every year (*Holzer*, 2001; *Horváth* and *Geresdi*, 2003; *Tolasz et al.*, 2007; *Dotzek et al.*, 2009). The accompanying phenomena of convective storms represent a big hazard, and it is evident that Europeans are affected by severe convective weather hazards as well (*Doswel*, 2014).

Every year, tornadoes are detected in Central Europe (*Dotzek*, 2003). There is a clear increase in tornado frequency from the past to present (*Brázdil et al.*, 2012). The highest frequency of tornado reports in the Czech Republic is in the summer half of the year (June-August): 65.7%. Tornado may cause serious regional or local damage or even number of casualties. These events connected to convective storms have also hit densely populated regions in the past few years, and thus increased their threat (*Doswel*, 2014).

It is very important to consider the possible impacts on severe weather events such as thunderstorms and tornadoes as the climate on Earth changes (e.g., *Brooks*, 2012). A CAPE increase is expected in the future from climate model simulations, which will lead to more frequent environments favorable for severe storm occurrence (*Brooks*, 2012). Local increases in heavy rain (*Field et al.*, 2012) and severe tornadoes (*Doswel*, 2014) are expected in the future, larger hail reaching the ground may also be expected (*Brooks*, 2012).

It is essential to be able to forecast the possible occurrence and impact of severe weather events. Severe storms must be identified as early as possible to the timely warning issued before the storm hits populated areas. Nowcasting tools play a major role in this matter. Different nowcasting and forecasting methods based on satellite and radar data are used in different countries and a lot of them are under further development. The main feature (and also the main "problem" for the forecasting) of convective storms, however, is their rapid development, small scale, and short life. These features were not so easy to track (*Shiqiang* and *Zhemin*, 2001) using the first generation geostationary satellites 15 years ago. Now, that modern geostationary satellites and radar observations are used, tracking is much easier. Recent multi-spectral satellite capabilities in meteorology (GOES and MSG) can be used to identify the start of glaciation in elevating cloud tops, to augment the techniques by *Roberts* and *Rutledge* (2003). In addition, the sounding capabilities of both satellites can be used to monitor changes in precipitable water and thermodynamic stability (CAPE and CIN) in cloud-free areas prior to storm initiation, and within the near-surface inflow to existing storms (http://www.ssec.wisc.edu/~rabin/paper/eumetsat/paper2_eumetsat.doc).

Current storm nowcasting in the Czech Republic is mostly based on radar and satellite data (both are available every five minutes). Available weather radar data used in Central Europe, e.g., http://radar.bourky.cz/ (2015), reveal only precipitating clouds as they occur. Such data are not able to analyze the pre-storm

environment and cannot provide any specific information as to what dangerous phenomena can occur (if large or small hail or tornadoes). Weather model output refers to a specific time of input data and do not respond to the ongoing atmospheric processes. For nowcasting, they provide only little information. Thus, it is very useful to supplement it with a tool which is able to analyze the above mentioned pre-storm environment and to provide any specification in the field of developing storms before the current systems are able to identify them. Such a tool would provide more time for a forecaster to issue any relevant warning or specific forecast of severe and hazardous weather.

These microphysical characteristics of the pre-storm environment of clouds can now be gained by analyzing the profiles of temperature and the size of cloud particles as introduced by *Rosenfeld* and *Lensky* (1998). These profiles express the effective cloud particle radius (*re*) and temperature (*T*) (*Rosenfeld* and *Lensky*, 1998; *Rosenfeld et al*., 2008), and they indirectly reveal the updraft strength.

A nowcasting tool based on *T-re* profiles has been tested for the Central European region for the first time, and it is expected to improve forecasters' skills. On the basis of good results in several testing processes, it is expected to be confirmed as a new simple auxiliary forecasting tool in the region of Central Europe as well as in the field of dangerous weather event forecasting and other meteorological applications. Its simplicity lies in the use of Meteosat geostationary data in the frame of MSG_RGB software provided by its developer *I. M. Lensky* which was developed especially for the view of *T-re* profiles. The documentation of the software was provided by its developer Lensky in 2009. The main aim of this study is to improve accuracy of severe storm nowcasting so that damage and serious injuries are prevented and life protection is strengthened in Central Europe.

Section 2 describes the origin and basic principles of the applied method, Section 3 mentions the procedure of processing the data. The following part then introduces the profiles of severe and nonsevere situations and conveys more profound analysis of typical severe and nonsevere situations. Setion 4 compares the collected data from both situation types.

2. Method

Rosenfeld and *Lensky* introduced the technique of *T-re* profiles (*T* - particle temperature, *re* - particle effective radius) in forecasting severe storms and their accompanying dangerous phenomena such as hail and tornadoes (*Rosenfeld* and *Lensky*, 2008). This technique was used in different projects (*Rosenfeld et al*., 2006; *Rosenfeld et al*., 2008), and tests were carried out and verified (*Lensky* and *Rosenfeld*, 2006) in several countries (namely Israel, California, Texas, Brazil, and in Africa) with different satellites providing 3.9 or 3.7 μm spectral information. MSG (Meteosat Second Generation) geostationary satellite data

were previously used in *T-re* profiles testing in the Mediterranean Sea area (*Lensky* and *Shiff*, 2007). In addition, other applications of the MSG data in the conditions of Central Europe were applied (*Pfeifer et al*., 2010). MSG data enable to track the evolution of the effective radius of cloud particles with the cloud top temperature by the *T-re* method also in Central Europe. The geostationary satellite MSG provides data scanned from a stable position, which is more useful for the continuous tracking of images compared to polar orbiting satellites. It was decided not to test the data from the polar orbiting satellite due to their irregular time resolution in our territory. There is no need to recalculate MSG data for any other satellite position, which is another big advantage compared to polar orbiting satellites. Another benefit is the frequency of cloud scanning, which is five minutes in the rapid scan mode. MSG has some other advantages for cloud observation such as 12 spectral channels or a higher resolution of images (as good as 1 km). In the region of Central Europe the resolution is lower, approximately 3 km, which is a lower resolution compared to polar orbiting satellites. With the new generation of Meteosat satellites, the resolution will be higher. To analyze the cloud top temperature and the effective radius of cloud particles in this work, the MSG geostationary satellite data and generated *T-re* profiles are applied for the area of Central Europe. The most advantageous procedure is to start the analysis with first convective clouds and track their evolution in consecutive MSG images before they become severe.

2.1. T-re profile principles

The method of *T-re* (*Rosenfeld et al*., 2008) profiles was designed to reveal the microphysical characteristic (*Rosenfeld et al.,* 2008) of severe storm clouds influenced by updraft speed (*Rosenfeld et al.,* 2008). Microphysical vertical profile as a function of temperature or height inside clouds may be explained as follows. Initially, cloud droplets at the bottom of a cloud grow by water vapor diffusion processes, followed by the second zone of collision-coalescence situated above. In the third stage, the droplets have already reached sizes large enough to enable internal precipitation processes. The fourth zone is mixed phase where ice and water coexist and further enhance the growth of droplet efficiency and the droplets grow even faster. The upper glaciated stage, where all the droplets are frozen, is situated above the level of –38 °C (*Rosenfeld et al*., 2008). Each zone has a different slope of the percentile line in *T-re* diagrams, which enables their identification (*Martins et al*., 2007). A more profound interpretation of microphysical layers in clouds and the above mentioned features is provided by *Lensky* and *Rosenfeld* (2005).

We will focus on the *T-re* profile as a graphical tool to reveal the severity of a developing storm (either in one type of airmass or in the vicinity of frontal boundaries) before it reaches the severe stage. Selecting a group of cells intentionally at different stages of development for the creation of *T-re* profiles

indirectly helps to determine the updraft strength inside clouds and to estimate the storm severity subsequently. The vertical updraft speed in clouds is the main factor in distinguishing between stratiform and convective cloud types. In stratiform clouds, the ascending air speed is low, so the cloud particles usually grow to larger sizes at lower levels compared to the situation in deep convective clouds. Conversely, in convective clouds, particles have to overcome the above mentioned updraft strength to fall out of the cloud to become precipitation (*Tokay* and *Short*, 1996). In addition, severe convective storms always produce hazardous weather events, such as tornadoes, hail, damaging wind, and so forth (*Jurkovic et al*., 2015). Such events occur in convective systems entirely due to the updraft motion (*Jurkovic et al*., 2015). Cloud particle size is related to the updraft strength inside convective clouds or storms which are developing within the target area. Thus, the particle size indirectly represents the severity of developing storms. The role of the updraft strength in the formation of severe weather can be explained as follows. The higher speed of the updraft delays the growth of cloud particles to larger sizes and postpones their glaciation. In other words, when there is a strong updraft in a cloud, particles do not have enough time to grow to larger sizes because they ascend through the cloud very quickly upwards. *T-re* profiles obtained and computed from satellite data by the MSG_RGB software indirectly reflect the updraft speed in rapidly growing convective clouds. In the case of vigorous convection, these profiles usually show only small particles near the cloud tops of relevant cumulonimbus clouds compared to nonsevere cases. Typical profiles of severe and nonsevere storms in maritime and continental conditions are provided by *Rosenfeld et al*. (2008).

The MSG_RGB software provides multispectral information on MSG channels for generating *T-re* profiles. The 3.9 μm reflectance determinates the cloud particles size in generated profiles. Smaller cloud particles are revealed by a larger 3.9 μm reflectance. According to some studies, it has been shown that smaller crystals are really effective reflectors near 3.9 μm (e.g., *Melani et al*., 2003). The major hypothesis assumes that such detection of cloud cells with the enhanced 3.9 μm reflectivity due to small cloud particles discloses rapidly developing thunderstorms with a high updraft speed inside clouds.

The *T-re* analysis tool performs all calculations automatically as it was developed to generate *T-re* profiles in a graphical form without any additional calculations. Its main goal is to provide such graphical output that enables quick reaction to the severity of a developing storm. Unfortunately, the software cannot reduce the number of lines in profiles. Nevertheless, the *T-re* method was designed to be as easy and fast as possible.

Because of the 3.9 μm channel features (*Setvák*, 1989), the method is limited to daytime hours only, when solar illumination is available. This limitation is also mentioned by *Jurkovic et al*. (2015). This aspect poses the major deficiency of this tool, because many convective storms keep developing after sunset. After personal communication with Prof. *D. Rosenfeld* in 2015 concerning the issues of

T-re profile method, the limit for solar zenith angle was set to be 65°. In addition, there is no possibility to show country borders in the background of an image for better orientation in the satellite image, which is another disadvantage of the *T-re* method in MSG_RGB software.

In addition, in a recently published study (*Sporre et al*., 2014) from another European region, *T-re* profiles were also used to find cloud particle sizes. This paper focuses on analyzing aerosol effects on convective clouds. However, the detected cloud drop size range corresponded to our data. *Zipori et al*. (2015) have recently used the same technique with the MSG_RGB program (*Lensky* and *Rosenfeld*, 2008) and the satellite data of Meteosat-9 in their study of the effect of aerosol sources on cloud particle size and glaciation temperature. *Jurkovic et al*. (2015) used the MSG 3.9 μm reflectivity for generating the profiles of cloud effective radius and temperature (*T-re*) to describe severe storms characteristics over Central Europe. They applied *Rosenfeld* and *Lensky's* (1998) methodology in Hungary, Germany, Austria, and other countries. *Rosenfeld et al*. (2013) employed the theory of *T-re* profiles (*Rosenfeld* and *Lensky*, 2008) in the study of cloud microstructure. The vertical evolution of cloud microstructure using the above mentioned methodology was also used in warm rain onset height and aerosol optical depth research (*Zhu et al*. 2015). They mentioned some basic rules concerning *T-re* profiles, which are also used in our paper. *Zheng* and *Rosenfeld* (2015) studied the updraft speed in convective clouds according to *Rosenfeld et al*. (2014) and *Zheng et al*. (2015) in another project.

3. Data from T-re profiles

The principles described above were tested on data from the warm part (from May to August) of the years 2005–2013 for the Czech Republic and its vicinity on archive data provided by EUMETSAT. Subsequently, another test was realized on real-time data of the years 2012–2013 for days, when intensive accompanying phenomena of convective storms were expected (forecasted) or reported (for archive data). These data were selected according to the severity of storms; the severity criteria were mainly based on the European Severe Weather Database (ESWD) (http://www.eswd.eu/) operated by the ESSL (European Severe Storms Laboratory). In general, ESWD provides a clear description of severe weather events online (http://www.eswd.eu/cgi-bin/eswd.cgi?action=showdefinitions &lang=en_0) and the list of severe weather event reports online. Similarly, *Jurkovic et al*. (2015) define the warm part of the year as May-September.

52 situations with strong convection or rain occurrence were analyzed. While 33 of those were accompanied by severe attendant phenomena, 17 situations may be classified as nonsevere. From all severe situations, 24 hit the Czech Republic. Subsequently, after detailed analysis of the selected severe and nonsevere situations, a table of tracked values of the *T-re* profiles was compiled (*Table 1*)

and is provided in Section 5. The values of tracked features mentioned below can be simply gained from the numerical listing of temperatures (in 1 °C steps) and the radii related for each percentile line depicted in the *T-re* profile. This is very useful for further computations. Graphically the values could be acquired from the generated *T-re* profiles, which is possible due to the good resolution of the *T-re* profiles. As a matter of fact, *Tl* or *Tg* are the breaking points of the 15th percentile line in the profile, i.e., the vertical coordinate of the 15th percentile line, which makes them easy to recognize in the gained *T-re* profiles. This can mostly be used to make a quick reaction to the severity of a storm.

An analysis of the severe situation data is shown in *Figs. 1a-f* based on satellite data obtained from the EUMETSAT archive and the MSG reception station (situated in the Dept. of Atmospheric Physic, the Faculty of Mathematics and Physics, Charles University, Prague) and processed in the MSG_RGB software (*Lensky*, 2009). An analysis of the nonsevere situation data is shown in *Fig. 2*, which is based on the Severe Storm product. Section Four provides information about collecting the data, *Table 1* in Section Five summarizes the typical features of *re*, *Tl*, *Tg,* and so forth, of selected situations, and *Table 2* provides their statistical processing.

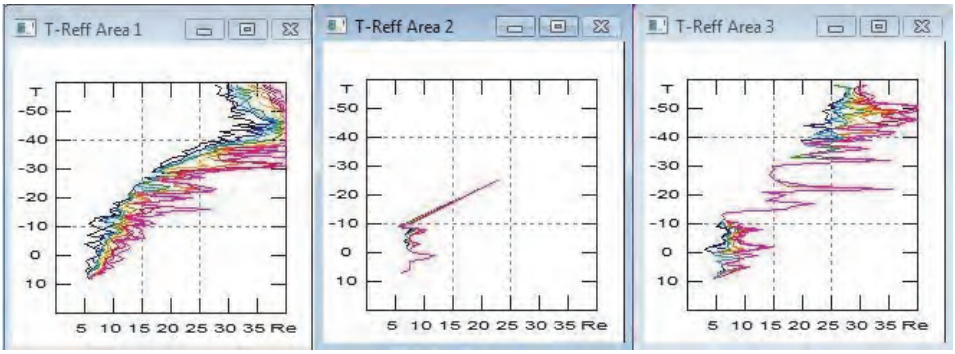

Fig. 1a. Analysis of the situation for 1457 UTC, June 12, 2010

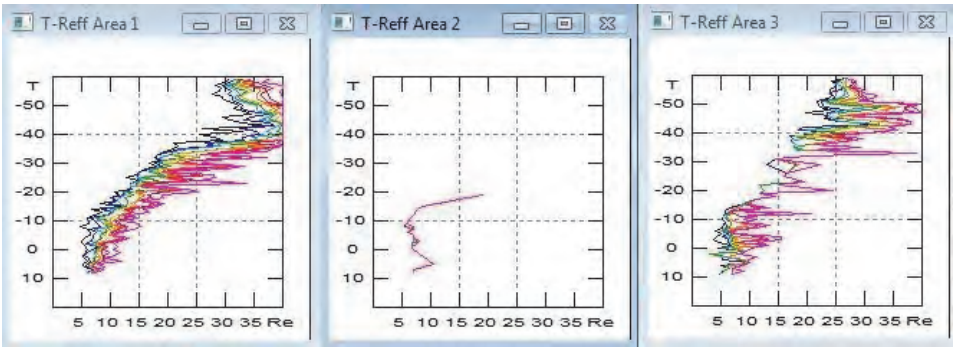

Fig. 1b. The same as *Fig. 1a* but for 1512 UTC, June 12, 2010

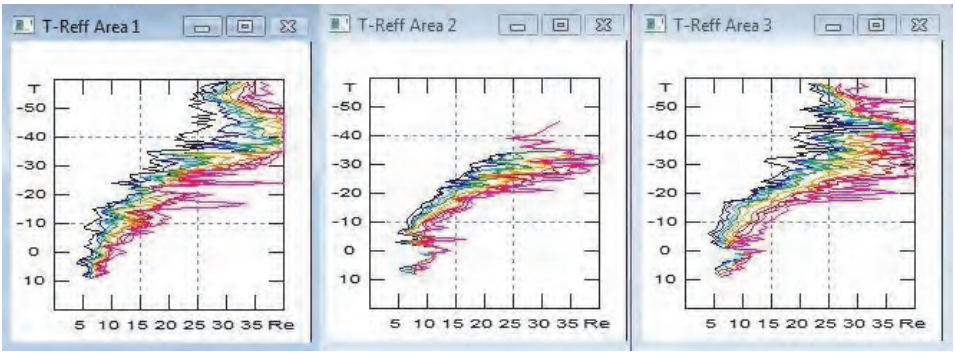

Fig. 1c. The same as *Fig. 1a* but for 1542 UTC, June 12, 2010

Re (μm) – cloud particle radius
T (°C) – temperature of cloud particle
Color lines (black to magenta) in profiles express the 5th to 100th percentiles of effective particle radius in the interval of 1 °C.

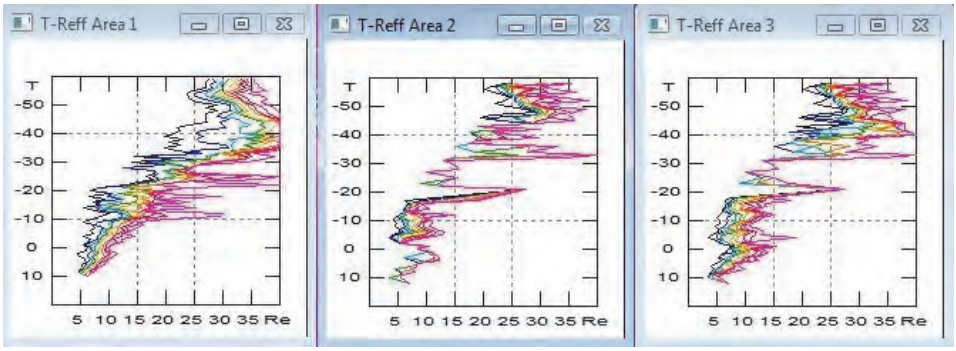

Fig. 1d. The same as *Fig. 1a* but for 1557 UTC, June 12, 2010

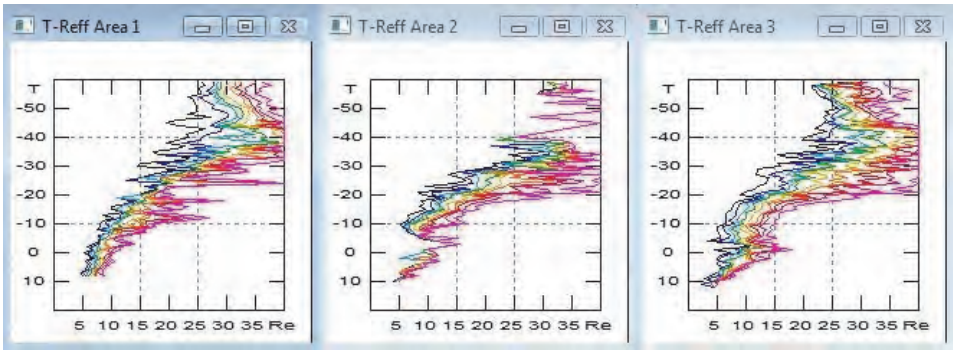

Fig. 1e. The same as *Fig. 1a* but for 1612 UTC. June 12, 2010

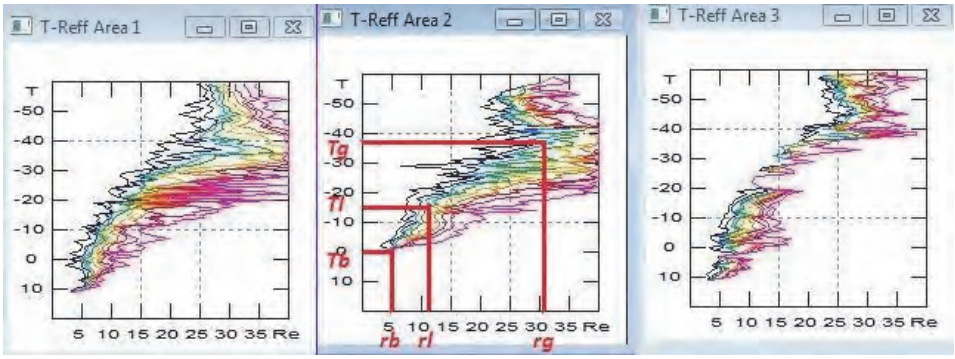

Fig. 1f. The same as *Fig. 1a* but for 1627 UTC. June 12, 2010

Re (μm) – cloud particle radius ; T (°C) – temperature of cloud particle
rb (μm) – cloud particle radius range near the cloud base
rl (μm) – cloud particle radius near the top of the lower linear part of the profile
rg (μm) – temperature of the glaciation phase bottom
Tb (°C) – cloud particle temperature near the cloud base
Tl (°C) – temperature of the top of the lower linear part of the profile, it mostly represents the top of the layer in which the particles grow mostly by diffusional or coalescence growth
Tg (°C) – temperature of the glaciation phase bottom, from this layer, all particles are expected to be frozen, it is the top of the mixed phase layer
Color lines (black to magenta) in profiles express the 5th to 100th percentiles of effective particle radius in the interval of 1 °C.

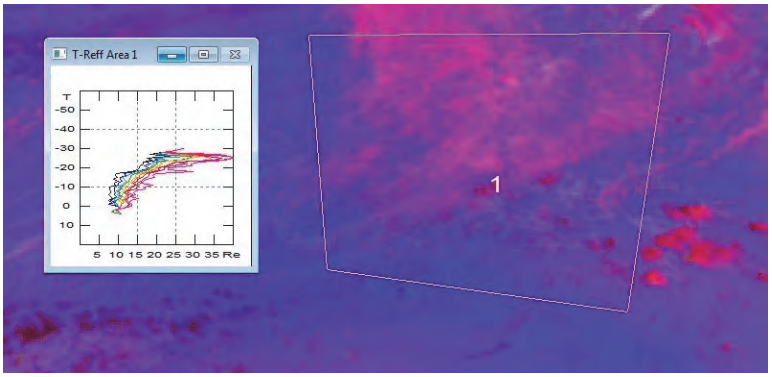

Fig. 2. Analysis of the situation for 1400 UTC. May 23, 2013 – nonsevere profile. Color lines (black to magenta) in profiles are expressing 5th to 100th percentiles of effective particle radius in the interval of 1 °C.

4. T-re profiles in the territory of Central Europe

As already mentioned above, two groups of convective situations (severe and nonsevere) were studied. The areas of convective clouds either moving to Central Europe or developing there were determined, and the satellite images generated from the MSG data were compared. These images were analyzed in a time interval when the solar zenith angle of the Sun was greater than 65°. Within that time period, the reflected sunlight in the 3.9 μm channel was sufficient. In these areas and times, the *T-re* analysis was done, and the data from the saved images were subsequently processed. Afterwards, a forecast of the severity of a storm based on the *T-re* profile shapes and gained values was given immediately as the profiles revealed severe features. Later, it was compared to weather reports and radar observations. A case study was selected from each group to be analyzed in a greater detail for the Central European region. Dangerous phenomena in the severe case and the typical *T-re* features are described.

4.1. Comparison of severe and nonsevere situations

This Chapter introduces the *T-re* profiles of one severe and one nonsevere situation to show their mutual differences. However, it is clear that the temperatures and particle sizes do not match exactly the values which were received from the profiles in other countries (*Rosenfeld et al.*, 2008), because Central European conditions are partly different. For example, cloud base temperatures are usually lower in Central Europe in the warm season, and cloud particles near the cloud base are slightly larger compared to profiles derived, for example, from the USA. For this reason we decided to test this method in the European environment, and we tried to get specific *T-re* shapes for this region.

The shape and position of percentile lines in profiles are the main features of profiles, which can help us to decide if the storm is prone to grow to a severe or nonsevere storm.

In this case, a nonsevere situation means that thunderstorms developed without dangerous accompanied phenomena are classified according to ESWD. The situation represents the threshold state for nonsevere/severe situations. Other weaker or less intensive storms revealed even shallower *T-re* profiles with larger particles at lower levels and cloud tops which did not reach significantly higher levels, i.e., over 6 km, are typically nonsevere profiles.

4.1.1. Case study of June 12, 2010: the severe situation

This situation was chosen as a case study due to the occurrence of a supercell with large hail, heavy rain, and strong wind. It is a typical severe storm with dangerous attendant phenomena. Furthermore, *Figs. 1.a-f* clearly show gradual evolution of *T-re* profiles in Central Europe from 1457 UTC to 1627 UTC after they became severe. Cloud particles grow very slowly to larger sizes, when coalescence and mixing of liquid water with ice particles continues.

A low pressure area moving to the southeast was affecting Central Europe, the temperature maxima in the Czech Republic were about 26 °C. After 1500 UTC, massive Cbs were observed, and thunderstorms developed in the Czech Republic. In southern Bohemia, a supercell formed where a rotation of the cloud system was observed from the ground by witnesses, and a funnel cloud was reported. After 1700 UTC, hail and heavy rain occurred. The hail diameter was about 3 cm. Severe wind gusts were reported after 1800 UTC, followed by heavy precipitation in south of Moravia. After 2000 UTC, other wind gusts were reported in southern Moravia. Strong wind was observed after 1800 UTC in Austria and it was followed by a heavy rain. The wind speed in the squall line was 25 m/s (ESWD).

The analysis of cloud areas in *Fig. 1a* shows very small particles (less than 15 μm in radius) up to about –20 °C in clouds according to *T-re* profiles. This indicates a strong updraft in the lower part of these clouds, namely in area 1 showing a long and nearly linear lower part of the profile which indicates the possibility of a severe weather occurrence (*Rosenfeld et al.*, 2008). This is confirmed by a hail report from South Bohemia and other dangerous phenomena in the vicinity (ESWD). The profiles in *Figs. 1a-1f* are similar to the profiles gained by *Rosenfeld et al*. (2008), when hail and other severe weather events were documented. As early as 1457 UTC, cloudiness with a strong updraft above Austria (*Fig. 1a* – area 1) is revealed by the *T-re* analysis. The profile starts at 9 °C and 6 μm. This indicates the cloud base temperature (*Tb*) to be 9 °C and the effective radius of cloud base particles (*rb*) to be 6 μm, which is in agreement with *Rosenfeld et al*., (2008) and other authors (*Rosenfeld* and *Lensky*, 1998). The top of the zone of coalescence (*Tl* - temperature of the lower linear part of the

profile, it mostly represents the top of the layer in which the particles grow mostly by the diffusional or coalescence processes) only reaches –8 °C with a cloud particles' radius at that level (*rl* - cloud particle radius near the top of the lower linear part of the profile) of 8 μm, but the mixed phase zone steeply reaches the *Tg* (temperature of the glaciation zone bottom) of –28 °C and *rg* (radius at *Tg* - temperature of the glaciation phase bottom) of 18 μm. This level indicates the full development of the ice phase inside the cloud and the top of a deep mixed phase. In such clouds, the precipitation is mostly formed by snow particles and hail. Later, the updraft becomes even stronger and fills a vertically higher area. Its extent is from 9 °C (*Tb*) at the cloud base to the level of –16 °C (*Tl*). The particle radius at the cloud base (*rb*) is 6 μm and *rl* (particle radius at *Tl*) is 8 μm. The particles rise in updraft so quickly that they do not have enough time to grow to larger sizes before reaching that level. The top of the mixed phase zone reaches the level of *Tg* of –40 °C with *rg* of 34 μm. The difference between *Tl* and *Tg* is equal to 24 °C, which is quite large. For a high severity storm, the difference is supposed to be as small as possible. Later, the coalescence zone reaches higher levels, and the difference between *Tl* and *Tg* decreases to only 7 °C. This indicates that the severity of the developing storm rises. After 1500 UTC, larger particles in *T-re* profiles appear, and the slope of profiles is not as steep as in the case described above. The regeneration of updrafts (and *T-re* profiles severity) to the previously mentioned values occurs at about 1600 UTC (*Fig. 1f* – area 1) but after 1700 UTC, the clouds are filled with larger particles, and the updrafts weaken again.

Area 2 in *Fig. 1f* (east of Germany, west of the Czech Republic) shows a coalescence zone from 0 °C and an *rb* of 7 μm to –20 °C and 13 μm. The mixed phase continues up to the level of –33 °C with an *rg* of 38 μm. The vertical extent of the small particle zone is shallow, and particles grow fast to larger sizes. This profile thus provides information about a weaker updraft and, according to some of the following images from later hours, it did not reach larger intensity. No severe weather events were reported from that area.

The cloud base temperature (*Fig. 1e* – area 3) was 12 °C and *rb* 3 μm at 1612 UTC. The coalescence zone reaches the level of –26 °C with *rl* 17 μm. The top of the mixed phase zone is then detected at –38 °C level with *rg* 29 μm. Such a profile corresponds to a strong updraft. Later, at about 1700 UTC, that strong updraft rises to the level of –40 °C with *rg* of 15 μm. At least large hail may be predicted with the help of this cloud profile. Particles of such a small radius at this height reveal a significantly severe updraft inside clouds.

4.1.2. Case study of 23May 2013: the nonsevere situation

There are no severe weather reports in ESWD for the May 23rd, 2013. There were thunderstorms observed in the northeast of the Czech Republic according to

professional weather station reports. The weather was influenced by the low pressure area.

Since the morning hours, stronger updrafts in the lower part of clouds have been revealed by *T-re* profiles. Cloud base temperature is about 3 °C, and the radius of particles is 6 μm. The coalescence zone reaches the level of –27 °C with *re*12 μm. Later the radius grows to 22 μm. The cloud base temperature changes to -8 °C, and the particle radius changes to 7 μm. A radius of 15 μm is reached at the level of –20 °C. The profiles have nearly linear shape in some parts, but they are bent down to larger particles (to the right side of the profile). *Fig. 2* shows the cloud base temperature at about 4 °C, and the radius of particles at 9 μm. The cloud top reaches –29 °C with particle radius 23 μm. The lower linear part of the profile (coalescence zone) reaches the level of –16 °C with particle radius 14 μm. The cloud tops do not reach any significant height. A fully glaciated zone with small particles typical of severe situations is not developed. The profiles confirm only a nonsevere convection in the observed region.

5. Results

The data for the analysis are stated in *Tables 1* and *2*, and their description follows in the text. *Table 1* is sorted by the following accompanying events of storms, providing the data of analyzed situations:

TOR – tornado (1)
GR – hail (2)
+RA – heavy rain (3)
FC –funnel cloud (4)
NONSEVERE (5)

Consider tornado being the most intensive (dangerous) accompanying event of a storm expressing its intensity, number 1 was assigned as the most intensive case decreasing to number 4 (see *Figs. 3* and *5*). The intensity decreases from tornado (1) through hail (2) and heavy rain (3) to funnel cloud (4) as mentioned above with respect to the danger for human and infrastructure. The nonsevere category is represented by the number (5).

The description (intensity) of each event (size of hail, length of funnel cloud and so forth) is mentioned in *Table 1* if it was provided by sources (ESWD). Additional information about the date and place of the event is stated together with the time of the forecast of the severe event. This forecast was made according to the analyzed profiles. The analyzed features of the *T-re* profiles in *Table 1* are provided as follows: *re* (μm), *re base* (μm), *re top* (μm), *Tl* (°C), *Tg* (°C), *T14 μm* (°C).

Table 1. Reported severe weather events, nonsevere situations and analyzed values of *re*, *Tl*, *Tg* and *T14μm*

Date	Month	Country	Event	Other event	Attendant phenomena	Time of report (UTC)	Forecast of dangerous event (UTC)	*re* (μm)	*re base* (μm)	*re top* (μm)	*Tl* (°C)	*Tg* (°C)	*T14μm* (°C)
May 23, 2005	5	PL	TOR	GR		1800	1300	6-38	6	38	-28	-38	-28
May 16, 2006	5	FR	TOR	GR	hail 3 cm	1337	1212	4-38	4	38	-15	-33	-15
May 26, 2007	5	D	TOR	GR	F1T3 - 11 km x 200 m path, hail 3 cm	1550	1212	6-33	6	33	-35	-48	-35
Jun 25, 2006	6	D	TOR	GR	F1T3 - 3 km x 300 m path, hail 3 cm	1630	1242	7-28	7	28	-28	-42	-28
Jun 21, 2011	6	CZE	TOR		F1T3 - 9km path	1509	1342 (GR)	9-40	7	40	-20	-38	-15
Jul 23, 2010	7	FR	TOR		0,5 km x 30 m path, hail 5 cm	1600	1112	7-40	7	40	-25	-30	-30
Jul 23, 2010	7	IT	TOR	GR	hail 7 cm	1630	1042	6-40	6	40	-20	-30	-25
Jul 29, 2013	7	CZE	TOR	RA	F1T3, rain 50 mm/h	after 2000	1157	6-36	6	36	-30	-40	-20
Apr 20, 2012	4	CZE	GR		hail 2 cm	1230	1230	6-33	6	33	-22	-30	-22
May 22, 2010	5	CZE	GR		hail 0.5 cm	1100-1500	0757	8-40	8	40	-12	-32	-17
May 27, 2010	5	CZE	GR	FC	hail 3,5 cm, 50 % cloud to ground	1730	1342	7-40	7	40	-24	-31	-27
May 10, 2011	5	D	GR	+RA		1935	1457	5-29	5	29	-32	-40	-28
May 20, 2011	5	D	GR	+RA	rain 60 mm/h, hail 2 cm	1400-1700	1227	7-38	7	38	-27	-35	-20
May 20, 2011	5	PL	GR	+RA	hail 2,5 cm	1400-1800	1227	7-38	7	38	-27	-35	-20
May 2, 2012	5	D	GR		hail 2,5 cm	1800	1142	5-32	5	32	-30	-38	-22
May 3, 2012	5	PL	GR		hail 2-3 cm	after 1100	0845	6-28	6	28	-28	-40	-28
May 4, 2012	5	PL	GR	FC	hail 2 cm	after 1400	0715	6-38	6	38	-20	-32	-25
May 7, 2013	5	PL	GR	FC	hail 3,5 cm, 50 % cloud to ground	after 1400	0715	7-32	7	32	-25	-38	-29
May 8, 2013	5	CZE	GR	FC	hail 3 cm, rain 33 mm/h	1350	1100	4-32	5	32	-36	-38	-28
May 9, 2013	5	PL	GR		hail 3 cm	after 1500	0630	7-20	7	20	-15	-38	-20
Jun 12, 2010	6	PL	GR		hail 3-10 cm	1840	1427	6-35	6	35	-29	-35	-29
Jun 30, 2010	6	CZE	GR		hail 0,2-1 cm	1330	1142	4-30	5	30	-25	-31	-27
Jun 30, 2010	6	D	GR		hail 3 cm	1500	1257	6-33	6	33	-15	-41	-25
Jun 30, 2010	6	SVK	GR		hail 2 cm		1257	5-33	5	33	-12	-36	-17

Table 1. (continued)

Date	Month	Country	Event	Other event	Attendant phenomena	Time of report (UTC)	Forecast of dangerous event (UTC)	*re* (μm)	*re base* (μm)	*re top* (μm)	*Tl* (°C)	*Tg* (°C)	*T14μm* (°C)
Jul 19, 2007	7	D	GR	+RA	hail 3 cm	1500	0804	7-32	7	32	-20	-38	-27
Jul 19, 2007	7	CZE	GR			1800	1339	7-33	7	33	-25	-38	-27
Jul 19, 2007	7	PL	GR			2000	1204	7-33	7	33	-25	-38	-27
Jul 1, 2009	7	D	GR	FC	hail 4 cm, 40 % cloud to ground	1627	1242	11-38	11	38	-12	-24	-12
Aug 15, 2010	8	CZE	GR		hail 3-5 cm	1900	0927	6-35	6	35	-18	-38	-20
May 31, 2011	5	CZE+A+D	+RA			after 2000	1442	6-33	7	33	-20	-33	-22
Jun 24, 2013	6	PL	FC		35% cloud to ground	1630	0830	7-35	7	35	-25	-35	-25
Jul 19, 2013	7	A	FC		30% cloud to ground	1400-1600	1354	7-12	7	35	-12	-30	-15
Aug 9, 2011	8	CZE	FC		35 % cloud to ground	after 1900		8-40	8	40	-22		-22
Nonsevere situations													
Apr 23, 2013	4	CZE						8-30	8	30	-20	-30	-25
May 12, 2013	5	CZE						9-40	9	40	-22		-24
Jun 7, 2013	6	CZE						10-40	10	40	-18	-31	-18
Jul 20, 2013	7	CZE						8-18	8	28	-10		-12

CZE - Czech Republic
A - Austria
PL - Poland
D - Germany
SVK - Slovak Republic
FR - France
IT - Italy
TOR - tornado
GR - hail
+RA - heavy rain
FC - funel cloud

The values of *rb* (cloud particle radius near the cloud base), *rl* (cloud particle radius near the top of the lower linear part of the profile), *rg* (temperature of the glaciation phase bottom), *Tb* (cloud particle temperature near the cloud base), *Tl* (temperature of the top of the lower linear part of the profile), and *Tg* (temperature of the glaciation phase bottom) are graphically shown in *Fig. 1f* to be understood better. From here, these temperatures and radii abbreviations are used in the text for faster and better orientation.

The cloud base particle radius provides information about the starting point of the evolution of clouds. The smaller the cloud base particle radius is, the more severe event can be expected (*Rosenfeld et al*., 2008), considering other cloud features such as *Tl*, *Tg,* etc., as confirmed in *Table 2*. For example, in situations with tornado occurrence, the cloud base particle radius was 6.1±0.9 μm, 7.0±0.0, with heavy rain, and 8.8±0.8 μm in nonsevere cases.

On the other hand, the particle radius at the cloud top provides information about the size of particles in the highest part of the cloud. It helps to uncover the intensity of updrafts reaching the cloud top. Smaller particles near the cloud top indicate stronger updrafts pervading through the whole cloud cell. Large particles near the cloud top indicate a weakening updraft at higher levels.

The temperature at the top of the lower linear part of the profile and the temperature of the glaciation phase bottom provide information about the severity of a developing storm in middle altitudes. The lower these temperatures are, the more intensive phenomena are to be expected. A similar rule can be set up on the base of the difference between *Tl* and *Tg*. With the decreasing value of that temperature difference we can expect more extreme events developing in the storm as shown in *Table 2*.

Finally, the temperature of the level where particles reach the radius of 14 μm is the precipitation threshold temperature. With the decreasing temperature of the level of 14 μm particle radii, stronger updraft is indicated inside the cloud. Indirectly, it may be deduced that a more severe storm will develop (see *Table 2*). Additionally, the knowledge of the cloud base temperature indirectly helps the improvement of the convection and precipitation (*Zhu et al.*, 2014) forecasts. It helps to reveal the top of boundary layer and the water vapor mixing ratio, which helps to calculate CAPE more accurately (*Zhu et al*., 2014).

Table 2. Statistical values: mean, standard deviation, median, mode, 10% percentile, and 90% percentile for the following characteristics: *re* at the cloud base, *re* at the cloud top, *Tl, Tg,* and *T14μm,* the difference of *Tl* and *Tg* all split by weather events. Zeros mean that no appropriate value was found, a blank space was not calculated as explained in Section 5.1.

EVENT	STATISTICS	*re base* (μm)	*Tl* (°C)	*Tg* (°C)	*T14μm* (°C)	*Tl–Tg* (°C)
TOR	MEAN + SD	6.1 ± 0.9	–25.1 ± 6.1	–37.4 ± 5.8	–24.5 ± 6.8	12.3 ± 4.1
TOR	MEDIAN	6	–26.5	–38	–26.5	11.5
TOR	MODE	6	–28	–38	–28	10
TOR	10 % PERC.	5.4	–31.5	–43.8	–31.5	8.5
TOR	90 % PERC.	7	–18.5	–30	–15	18
GR	MEAN + SD	6.5 ± 1.3	–22.8 ± 6.7	–35.5 ± 4.1	–23.7 ± 4.7	12.7 ± 6.5
GR	MEDIAN	6	–25	–38	–25	12
GR	MODE	7	–25	–38	–27	8
GR	10 % PERC.	5	–30	–40	–28	6
GR	90 % PERC.	7	–12	–31	–17	23
+RA	MEAN + SD	7 ± 0	–20 ± 0	–33 ± 0	–22 ± 0	13 ± 0
+RA	MEDIAN	7	–20	–33	–22	13
+RA	MODE	0	0	0	0	0
+RA	10 % PERC.	7	–20	–33	–22	13
+RA	90 % PERC.	7	–20	–33	–22	13
FC	MEAN + SD	7.3 ± 0.5	–19.7 ± 5.6	–32.5 ± 2.5	–20.7 ± 4.2	14 ± 4
FC	MEDIAN	7	–22	–32.5	–22	14
FC	MODE	7	0	0	0	0
FC	10 % PERC.	7	–24.4	–34.5	–24.4	10.8
FC	90 % PERC.	7	–14	–30.5	–16.4	17.2
NONSEVERE	MEAN + SD	8.8 ± 0.8	–17.5 ± 4.6	–30.5 ± 0.5	–19.8 ± 5.2	11.5 ± 1.5
NONSEVERE	MEDIAN	8.5	–19	–30.5	–21	11.5
NONSEVERE	MODE	8	0	0	0	0
NONSEVERE	10 % PERC.	8	–21.4	–30.9	–24.7	10.3
NONSEVERE	90 % PERC.	9.7	–12.4	–30.1	–13.8	12.7

GR – hail; TOR – tornado; +RA – heavy rain; FC – funnel cloud

As can be expected, *Table 1* shows that no single value (as *Tl*, *Tg*, etc.) can provide any relevant and complete information about the severity of a developing storm. However, it can show values from which the storm can be predicted to become severe, but there is no strict boundary in values between individual severe event values in *Table 1*. This confirms that we need to analyze the *T-re* profile as a whole to see all connections above and under a specific value in the profile.

Better information about threshold values between individual severe events is provided with statistically processed data (mean values and standard deviations) in *Table 2*.

Table 2 also provides some basic statistical quantities that were applied to the values of *re base* (μm), *Tl* (°C), *Tg* (°C), *T14μm* (°C), and *Tl-Tg* (°C). The quantities are mean, standard deviation (SD), median, mode, 10% percentile, and 90% percentile for each severe weather event. They are presented in *Table 2*.

The analysis of the statistical quantities showed that there is a good transition value of *re base*, *Tl*, *Tg,* and *T14μm,* which would clearly distinguish severe and nonsevere situations. Moreover, these features may distinguish different severe accompanying phenomena in most cases. However, it is still faster and easier to analyze the gained *T-re* profiles as an image without any calculations. Some basic features of severe and nonsevere *T-re* profiles gained from *Tables 1* and *2* are mentioned in the Section 6.

Not every nonsevere situation is mentioned in *Tables 1* and *2*, because the values of tracked features are always typically nonsevere. Nonsevere situations, especially those with rain and without thunderstorms which could potentially form a new "non-thunderstorm" category were also analyzed, but the values of their tracked features cannot be included in the statistical analysis for the nonsevere category. These values were not in our focus. In addition, they would shift the gained statistical severe/nonsevere threshold results closer to the "non-thunderstorm" values, i.e., far from the desired threshold values. Furthermore, these values would enlarge the standard deviation of the tracked values in the nonsevere category, which would cause false alarm cases.

5.1. Nonsevere situations

Nonsevere situations, still significant in terms of convection, which were included in the statistics can be considered a threshold state between nonsevere and severe situations. There were thunderstorms without any severe accompanying phenomena observed. The definitely non-thunderstorm convective situations have only a small vertical extent with cloud tops typically below 6 km, and particles grow to larger sizes in the coalescence zone at lower levels rather than in the cases presented here. As the analysis reveals, in nonsevere (threshold) situations the coalescence zone to (*Tl*) does not usually reach the –20 °C level as it can be seen in *Table 2*. There are mostly large particles in the coalescence growth zone with a radius of about 15 μm. Near the level of –20 °C or lower (towards the ground), the particles start to enlarge their sizes quickly. The coalescence in nonsevere situations has a larger effect compared to the severe situation. Slower updrafts allow particles grow to larger sizes as they stay in a relatively thin area in contrast to severe situations. A radius of about 30 μm is usually reached near the temperature of about –30 °C. The particles freeze heterogeneously, and their sizes enlarge quickly in this zone. Cloud bases very often

develop between temperatures of 10 °C and 0 °C, with the highest frequency between temperatures of 5 °C and 0 °C.

Nonsevere thunderstorms with large Cbs can reach a level of –40 °C. The analyzed profiles show a noticeable bent shape, and there is no linear part of the graph.

It is important to remember that the large extent of the updraft zone and low temperatures near cloud tops indicate hail or other severe attendant phenomena. Even if there were a strong updraft in clouds which did not reach very low temperatures, severe storms would not develop.

In the situation where only rain was observed, even the values mentioned above are not reached, and the profiles are shaped towards larger particles at lower temperatures (to the right side).

The following threshold values between nonsevere and severe storms were found: *re base* 8.8 ± 0.8 μm, *Tl* –17.5 ± 4.6 °C, *Tg* –30.5 ± 0.5 °C, and *T14μm* –19.8 ± 5.2 °C (*Table 2*). The high values of standard deviations are caused by the situation on July 20th, 2013, which is included in the statistics. This is a typical nonsevere situation with higher tracked temperatures, which causes the enlargement of the standard deviation. The situations with smaller *re base* and lower temperatures (*Tl, Tg, T14μm*) are prone to grow into storms with severe attendant phenomena. Estimating the difference of *Tl* and *Tg* for the nonsevere cases is absolutely irrelevant, because the glaciation phase with *Tg* value mostly did not develop.

5.2. Severe situations

T-re profiles of severe situations (convective storms with dangerous attendant phenomena) reach much higher levels than in the case of nonsevere situations. The profiles are steeper in the thicker zone, mostly in their lower part, with this zone being frequently linear or nearly linear as the updraft pushes the particles higher with a high speed. A radius of 14 μm is mostly reached by the level of –20 °C or above, when the clouds include ice particles. The particles do not grow fast because they do not stay in the coalescence zone for a long time. When the ice particles are small at a level of around –40 °C, it indicates vigorously growing cells with a strong updraft inside. Cloud droplets freeze homogenously there, and the radius is usually less than 35 μm in this zone. Cloud particles with radii less than 14 μm often fill the zone of the temperature difference of 30 °C or more.

In the case of 2–3 cm hail occurrence, a particle radius of 9 μm was observed up to the level of –22 °C. In the case of 3 cm hail and 20 mm/h rain, a radius of 14 μm was identified at a level of about –28 °C. With larger hail (4 cm), the radius of 14 μm reached a level of about –30 °C.

Table 2 shows the mean values and standard deviations of tracked features for different severe storms with various attendant phenomena. It clearly shows that the *re base* decreases with increasing the severity of the accompanying phenomena of a storm, and the same is valid for the mentioned temperatures *Tl*, *Tg*, and *T14μm.*

The illustrative interpretation is depicted in boxplots, in *Figs*. *3a-d*.

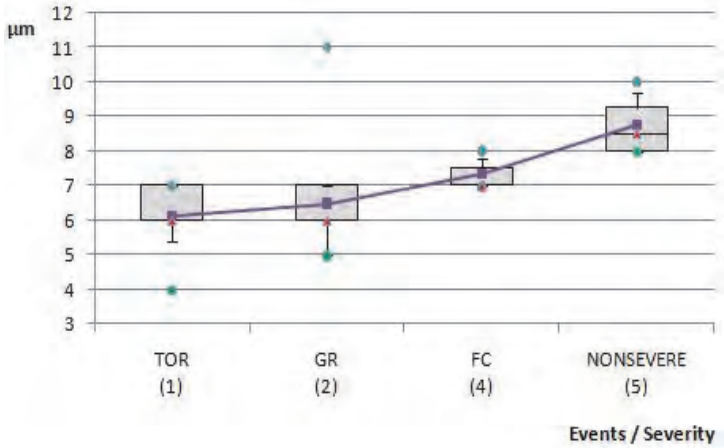

Fig. 3a. Boxplots of *re base* (µm) for different attendant phenomena of storms. Decrease of *re base* with an increase in the attendant phenomena severity represented by the different group of attendant phenomena. Number 1 was assigned to the most intensive case (tornado) decreasing to number 5 (nonsevere) as explained in Section 5. The case of heavy rain (3) is not included because only one case was recorded. The bottom of the box of *re base* represents the value of the 1st quartile, the middle dark line in the box with the red triangle is the median, the violet rectangle inside each box is the mean, and the top of each box is the 3st quartile value. The bottom and top of each whisker are the 10% and 90% percentiles, and the green and blue dots are the maximum and minimum, respectively. In the values of the mean for tracked features depicted by the box profiles, a clear decrease in tracked size with increasing severity of storms can be seen.

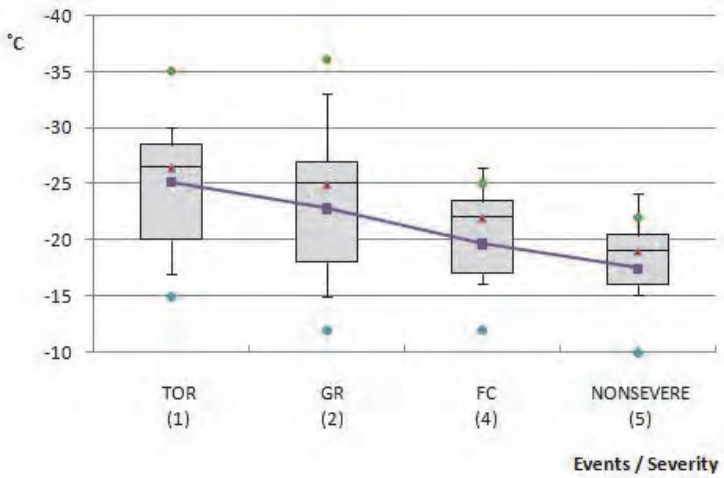

Fig. 3b. The same as *Fig. 3a* but for *Tl* (°C) for different attendant phenomena of storms.

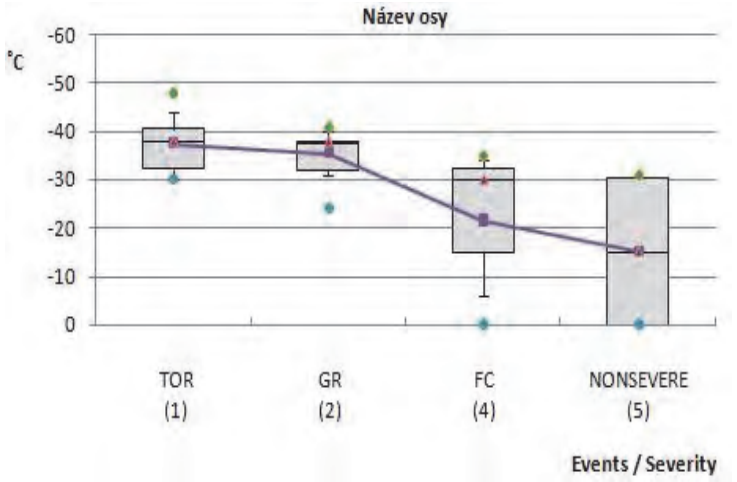

Fig. 3c. The same as *Fig. 3a* but for *Tg* (°C) for different attendant phenomena of storms.

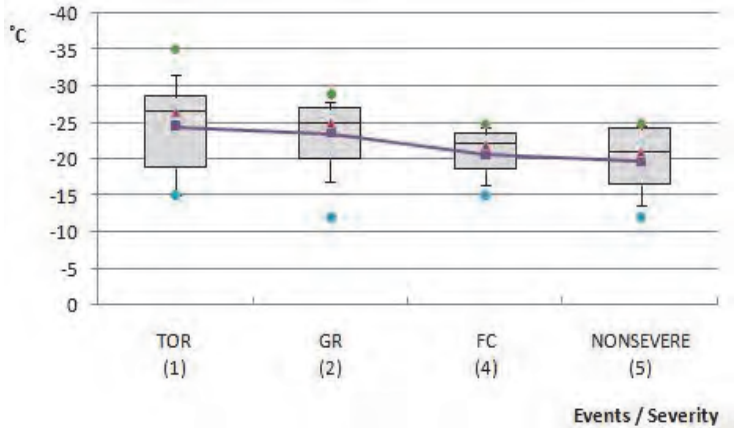

Fig. 3d. The same as *Fig. 3a* but for *T14μm* (°C) for different attendant phenomena of storms

The difference of *Tl* and *Tg* as presented in *Table 2* decreases with an increase in storm severity. In cases with funnel cloud occurrence, the difference was 14 ± 4 °C, in heavy rain cases 13 ± 0 °C, in hail cases 12.7 ± 6.5 °C, and in tornadic cases 12.3 ± 4.1 °C.

Furthermore, correlation analysis was performed. It represents a statistical method which describes the relationship between two variables. The first step was the compilation of the correlation matrix (*Table 3*), which includes the correlation coefficients of all the couples of variables, here the tracked features of *T-re* profiles (*re base*, *Tl*, *Tg*, *T14μm*). In this case, correlation represents the mutual relationship

between two tracked features. The level of correlation is influenced by the value of the correlation coefficient R that attains values from –1 to +1. There is no relationship between the studied variables if the value of R equals 0. A positive value close to +1 represents direct proportion (a positive correlation), –1 on the other hand represents indirect proportion (a negative correlation). Taking into account our results where all the values of R were higher than 0.92 (*Fig. 4*), a significant positive linear correlation for tracked features was found.

Table 3. Correlation coefficients (R) of all couples of tracked features (*re base, Tl, Tg, T14µm*). The values of correlation coefficient represent significant linear correlation of all tracked features, because all the values are close to 1.

	***re* base (µm)**	**Tl (°C)**	***Tg* (°C)**	***T14µm* (°C)**
***re* base (µm)**	1.00			
***Tl* (°C)**	0.92	1.00		
***Tg* (°C)**	0.93	1.00	1.00	
***T14µm* (°C)**	0.92	0.97	0.98	1.00

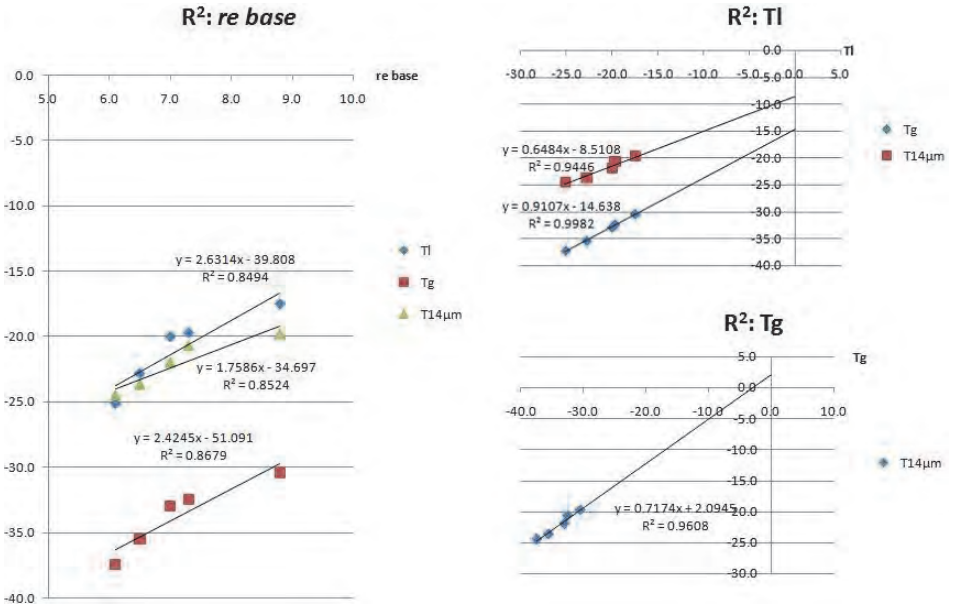

Fig. 4. Coefficient of determination (R^2) of *re base* and other tracked features of *T-re* profiles (*Tl*, *Tg*, *T14µm*).

The correlation matrix (Table 3) provides the correlation coefficients (R) for all couples of tracked features (*re base*, *Tl*, *Tg*, *T14μm*). All couples are in significant linear correlation, since R is higher than 0.92 for all. The determination coefficients confirm that the line equation confidence level is higher than 84%. Linear coefficients are statistically significant at the significance level 0.05.

Fig. 4 shows the linear correlation of all couples of tracked features where the horizontal axis represents one feature and the vertical axis represents the other feature for each couple. Their correlation is provided by the equation of the line and R^2 represents the suitability of the model.

The knowledge of linear correlation for tracked features of *T-re* profiles allows us to find a model of correlation for those features. On the basis of the results, the model can only provide a simple mathematical forecast, but it cannot result in certainty. That trend predicts next evolution of features according to the previous evolution. Every mathematical forecast has its own confidence level, which represents the reliability of that forecast. The confidence level (*Table 4*) is expressed by the determination coefficient (R^2) that attains values from 0 to 1, where 1 means 100% confidence. The determination coefficient (R^2) of our data was always equal to more than 0.84; thus, the confidence level of the model of the regression function is always higher than 84%.

Table 4. Determination coefficient (R2) of all couples of tracked features (*re base, Tl, Tg, T14μm)*

	***re base* (μm)**	***Tl* (°C)**	***Tg* (°C)**
***Tl* (°C)**	0.8494		
***Tg* (°C)**	0.8679	0.9982	
***T14μm* (°C)**	0.8524	0.9446	0.9608

The revealed linear correlation of *re base*, *Tl*, *Tg,* and *T14μm* made it clear that the mentioned temperature *T14μm* decreases with the increasing severity of the attendant phenomena of storms and a proportional decrease of *Tl* and *Tg* as well as *re base* with the increasing severity of the attendant phenomena of storms. This correlation analysis confirms previously specified rules of *T-re* profiles in severe weather analysis and forecasting (*Rosenfeld et al.*, 2008). With the increasing severity of weather events, the *T-re* profiles actually shift to the left side of the graph (to smaller *re*) and extend higher (to lower temperatures) (see *Fig. 1* and *Fig. 2* to compare).

The determination coefficients for all couples of tracked features were calculated (*Table 4*). The value expresses in percent the reliability of the line equation of two features. All the values exceed a value of 84%, thus the equation describes the correlation between two features better than 84%.

The processed data are graphically presented in *Fig. 4*, which proves the correlation of individual tracked features, their trend functions and confidence level. Similarly, the trend functions for *Figs. 5a-d* were obtained. The graphs reveal the correlation of individual tracked features and the severity of attendant phenomena of a storm, trend function, and determination coefficient (R^2), where the confidence level of each model is greater than 90%.

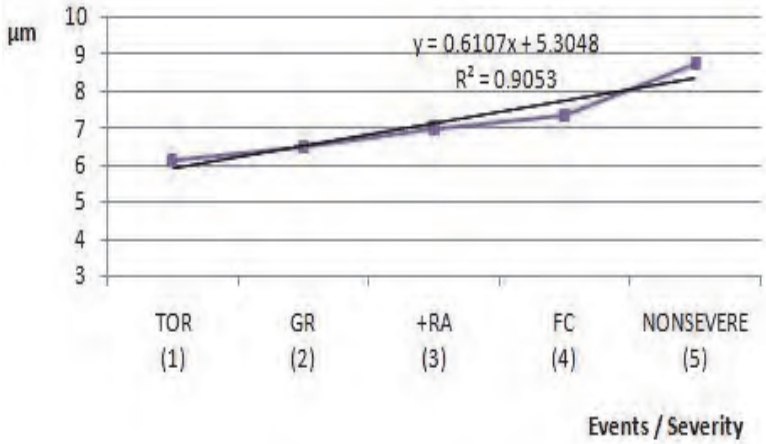

Fig. 5a. Coefficient of determination of *re base* for different groups of attendant phenomena of storms.

Consider *re base* as a mean of *re base*. Gaining high value of R (correlation coefficient) expresses the linear correlation of *re base* and the intensity of storms represented by the different group of attendant phenomena. The equation of the line (see the graph) describes the data at the significance level of 90% what is represented by the value of the coefficient of determination (R^2) to be 0.9053.

According to the values gained from the graph and the equation of the line we can find the storm severity. If, for example, the *re base* equals six, then the equation gives the stage of a tornado, but this can also indicate other storm stages (TOR, GR, etc.). The only result is that the storm stage could be a tornado. All other tracked features (*Tl*, *Tg* or *T14µm*) have to be evaluated as well.

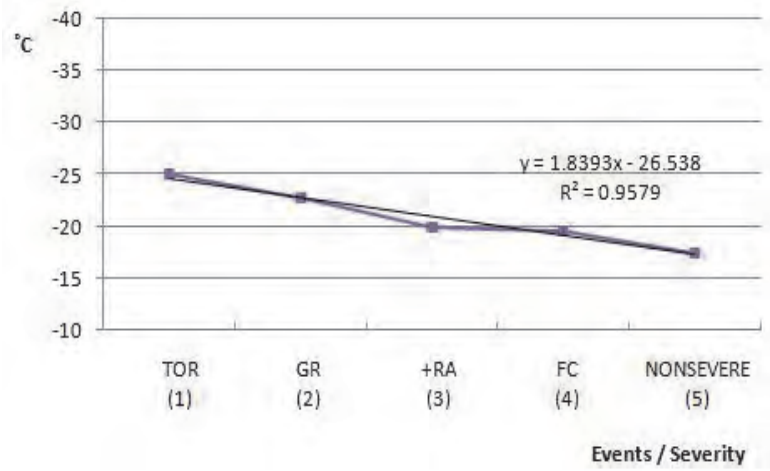

Fig. 5b. The same as *Fig. 5a* but for *Tl* for different groups of attendant phenomena of storms.

Consider *Tl* as a mean of *Tl*. A high value of R (correlation coefficient) expresses the linear correlation of *re base* and the intensity of storms represented by the different group of attendant phenomena. Significant linear correlation was found at the level of 95.8%.

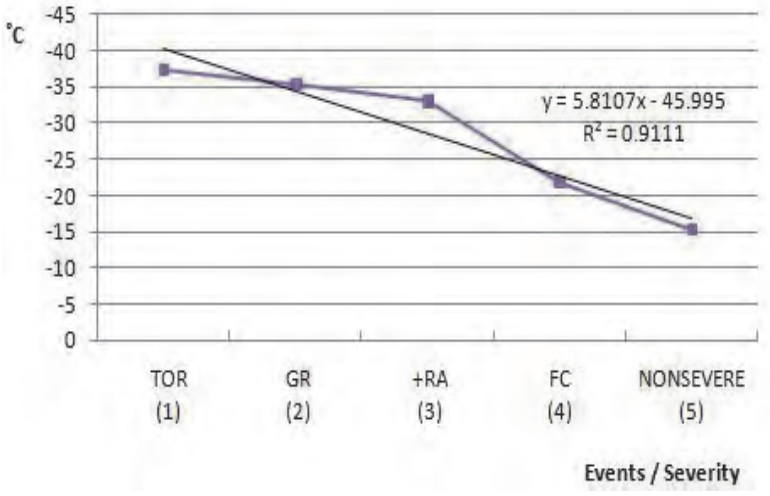

Fig. 5c. The same as *Fig. 5a* but for *Tg* for different groups of attendant phenomena of storms

Consider *Tg* as a mean of *Tg*. Gaining a high value of R (correlation coefficient) expresses the linear correlation of *re base* and the intensity of storms represented by the different group of attendant phenomena. Significant linear correlation was found at the level of 91.1%.

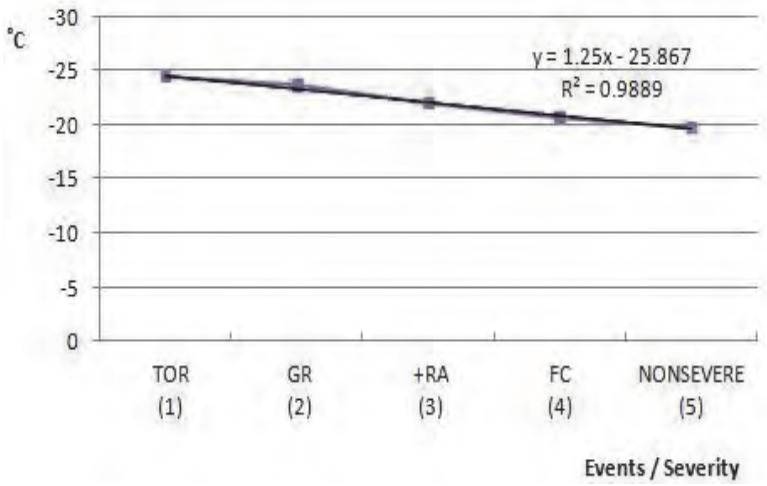

Fig. 5d. The same as *Fig. 5a* but for *T14μm* and the intensity of attendant phenomena of storms.

Consider *T14μm* as a mean of *T14μm*. Gaining a high value of R (correlation coefficient) expresses the linear correlation of *re base* and the intensity of storms represented by the different group of attendant phenomena. Significant linear correlation was found at the level of 98.9%.

Individual graphs and models of functions, regardless of the R^2 value, cannot be considered as decisive. In addition, it was proved that one single tracked feature cannot be used as a unique storm severity forecast element. All the tracked features, the shape of the *T-re* profile and its position and extent should be studied. As it is demanding to gain all the tracked features, to find all their correlations, and to find which variables support the model, it is also very difficult to assemble a global model of the tracked features for making storm severity decisions. It would probably also request more storm cases observation, which requires the gathering of automated data.

The linear correlation of *re base* and the tracked temperatures allows us to simplify the description of the *T-re* profiles. In an ideal case, it is possible to divide the individual part of a profile to individual lines defined by the temperatures *Tl* and *Tg* (*Fig. 1a-f*). As a matter of fact, the profile is a non-ramp fiction due to the vertical axis inversion, which corresponds to the real temperature decrease in the atmosphere. As has already been mentioned, one of the severe storm signs is the long linear (or nearly-linear) lower part of a *T-re* profile, rising to the breaking point of *Tl*.

This analysis should be considered a demonstration in which the independent dataset was used to test the previously derived relationships (*Rosenfeld et al*., 2008) requested by *Rosenfeld et al*. (2008). It has confirmed the value of the methodology for nowcasting of severe weather events.

Fig. 6 presents graphically the number of events reported (blue) and forecasted (red) in a given hour. Nearly 30% of the reported cases occurred at 12–14 UTC and nearly a similar percentage at 16–18 UTC. The prediction of a severe event was mostly (45%) performed at 12–14 UTC, which is in good agreement with severe weather occurrence, subsequently at 10–12 UTC.

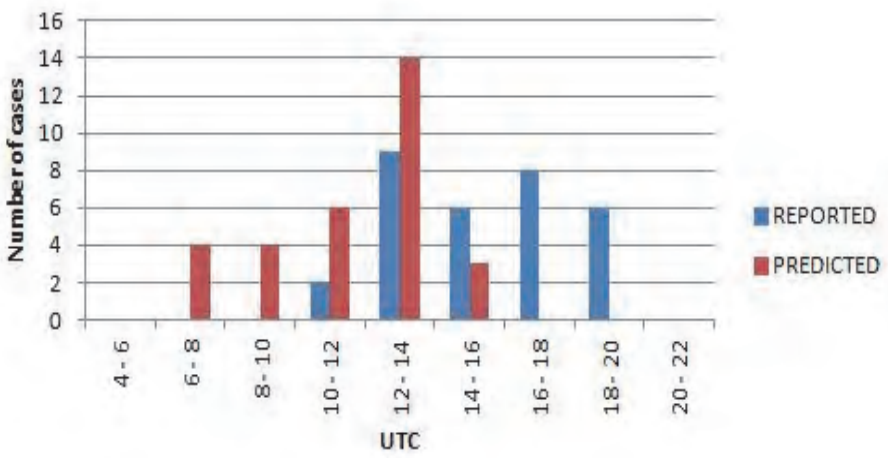

Fig. 6. Time distribution of reported (blue) and predicted (red) severe attendant phenomena of storms.

The forecasting skill of the *T-re* method was statistically evaluated (*Fig. 7*) comparing the time of the reported event (i.e., not the time of the first occurrence of the event) of the European Severe Weather Database and the time of our own severe event forecast. We compared the time of forecast and the time of the report of the event intentionally, because it is very complicated to estimate the time of first occurrence of the event without any appropriate confirmed observation. *Fig. 7* graphically shows the most frequent time difference of the forecast of an event before it was reported as discussed above. 68 percent of the predictions of severe weather were performed about two hours before its report, which is a good advantage for preventive measures. *Jurkovic et al.* (2015) found the ability of a *T-re*

profile to reveal severe updrafts inside clouds 10-20 minutes in advance before hail start to fall out of the clouds. For example, the formation of hailstone with a size of 1 cm does not usually last longer than 1 hour.

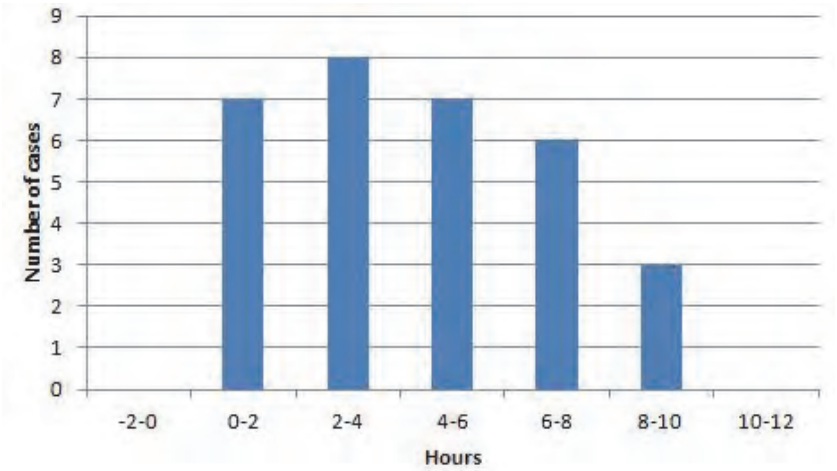

Fig. 7. Numbers of severe weather events according to the time difference of predicted and reported events (i.e., not the time of the first occurrence) as discussed in Section 5.2. Large intervals can be the consequence of inaccuracy of the detection of the precipitation type and amount on the ground.

Jurkovic et al. (2015) confirmed also that deep convective clouds which are associated with greater updraft speed are filled by smaller particles with a *re* of 15–20 μm above the level of –30 °C and a *re* of 30 μm above the level of –40 °C. He also stated the basic shapes of *T-re* profiles and other features of severe storm clouds in Europe (*Jurkovic et al*., 2015). Nonsevere storms on the other hand reveal a very different dependence of particle size on temperature. Large particles (*re* more than 35 μm) are frequently found below the level of –20 °C (*Jurkovic et al*., 2015).

There were no failed predictions of severe storms occurrence arising from the background of the method. According to cloud microphysics rules which can be depicted in gained profiles, failed predictions of severe storms cannot occur. Some people may incorrectly forecast different severe cases from others.

6. Discussion

It is apparently not possible to determine the absolute exact threshold values of *T* and *re* between different severe phenomena. It is important to analyze the thickness of the zone with small particles (less than 15 μm), the whole vertical extent of cloud cells and the shape of profiles in all their parts as well as the auxiliary values, such as *Tl*, *Tg* and *T14μm* etc. The mean values of *Tl* and *T14μm* followed by the mean values of *re base* and *Tg* presented in *Table 2* for each severe event could, on the other hand, are considered being a hint in distinguishing of different severe attendant phenomena of developing storms. These satellite-based predictors are considered to be at least as good as, for example, frequently used atmospheric sounding predictors and are much more detailed in time and space (*Rosenfeld et al*., 2008). They are able to vary in time, because they are recalculated with every new satellite observation, which allows them to react to actual cloud development. When applied to multispectral geostationary satellite data, the *T-re* method provides us with a typical storm signature before these clouds are revealed by weather radar. Therefore, additional time to detect a severe storm is provided, although with lesser spatial accuracy compared to weather radars (*Rosenfeld et al.*, 2008). In general, it can be concluded that the profiles in Central Europe start at lower temperatures compared to those from the US (approximately about 5–10 °C), and the values *Tg* and *Tl* are observed at higher levels as well. The crucial point is that the cloud particle diameters are usually about 3–5 μm larger near the cloud base and again at higher levels compared to those from the US. The differences can be due to different instruments and resolution, not necessarily caused only due to physical features of air mass.

In some cases, the profiles indicate strong updrafts even during forenoon, but the dangerous events are reported in the evening.

For all presented severe situations, the mean particle effective radius at the cloud base is found to be between 6.0 and 7.3 μm as presented in *Table 2*. Tornadic situations, considered the most severe event, reveal the second highest mean of particle effective radius at the cloud base, but the smallest median together with hail and heavy rain cases. Small radii, about 6 μm or even smaller at the cloud base indicate a higher probability of tornado occurrence. There are also clear indications that smaller *Tl* and *T14μm* indicate greater severity of an event, the same for *Tg* can be said in most cases as well. All the severe situations presented in *Table 1* show smaller *Tg* and *Tl* difference in mean values ($\leq$2 °C) than nonsevere situations (10 °C). Some specific connections similar to our findings were stated by *Sporre et al.* (2014). They clearly mentioned that clouds with greater vertical extent have higher precipitation rates compared to less developed clouds. His study also confirms that meteorological parameters such as atmospheric instability or cloud vertical extent affect the precipitation amount measured on the ground more than aerosols.

Presenting some statistically processed values provides threshold values as well as other described rules of specified temperatures and their relationships, but in some cases it does not describe the situation of *T-re* profiles the best way. Statistical values sometimes do not strictly differentiate between particular severe events, because analyzed values (such as *Tg* or *Tl*) are generalized too much. Thus, it is crucial to analyze the *T-re* profiles as a unique situation description, just because every thunderstorm is unique with different *T-re* values and also not every tornado is the same. Human forecasters are much more successful at severe weather forecasting compared to existing automated systems (*Doswel*, 2014), and with help of other analysis tool they could be even better.

The method of severe storm intensity forecasting with the help of *T-re* profiles applied to the MSG satellite data in the region of Central Europe seems to be apparently successful.

7. Conclusions

The basic principle of the presented theory is the analysis of cloud particle profiles based on satellite observation in different spectral channels to help forecast and identify a potentially dangerous storm. It is possible to generate *T-re* profiles that represent the microphysical composition of clouds with special software. The analysis of archived satellite data selected according to dangerous weather reports as well as real-time data from the MSG reception station was carried out, and the applicability of these profiles were evaluated in Central Europe for the first time. The nonsevere threshold situations were analyzed in order to confirm the potential of this tool also for these non-threatening cases. *T-re* profiles have proved to be a useful tool for nowcasting during severe convective storm situations in this region. However, different air mass types play a crucial role in the thermodynamic condition above different areas. The profiles from Central Europe revealed, for example, the shift in the temperature and size of cloud particles compared to profiles from other continents, as mentioned in Section 4. Also *Tl* and *Tg* values were usually higher, which represents lower temperatures than in the profiles of *Rosenfeld et al*. (2008).

The *T-re* method can help to reveal the areas apt to produce severe weather phenomena mostly one or two hours in advance, sometimes even sooner, analyzing cloudy areas from morning hours in days with expected intense convection. It is a very simple software to use and quickly provides a microphysical preview of clouds. This research revealed the fact that it is crucial to see the whole profile with all of its features to be able to create a forecast of severity for a developing storm. A stand-alone value such as *Tl* or *Tg* without knowing any other features of a *T-re* profile cannot provide complete and exhaustive relevant information to use in forecasting. It can however provide an initial impulse in distinguishing between severe and nonsevere cases, and in most

cases, in distinguishing between particular severe cases. After familiarization with a typical *T-re* profile for severe situations, a local forecaster should be able to use it successfully to improve the severe weather nowcasting processes. With the help of this nowcasting tool, specific and more accurate weather warnings for particular areas can be issued to protect property or even lives.

Acknowledgements: This project was supported by the Specific Research Fund of the Faculty of Mathematics and Physics, Charles University, Prague, number SVV-2011-263308. A special thanks goes to *Dr. Itamar Lensky*, Bar-Ilan University, Israel, the provider of the MSG_RGB software and EUMETSAT for providing the satellite data.

References

Brázdil, R., Chromá, K., Dobrovolný, P., and *Černoch*, Z., 2012: The Tornado History of the Czech Lands, AD 1119-2010. *Atmos. Res. 118*, 192–204.

Brooks, H.E., 2012: Severe Thunderstorm and Climate Change. *Atmos. Res. 123*, 129–138.

Doswel, C.A.III, 2014: Severe Convective Storms in the European Social Context. *Atmos. Res. 158-159*, 210–215.

Dotzek, N., 2003: An updated estimate of tornado occurrence in Europe. *Atmos. Res. 67-68*, 153–161.

Dotzek, N., Groenemeijer, P., Feuerstein, B., Holzer, A.M., 2009: Overview of ESSL's severe convective storms research using the European Severe Weather Database ESWD. *Atmos. Res. 93*, 575–586.

Field, C.B., Barros, V., Stocker, T.F., Qin, D., Dokken, D.J., Elbi, K.L., Mastrandrea, M.D., Mach, K.J., Platner, G.K., Allen, S.K., Tignor, M., and *Midgley, P.M.*, 2012: Managing the Risks of Extreme Events and Disaster to Advance Climate Change Adaptation. A Special Report of Working Groups I and II of the Intergovernmental Panel on Climate Change. Cambridge University Press, Cambridge, UK, New York, NY, USA, 582 pp.

Holzer, A.M., 2001: Tornadoes Climatology of Austria. *Atmos. Res.* 56, 203–211

Horváth, Á. and *Geresdi, I.*, 2003: Severe Storms and Nowcasting in the Carpathian Basin. *Atmos. Res. 67-68*, 319–332

Jurković, P.M., Mahović, N.S., and *Počakal, D.*, 2015: Lightning, Overshooting Top and Hail Characteristics for Strong Convective Storms in Central Europe. *Atmos. Res. 161-162*, 153-168.

Lensky, I., 2009: User Guide for MSG_RGB. Personal communication.

Lensky, I. and *Rosenfeld, D.*, 2005: The Time-Space Exchangeability of Satellite Retrieved Relations Between Cloud Top Temperature and Particle Effective Radius. *Atmos. Chem. Phys.6*, 2887–2894.

Lensky, I., Shiff, S., 2007: Using MSG to monitor the evolution of severe convective storms over East Mediterranean Sea and Israel and its response to aerosol loading. *Adv. Geosci. 12*, 95–100.

Martins, J.V., Marshak, A., Remer, L.A., Rosenfeld, D., Kaufman, Y.J., Fernandez-Borda,R., Koren, I., Yubko, V., and *Artaxo, P.*, 2007: Remote Sensing The Vertical Profile of Cloud Droplet Effective Radius, Thermodynamic Phase and Temperature. Atmos. Chem. Phys. Discuss. 7, 4481–4519.

Melani, S., Cattani, E., Levizzani, V., Cervino, M., and *Torricella, F.*, 2003: Radiative effects of simulated cirrus clouds on top of a deep convective storm in MSG SEVIRI channels. *Meteorol. Atmos. Phys. 83*, 109–122.

Pfeifer, M., Yen, W. ,Baldauf, M., Craig, G., Crewell, S., Fischer, J., Hagen, M., Huhnerbein, A., Mech, M., Reinhardt, T., Schroder, M., and *Seifert, A.*, 2010: Validating Precipitation Forecast Using Remote Sensor Synergy: A Case Study Approach. Meteorol. Zeit. 19, 601–6017.

Roberts, R.D. and *Rutlege, S.*, 2003: Nowcasting Storm Initiation and Growth Using GOES-8and WSR-88D Data. *Weather Forecast. 18*, 562–584.

Rosenfeld, D., Fischman, B., Zheng, Y., Goren, T., and *Giguzin, D.*, 2014: Combined Satellite and Radar Retrievals of Drop Concentration and CCN at Convective Cloud Base. *Geophys. Res. Let. 41*, 3259–3265.

Rosenfeld, D. and *Lensky, I.*, 1998: Satellite-Based Insights into Precipitation Formation Processes in Continental and Maritime Convective Clouds. *Bull. Amer. Meteorol. Soc. 79*, 2457–2476.

Rosenfeld, D., Woodley, W.L., Krauss, T.W., and *Makitov, V.*, 2006: Aircraft Microphysical Documentation from Cloud Base to Anvils of Hailstorm Feeder Clouds in Argentina. *J. App. Meteorol. Clim. 45*, 1261–1281.

Rosenfeld, D., Liu, G., Yu, X., Zhu, Z., Dai, J., Xu, X., and *Yue, Y.*, 2013: High Resolution (375m) Cloud Microstructure as Seen from The Satellite NPP/VIIRS Satellite Imager. *Atmos. Chem. Phys. Discus. 13*, 29845–29894.

Rosenfeld, D., Woodley, W.L., Lerner, A., Kelman, G., and *Lindsey, D.T.*, 2008: Satellite Detection of Severe Convective Storms by Their Retrieved Vertical Profiles of Cloud Particle Effective Radius and Thermodynamic Phase. *J. Geophys. Res.113*, D04208.

Setvák, M., 1989: Convective Storms - The AVHRR Channel 3 Cloud Top Reflectivity as A Consequence of Internal Processes. Proc. 5th WMO Conference of Weather Modification and Applied Cloud Physics, Beijing, China, WMO/TD 269, 109-112.

Shiqiang, F. and *Zhemin, T.*, 2001: On the helicity dynamics of severe convective storms. *Adv. Atm. Sc. 18*, 67–86.

Sporre, M. K., Swietlicki, E., Glantz, P., and *Kulmala, M.*, 2014: A long-term satellite study of aerosol effects on convective clouds in Nordic background air. Atmos. *Chem. Phys. 14*, 2203–2217.

Tokay, A. and *Short, D.A.*, 1996: Evidence from Tropical Raindrop Spectra of the Origin of Rain from Stratiform versus Convective Clouds. *J. Appl. Meteorol. 35*, 355–371.

Tolasz, R., Brázdil, R., Bulíř, O., Dobrovolný, P., Hájková, L., Halásová, O., Hostýnek, J., Janouch, M., Kohout, M., Krška, K., Křivancová, S., Květoň, V., Lepka, Z., Lipina, P., Macková, J., Metelka, L., Míková, T., Mrkvica, Z., Možný, M., Nekovář, J., Němec, L., Pokorný, J., Reitschläger, J.D., Richterová, D., Rožnovský, J., Řepka, M., Semerádová, D., Sosna, V., Stříž, M., Šercl, P., Škáchová, H., Štěpánek, P., Štěpánková, P., Trnka, M., Valeriánová, A., Valter, J., Vaníček, K., Vavruška, F., Voženílek, V., Vráblík, T., Vysoudil, M., Zahradníček, J., Zusková, I., Žák, M., and *Žalud, Z.*, 2007: Atlas podnebí Česka - Climate Atlas of Czechia. Český hydrometeorologický ústav, Praha, Univerzita Palackého v Olomouci, Olomouc.

Zheng, Y. and *Rosenfeld, D.*, 2015: Linear Relation between Convective Cloud Base Height and Updrafts and Application to Satellite Retrievals. *Geophys. Res. Let. 42*, 6485–6491.

Zheng, Y. and *Rosenfeld, D., Li, Z.*, 2015: Satellite Inference of Thermal and Cloud-Base Updraft Speeds Based on Retrieved Surface and Cloud-Base Temperatures. *J. Atmos. Sci. 72*, 2411–2428.

Zhu, Y., Rosenfeld, D., Yu, X., and *Li, Z.*, 2015: Separating Aerosol Microphysical Effects and Satellite Measurement Artifacts of the Relationship between Warm Rain Onset Height and Aerosol Optical Depth. *J. Geophys. Res. 120*, 7726–7736.

Zhu, Y., Rosenfeld, D., Yu, X., Liu, G., Dai, J., Xu, X., 2014: Satellite Retrieval of Convective Cloud Base Temperature Based on The NPP/VIIRS Imager. *Geophys. Res. Let. 41*, 1308–1313.

Zipori, A., Rosenfeld, D., Tirosh, O., Teutsch, N., and *Erel, Y.*, 2015: Effects of aerosol sources and chemical compositions on cloud drop sizes and glaciation temperatures. *J. Geophys. Res. 120*, 9653–9669.

Web references

Nowcastimg Thunderstorm Intensity from Satellite: A Review, *Robert M. Rabin*: http://www.ssec.wisc.edu/~rabin/paper/eumetsat/paper2_eumetsat.doc, 2015.

European Severe Weather Database: http://www.eswd.eu/, 2015.

European Severe Weather Database – Definitions: http://www.eswd.eu/cgi-bin/eswd.cgi?action =showdefinitions&lang=en_0, 2015.

Abbreviation list

CAPE – convective available potential energy
CCN – cloud condensation nuclei
CIN – convective inhibition
dBZ – radar reflectivity scale
EPS – EUMETSAT Polar System
ESSL – European Severe Storms Laboratory
ESWD – European Severe Weather Database
GOES – Geostationary Operational Environmental Satellites
MSG – Meteosat Second Generation
NOAA – National Oceanic and Atmospheric Administration
NWP – numerical weather prediction
Re – cloud particle effective radius
re base – cloud particle radius range near the cloud base
re top – cloud particle radius range near the cloud top
RGB – colored combination of satellite channels
RUC – rapid update cycle
SAFNWC– Satellite Application Facility on support to Nowcasting
T14μm – temperature of the level when particles reach a radius of 14 μm
Tg – temperature of the glaciation phase bottom
Tl – temperature of the top of the lower linear part of the profile
T-re – *T* represents cloud top temperature, *re* means particles effective radius
USA – The United States of America
WV – water vapor

IDŐJÁRÁS

Quarterly Journal of the Hungarian Meteorological Service
Vol. 121, No. 3, July – September, 2017, pp. 243–263

The effect of climate and soil moisture on the tree-ring pattern of Turkey oak (*Quercus cerris L.*) in Central Transdanubia, Hungary

István Péter Kovács[1] and **Szabolcs Czigány**[2*]

[1]*Department of Cartography and GIS, University of Pécs, Ifjúság u. 6, H-7624 Pécs, Hungary*

[2]*Department of Physical- and Environmental Geography, University of Pécs, Ifjúság u. 6, H-7624 Pécs, Hungary*

**Corresponding author E-mail: szczigany@gamma.ttk.pte.hu*

(Manuscript received in final form August 1, 2016)

Abstract—Dendrochronological studies have revealed several environmental signals of many oak species supporting the suitability of these species for climate reconstruction (*Haneca et al*. 2009). Despite the large number of studies, limited information is available on the influence of climatic condition and soil moisture on the growth characteristics of Turkey oak (*Q. cerris*). Although soil moisture is probably the most limiting factor on growth of most oak species, relevant studies in Hungary primarily focused on the effect of temperature and rainfall, and ignored the impact of soil moisture. The combined analysis of climatic factors and soil moisture would reveal the importance of the influencing factors and would point out the anatomical patterns and environmental signals of a given area. In the current study, we analyzed the dendrochronological characteristics of a grove in Western Hungary (Central Transdanubian Region), and correlated tree anatomical patterns with the mean monthly temperatures, monthly precipitation totals, and modeled soil moisture at five different depths. The grove is exposed to environmental stress due to the local soil and climatic factors. Our findings indicate that the most pronounced environmental signal stored in the oaks is the change of soil moisture that exposes a direct impact on tree growth.

Key-words: Turkey oak, soil moisture, tree-ring width, early wood width, late wood width

1. Introduction and aims

1.1. Background

One of the most notable feature of Earth's climate is its variability, which has been profoundly affecting the evolution of life, distribution, diversity, and health of trees and forest composition. The natural global warming that followed the Pleistocene glaciation is exacerbated by the increased concentration of greenhouse gases (*Smith et al*., 2014) and exerts an increasing influence on forests. According to most studies, climate of the Carpathian Basin likely becomes drier and warmer in the very near future (*Bartholy et al.,* 2008), which, besides the increasing number of extreme events, envisages the increasing frequency of droughts (*Führer et al.,* 2011a). The single known positive effect of warming climate is the increasing growth rate of the warm-loving and drought-tolerant tree species (*Somogyi,* 2007, 2008), however, this sole positive phenomena is likely unable to counterweight for all the negative effects of global warming. With the decreasing return period of drought, the occurrence of forest fire likely increases (A1B emission scenario, *Smith et al.,* 2014), while, similarly, the spreading of fungi-originated diseases speeds up, insect and pest damages intensifies, therefore, tree tissue structure alters, triggering the general deterioration of tree health conditions (*Mátyás et al.* 2010; *Klimo* and *Hager,* 2001). The habitat of less drought-tolerant species will be taken over by less productive species ((*Führer et al.,* 2011a), resulting in decreasing productivity and CO_2 uptake. In Hungary, the decreasing areal distribution of beech and sessile oak, and simultaneously, the spreading of Turkey oak is expected (*Móricz et al*., 2013). The latter species makes up 11.2 percent of the forest stands of Hungary (*Miniszteri Tájékoztató,* 2015). Nevertheless, wood quality and economical significance of Turkey oak, due to its known growth disorders (e.g., frost cracks) and imperfections, is lower than for other oak species (*Molnár et al.,* 2007). Hence, due to its spreading in the region, thorough understanding of its dendrochronological features is indispensable. Climatic preferences and reactions of common European oak species (e.g., *Quercus robur, Quercus petreae, Quercus pubescens, Quercus ilex* etc.) are well known (*Cufar et al.*, 2014; *Haneca et al.,* 2009), and studies on the topic have also been conducted in Hungary (*Kern et al.,* 2009). However, due to their similar structural composition, oak species pursue different survival strategies and react for increasing drought frequency in a different manner (*Nardini* and *Tyree*, 1999). Turkey oak has a homogeneous dendrochronological character, and it is sensitive to climate changes, providing valuable climatic signals (*Nardini et al.,* 1999; *Di Filippo et al.,* 2010, *Stafasani* and *Toromani,* 2015). However, only regional data are available on the temperature and rainfall demand and drought tolerance of Turkey oak in Hungary (*Babos,* 1984; *Szabados,* 2008).

Tree-ring width (TRW) is the most commonly analyzed proxy in dendrochronological studies, which provides a general overview on tree growth. Tree-ring width fundamentally determines the anatomical features and structure of tree rings (*Gasson,* 1987; *Rao et al.,* 1997; *Leal et al.,* 2007; *Gričar et al.,* 2013), therefore, dendrochronological studies principally focus on TRW. Analyses of latewood width (LWW) and earlywood width (EWW) (*Eckstein et al.,* 1977; *Weigl et al.,* 2008), however, provide climatic signals of intra-annual resolution and enable researchers to obtain accurate paleoclimatic reconstruction of higher resolution. The aforementioned features are spatially heterogeneous, thus climatic signals are profoundly influenced by regional characteristics and settings (*Gričar et al.* 2013). Depth of groundwater table, soil moisture contents, slope, exposure, hierarchical role in ecological associations all influence growth (*Stokes* and *Smiley,* 1968), hence adequate filtering of climatic signal errors is only representative, when a sufficiently large number of specimens are sampled. In their European habitats, including Hungary, oaks most influentially react on the changes of long-term rainfall patterns. Growth of Turkey oak, depending on the water budget of the soil, is most profoundly affected by fall and winter rainfall of the preceding season and the early spring precipitation of the year of relevance (according to the authors' *former unpublished findings*). In other areas, the role of spring and summer precipitation (*Szabados,* 2008) were found to be the most influential factors, and the impact of temperature, as a limiting factor, had a lesser importance (*Haneca et al.,* 2009). Water demand of trees is primarily delivered from soils (*Fritts,* 1976), and many studies indicated that the growth of oak species is chiefly affected by mean monthly soil moisture values rather than precipitation (*Graiser*, 1951; *Auchmoody* and *Smith,* 1979). Yet, growth rate of selected species do not directly correlate with soil moisture contents (*Kwiaton* and *Wang,* 2015).

In the current study, we hypothesized, that the studied anatomical features directly indicate the plant available soil moisture totals at different depths, while only indirectly reflected the rainfall totals. Hitherto, no studies in Hungary have been conducted on the correlation between the growth characteristics of Turkey oak and the corresponding soil moisture contents. If our hypotheses are proven, implementation of the impact of various soil physical types on the growth characteristics of Turkey oak should be anticipated in the future.

Many international studies are available on the reconstruction of drought periods using tree-ring data (*Woodhouse* and *Overpeck,* 1998; *Stahle et al.,* 2000), therefore our studies may provide additional data for future analyses in this field.

To analyze the major anatomical patterns of Turkey oak, we studied a grove developed on soils of poor water availability that was formed on gravelly parent material. As groundwater table is located at greater depth than the longest roots, the association is exposed to climatic changes (group of sensitive oaks), and trees provide profound growth reactions on climatic changes.

The objective of the current study is the analysis of the anatomical patterns of the trees of the investigated site, and the comparison of anatomical patterns

with local climatic and soil moisture patterns to answer the following questions: Which climatic factors are responsible for tree growth? Which climatic signals are reproducible by the analysis of the tree rings of Turkey oak? What type of correlation can be identified between the anatomical pattern of Turkey oak and the change of soil moisture?

1.2. Site description

The research site is located northwest of the city of Ajka, on the low rolling hills of the Pápa-Bakonyalja region (*Dövényi,* 2010) (*Fig. 1*). The reason for selecting the site is our preliminary knowledge and extensive studies on the geomorphology and water conditions of the site (*Babák et al.,* 2013). A second intention for site selection was the extremely slow growth rate of the Turkey oaks of the area, indicating a major drought stress, periodically exerted on the specimens of the grove. The 1000-meter thick Creataceous limestone and the overlying carbonaceous Eocene sequence of 2 to 250 meters in thickness (Szőc Limestone Formation) emerges to the surface as a horn in the vicinity of the Szék Lake (*Bohn,* 1983). These strata are overlain by younger Oligocene and Miocene gravelly sediments (Csatka Formation) (*Bihari,* 1979). By damming the Csigere Creek, the Széki Reservoir, covering an area of 68 hectars, was constructed in 1978. The experimental site is located downstream from the dam in the upper part of valley side, northeast of the town of Devecser (*Fig. 1*). Springs were revitalized here due to the replenishment of the karst water system (*Babák et al.,* 2013) from the adjacent areas. As the site is located on a ground approximately 5 to 8 meters above the springs, the trees are unaffected by spring water and capillary water rise.

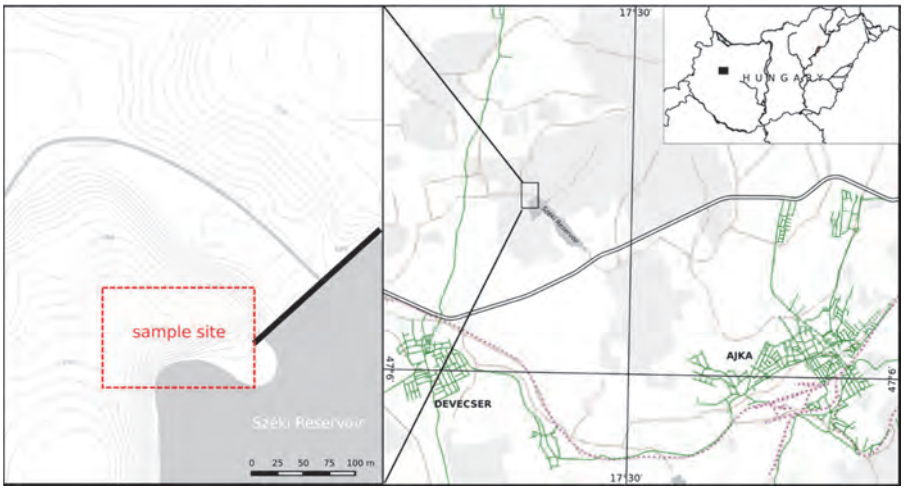

Fig. 1. Location of the study site.

The study area belongs to the Pápa-Bakonyalja forestry subregion (*Bidló et al.,* 2006). The moderately cool and moderately wet area has an annual insolation of 1,960 hours, and it is characterized with a mean annual rainfall total of 650 mm (*Dövényi,* 2010). Under the studied grove the typical genetic soil type is Leptosols (Entisols in the soil taxonomy), while the physical soil type is loam with a high concentration of coarse and gravelly fragments, characterized with unfavorable hydrologic properties and poor drainage. Topsoil thickness in the studied area ranges between 20 and 40 cm according to the AGROTOPO soil database compiled by the Research Institute for Soil Science and Agricultural Chemistry (RISSAC).

According to the studies of *Kovács et al.* (2012), the area belongs to the hornbeam-oak forest climatic zone, slowly transitioning to sessile oak – Turkey oak climate. The dominant tree species of the study area is the Turkey oak, however, along the Csigere Creek, black alder (*Alnus glutinosa*) is also commonly found. The approximate mean age of the trees of the studied grove ranges between 110 and 120 years. The average trunk diameter is around 35 cm, while the average height is about 22 meters. Turkey oak is a tree of Mediterranean origin, however, it easily adapts to the extreme temperature and soil moisture fluctuations of Hungary (*Gencsi* and *Vancsura,* 1992). Turkey oak is a ring-porous species that rarely develops missing and false rings, hence it is an ideal candidate for dendrochronological analyses (*Schweingruber,* 1993). During drought periods, taproot provides water supply for the trees, while root hairs create a homogeneous zone in the subsoil (*Führer et al.*, 2011b). The early wood vessels are relatively large, usually organized in the multiple rows. Wide rays and longitudinal parenchimas commonly characterize the xylem (*Molnár et al.*, 2007).

2. Methods

2.1. Dendrochronological methods

Sampling was done in April, 2014, during which 16 trees were sampled with random sampling (*Speer* 2011), and 31 drillings were used in our analyses. Sampling was done with a Haglöf Mora increment borer at breast height following the methods of *Jozsa* (1988). Core samples were glued to sample holders and were polished to 400 grits. The processed samples were digitalized at a resolution of 1200 dpi and were analyzed with ImageJ 1.48 software. Growth curve standardization (removal) was carried out with ARSTAN (44.h3), autocorrelation was minimized according to *Cook* (1985). Quality of the TRW, LWW, and EWW chronology, prepared for the period of 1979 to 2013, was validated with Cofecha (*Holmes,* 1983), during which mean sensitivity (MS) and expressed population signals (EPS) were considered.

Mean monthly temperatures and precipitation totals were measured at the Pápa Weather Station, located about 20 km from the study site, were downloaded

from the ftp.ncdc.noaa.gov server. Data were validated and corrected with the annual precipitation data of the Hungarian Meteorological Service. Using the meteorological data, forestry aridity index (*FAI*, *Führer,* 2010; *Führer et al.,* 2011a) was calculated for the studied period.

$$FAI = 100 \cdot \frac{T_{VII-VIII}}{P_{V-VII} + P_{VII-VIII}} , \quad (1)$$

where $T_{VII-VIII}$ is the mean temperature of the months of July and August, P_{V-VII} is the rainfall total of the months of May, June, and July, and $P_{VII-VIII}$ is the rainfall total of the months of July and August.

Linear correlations were then analyzed for all climatic, soil moisture, and anatomical datasets.

2.2. Soil moisture calculations

Using the aforementioned temperature and rainfall data, Thornthwaite potential evapotranspiration (*Thornthwaite,* 1948) was calculated according to Eq. (2):

$$E_{pot} = 16 \cdot \frac{L}{12} \cdot \frac{N}{30} \cdot \left(\frac{10T_a}{I} \right)^{\alpha} , \quad (2)$$

where L is the mean length of daylight during the given month, N is the number of days in the month of relevance, T_a is the mean monthly temperature, while I is the annual heat index, the sum of the monthly heat indices i, and α was calculated according to Eq. (3):

$$\alpha = (6.75 \cdot 10^{-7} I^3) - (7.71 \cdot 10^{-5} I^2) + (1.792 \cdot 10^{-2} I) + 0{,}.49239 . \quad (3)$$

The annual heat index I was calculated as follows:

$$I = \sum \left(\frac{T_a}{5} \right)^{1.514} . \quad (4)$$

Using the annual evapotranspiration and precipitation data, soil moisture content was modeled for the entire 35-year period with Hydrus-1D (v.4.16.0110). The initial time step was 1 month, thus 420 time variable records were entered to the model. The maximum number of iteration was set to 100. For the hydraulic model we used the Van Genuchten-Mualem model with hysteresis, with an initial drying curve. Residual water content θ_r was adjusted to 0.0737 $m^3\ m^{-3}$, while the saturated moisture content was set to 0.43 $m^3\ m^{-3}$. The van Genuchten parameter

of α was adjusted to 0.0019, while n and the saturated hydraulic conductivity (K_s) were set to 1.31 and 9.05 mm d^{-1}, respectively. The upper boundary condition (BC) was set to atmospheric BC with surface runoff, while for the lower BC, free drainage was selected. For the time variable BCs monthly precipitation and evaporation totals were used, and interception was not considered in the calculations. As Thornthwaite's equation calculates potential evapotranspiration, we ignored transpiration through the trees, with the exception of indicating the presence of root collar in the entire modeled soil profile with a root density of 100/mm.

Based on our field experience, a homogenous loamy soil profile of 60 cm depth was used in the model. The initial volumetric moisture content was set to 0.25 m^3 m^{-3} at the surface, and it gradually increased with depth to 0.35 m^3 m^{-3} to the bottom of the profile (60 cm). Soil moisture was modeled at depths of 4, 10, 20, 30, and 58 cm. Output model data were then correlated with tree anatomical parameters.

3. Results

3.1. Climatic changes

The overall tendency of the monthly precipitation totals indicate a decreasing trend for the period 1979–2013 for the study area (*Table 1*). Precipitation decrease is more pronounced for the months of November and December, however, a noticeable drop is observable during April and the summer months, during which water availability is crucial for tree growth. Slight increase in monthly rainfall totals is observable only in February, March, May, and September. Mean monthly temperatures, with the exceptions of September and December, indicate an increasing trend. Warming is the most pronounced during the summer months. The combined rainfall and temperature data clearly indicate the increasing aridification of the climate in the study area.

The *FAI* pattern acts similarly to the temporal aridification pattern of the area (*Fig. 2*). The *FAI* time series clearly indicates the arid periods of the late 1980s and early 1990s (=D9), the early 2000s (=D20), and the post-2010 (=D21) drought periods of the area. *FAI* is sensitive to the alteration of the arid and humid periods. The mean value of the *FAI* for the entire studied period was 6.82. Noticeably, during the dry periods, the mean value sometimes is exceed by twofold, reaching an index value of more than 13 and lasts for an excessively long time. The typical value of the index ranges between 4 and 6 during the more humid periods. The highest value of the *FAI* during the study period reached 14.17, its minimum was 3.3 with a standard deviation of 2.76. The overall temporal tendency indicated an increasing trend (*Fig. 2*).

Table 1. Slope of the linear regression line of the monthly rainfall totals (Pslope) and the mean monthly temperatures (Tslope) measured at the Pápa weather station between 1979 and 2013

Y	Pslope	Tslope
1	–0.138	0.052
2	0.258	0.024
3	0.206	0.007
4	–0.284	0.060
5	0.191	0.036
6	–0.245	0.066
7	–0.115	0.062
8	–0.133	0.043
9	0.084	–0.003
10	–0.121	0.006
11	–1.076	0.076
12	–0.593	–0.011
winter	–0.254	0.018
spring	0.112	0.034
summer	–0.493	0.057
autumn	–1.114	0.026

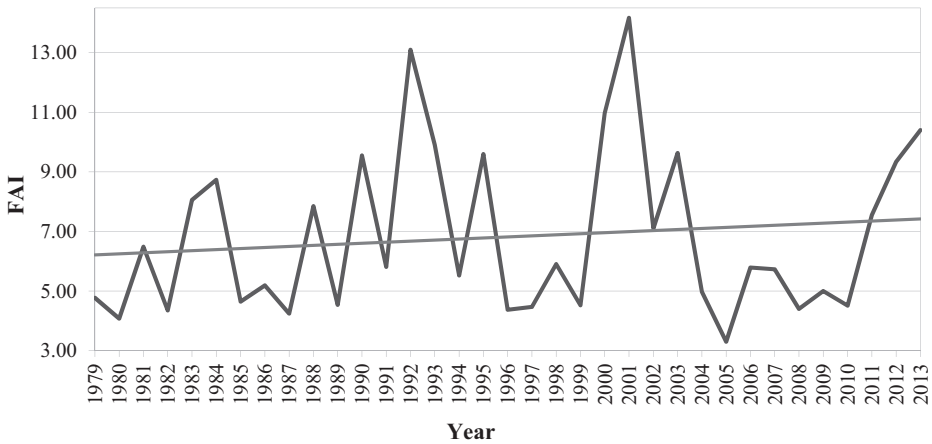

Fig. 2. Time series of the *FAI* values, based on the meteorological data of the Pápa weather station.

3.2. Soil moisture (SM) variability over the study period

The average soil moisture positively correlates with the month of the active vegetative period, and shows a relatively high correlation with January and February, however, we found no correlation with December. The highest correlation between *SM* and growth was found for spring and summer, especially for May and June, the months of the most intense LW formation.

As it was expected, the largest modeled soil moisture fluctuations and standard deviations were observed at a depth of 4 cm (*Fig. 3*). As shallow topsoil plays a very limited role in the physiological activity of large trees and is profoundly affected by drying up or rapid replenishment (*Echeverría et al.,* 2001; *Hegedüs et al.,* 2015), we ignored this modeled soil moisture data in our analyses. The amplitude and deviation of the *SM* data decreased with increasing depth, ranging between 0.27 and 0.33 m^3 m^{-3} below the depth of 20 cm. The periodical (monthly) *SM* fluctuations, generated by rainfall and evaporation variability, were hardly detectable below 20 cm. The modeled *SM* extremes (maxima and minima) at greater depths were shifted by up to a year compared to the values detected at a depth of 4 cm. However, unlike the climatic data, no long-term linear trend is observable for the temporal changes of *SM* data (*Table 2*).

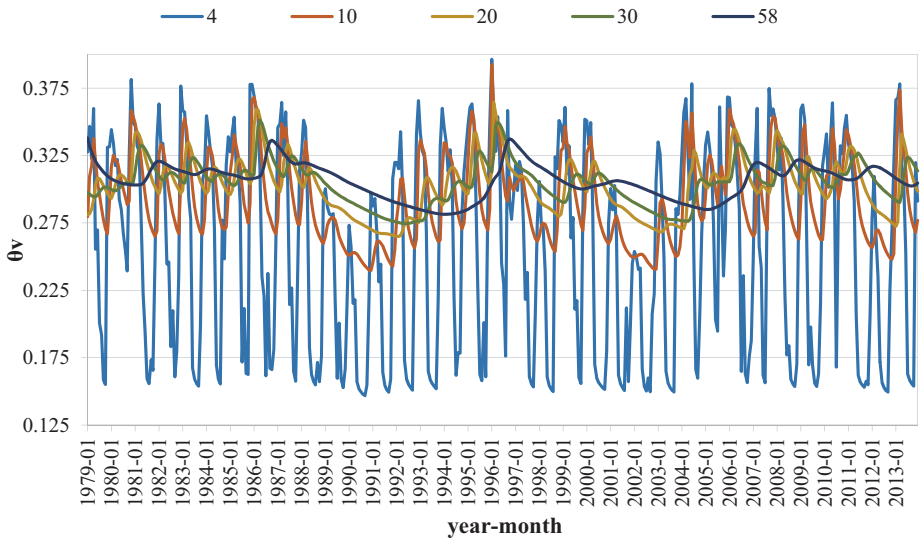

Fig. 3. Modeled volumetric soil moisture contents for the period 1979–2013 for five different depths (depths are shown in cm in the legend).

Table 2. Slope of the linear regression line of the soil moisture data at the five modeled depths between 1979 and 2013

Depth (cm)	Slope
4	–0.00039
10	–0.00021
20	–0.00009
30	–0.00002
58	–0.00018

3.3. Anatomical patterns of the studied trees

The oldest studied Turkey oaks of the experimental site reach an age of 110–120 years. During sampling, all trees were healthy, however, almost all trees were affected by frost cracks. Additionally, a considerable amount of methane has accumulated on the border of the hardwood and the sapwood, which was released in all cases during coring. Among the studied anatomical features, the earlywood and latewood form the tree-ring. Over the studied period, the tree growth and the increase of the EWW, LWW, and TRW were extremely low, compared to habitats of better water conditions (*Table 3*). Commonly, only a row of EW vessels was formed over the beginning of the growth season, therefore the EWW corresponds with the transversal width of the vessels. The deviation of the EWW was the lowest, and according to its size, this anatomical feature is the least influential (on average in 38%) in the structure of the tree ring. The only exception is the arid period during the early 2000s (from 2002 to 2004), when the width of the EW slightly exceeded that of the LW (*Fig. 4*). LW, on average, influences the TRW in 62%, and its width, similarly to the EWW is extremely low. A very strong linear correlation exists between the EWW and LWW with a coefficient of 0.998 closely correlating with the TRW.

Table 3. Statistical data of the studied anatomical features (MIN = minimum, MAX = maximum, AVERAGE = mean, STDEV = standard deviation)

	EWW	LWW	TRW
MIN	0.304	0.329	0.677
MAX	0.493	1.135	1.585
AVERAGE	0.415	0.717	1.132
STDEV	0.042	0.209	0.243

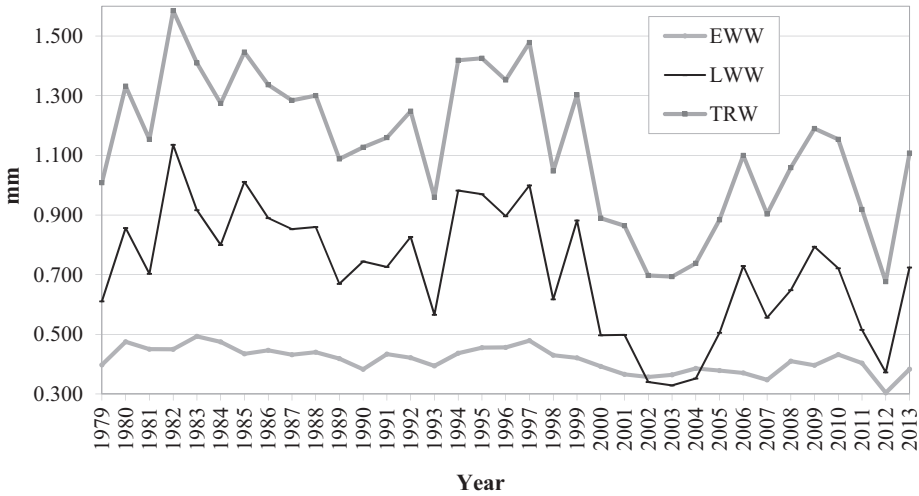

Fig. 4. Non-standardized EWW, LWW, and TRW chronology of the studied trees.

3.4. Correlation between the anatomical patterns and the climatic and SM data

At a probability level of $p = 5\%$ we only showed and analyzed correlations where correlations exceeded $r = 0.33$. The similar temporal behavior of EWW, LWW, and TRW showed a strong correlation with the measured climatic and modeled *SM* time series. The growth of the studied oaks was fundamentally influenced by monthly rainfall totals, while it was almost independent from mean monthly temperatures. Rainfall during fall of the preceding year, especially for September, showed a strong correlation with all anatomical patterns. Winter precipitation only showed correlation with the EW. Spring precipitation had a lower correlation with the anatomical patterns than the fall precipitation of the preceding year. Mean June temperatures exert a strong negative effect on growth rate. Despite the abundant literature on the importance of May precipitation (e.g., *Haneca et al.* 2009; *Gričar et al.,* 2013) on plant growth, correlations with the anatomical patterns found in the current study just fell below the threshold $r = 0.33$.

For the depth of 10 cm (*SM10*) the *SM* from January to August influenced growth rate of the studied grove, with a highest correlation with the spring months. Correlation was also found between the winter months and *SM10*, however, this is likely influenced by the moisture conditions of January and February (*Table 4*). Among the soil moisture values for a depth of 20 cm (*SM20*), the spring, summer and fall *SM* values influenced the growth rate positively. For the depth of 20 cm (*SM20*), the months from May to October impacted most intensely the growth rate

of the trees. *SM30* positively correlated with the months from May to October, and if entire seasons are considered, with summer and fall. For the SM values modeled for a depth of 58 cm, no correlation was found with the anatomical patterns. In accordance with the aforementioned time shift, the highest correlation was found for growth rate with winter *SM4*, spring *SM10*, summer and fall *SM20,* and fall *SM30* data. The average soil moisture for the entire profile positively correlated with the entire studied period (from January to October), including the months of January and February. Nevertheless, we found no correlation between the *SM* of the antecedent year and the anatomical patterns. Correlation coefficients between the *FAI* and the anatomical parameters ranged between 0.45 and 0.49.

4. Discussion

The aridification trend in Hungary has been widely published by many authors (e.g., *Mátyás et al.,* 2010; *Kovács et al.,* 2012), and it is supported by the linear correlation trends of the rainfall and temperature data observed in Pápa between 1979 and 2013. The aridification tendency is in accordance with the long-term changes of *FAI* that was already documented by *Führer* (2010) and *Führer et al.,* (2011a). *FAI* values are derived from the climatic data of the most intensely warming and aridifying months. The mean *FAI* value of 6.82 for the entire studied period positions the area into the zone of the forest climate that is characterized by sessile oak and Turkey oak. This finding is in a good correspondence with the findings of *Kovács et al.* (2012), although it is found in the upper portion of this forest climate zone (*FAI* = 6.001–7.250). It is also notable, that the *FAI* many times exceeded the lower boundary of the forest steppe climate that lacks climate-indicator tree species, or, in extreme cases, is characterized by the complete absence of trees (*Führer,* 2010). Trees of the studied grove were capable to tolerate these relatively short, maximum 4-year periods, as *FAI* is only interpreted as the climatic average of decadal periods. The changes of *FAI* values are clearly reflected in the LWW, EWW, and TRW values. Such arid periods are likely undesired for tree growth, as, besides rainfall, no additional water source (e.g., spring water) is available for their physiological functioning (*Somogyi,* 2007, 2008). Aridification may result in gradual decrease in growth rate or health disorders and deterioration (*Csóka et al.*, 2009).

Table 4. Linear correlations between soil moisture and anatomical parameters, monthly rainfall totals, and mean monthly temperatures

	Precipitation			Temperature			Soil moistured												
							10 cm			20 cm			30 cm			average			
	eww	lww	trw	eww	lww	trw	eww	lww	trw	eww	lww	trw	eww	lww	trw	eww	lww	trw	
p9	0.441	0.427	0.428																p9
p10																			p10
p11																			p11
p12																			p12
1							0.462	0.445	0.459							0.369	0.361	0.376	1
2							0.551	0.536	0.565							0.431	0.420	0.440	2
3							0.506	0.497	0.525	0.454	0.442	0.450				0.466	0.457	0.477	3
4							0.501	0.488	0.520	0.529	0.519	0.533				0.489	0.478	0.500	4
5	0.301	0.300	0.313				0.535	0.523	0.560	0.531	0.519	0.538	0.385	0.378	0.385	0.518	0.509	0.532	5
6				−0.367	−0.373	−0.377	0.436	0.424	0.464	0.533	0.522	0.545	0.446	0.439	0.447	0.502	0.492	0.520	6
7							0.445	0.433	0.472	0.502	0.490	0.518	0.481	0.474	0.484	0.490	0.479	0.507	7
8							0.437	0.428	0.466	0.491	0.480	0.509	0.496	0.488	0.502	0.478	0.469	0.497	8
9										0.493	0.482	0.512	0.495	0.487	0.504	0.438	0.431	0.455	9
10										0.481	0.471	0.500	0.491	0.482	0.502	0.393	0.386	0.410	10
psummer																			psummer
pautumn	0.384	0.370	0.403																pautumn
winter	0.331						0.455	0.439	0.456							0.368	0.361	0.376	winter
spring	0.380	0.375	0.396				0.526	0.515	0.548	0.513	0.501	0.515				0.493	0.484	0.505	spring
summer							0.445	0.434	0.474	0.513	0.501	0.528	0.476	0.469	0.479	0.491	0.481	0.509	summer
autumn										0.472	0.462	0.490	0.492	0.483	0.502	0.397	0.392	0.417	autumn

Apparently, no direct correlation was found between surface climate and soil moisture data as *SM* is shifted in time compared to surface climatic patterns, with a simultaneous attenuation of extreme values. At greater depths, *SM* changes occur with significant lag (e.g., *Mahmood* and *Hubbard,* 2007; *Venkatesh et al.,* 2011), explained by the complex buffering and balancing capacity of soils. This process may prove favorable for trees, as they may take up water from both the shallower and deeper soil profiles. As the drying up of the deeper soil horizons is delayed, it may supply water for trees during the dry periods, while water is taken up from the shallow subsurface horizons over the rainy periods. This quasi-idealistic approach is shaded by the large spatial and temporal heterogeneity of *SM.* Additionally, different tree species take up water from various depths, i.e., their rhizosphere intrudes to different depths (*Montagnoli et al.,* 2012). Species-specific analyses of rhizosphere depths have been carried out for a limited number of tree species and solely under artificial conditions (*Grossiord et al.,* 2014). For Hungary, *Führer et al.* (2011b) provided detailed information on the general properties, of the rhizosphere and water demand of adult Turkey oaks. The rate of water uptake depends on the root density of the rhizosphere, physical soil properties and water potential (*Nobel,* 1991; *Bréda et al.* 1995). Additionally, due to the phenomena of hydraulic lift, *SM* may be transported from the moist lower soil horizons to the upper and drier soil horizons via the non-suberised radicles, whose Casparian strips are not formed yet (C*aldwell et al.,* 1998; *Jackson et al.,* 2000; *Zapater et al.,* 2011).

Because of the elevated age of the studied trees, their juvenile growth anomalies are commonly excluded from the analyses (*Norgler,* 1981). The early-season frosts may form the so-called frost cracks (*Butin* and *Shigo,* 1981) that directly do not affect tree health, but rather influence wood and timber quality. Presumably, methane-producing bacteria enter into the wood through these cracks. Nonetheless, the source of the methane generation is still subject of debates, some authors explain the process with the anoxic decomposition of the tree interior (*Covey et al.,* 2012), while others believe that methane is taken up via the roots from the soil (*Fender et al.,* 2013). During sampling, no sign of interior rot was found in the studied trees, therefore, in the absence of saturated moisture contents and organic matter, no methane generation is likely in the studied oaks. Complete understanding of the process is preferred, as the presence of methane, having 29 times higher forcing on climate than CO_2, and its subsequent emittance into the atmosphere intensifies the global greenhouse effect (*Rice et al.,* 2010). Consequently, due to their enlarged ecological amplitude, methane emission of Turkey oak may contribute to the increased greenhouse gas emission in the future.

The reduced growth rate of oaks with increasing age, which was removed from the analyzed samples, is not a climatic signal but rather a species-specific genetic nature. Tree growth was extremely slow over the study period, even compared to other test sites of higher water availability for the same period (from 1979 to 2013) indicated by lower-than-average TRW, EWW, and LWW values

(according to the authors' *former unpublished findings*). In extreme cases (*Fig 4*, D20), the width of the EW exceeded that of the LW, indicating extremely arid conditions. Due to the effect of extreme weather patterns, other diseases and pests may further diminish growth rate, however, these biotic factors, due to insufficient data accessibility, are unavailable for direct modeling and encoded in tree structure in a combined manner with climatic markers. The extremely close correlation among the EWW, LWW, and TRW corresponds with the findings of *Gasson* (1987), *Rao et al.* (1997), and *Leal et al.* (2007), according to which, TRW fundamentally determines the anatomical structure of oaks. The authors' *former unpublished findings* disproved these results for oaks that were provided with excess water due to the adjacent springs. EWW and LWW are formed over different times of the growth period (*Schweingruber,* 1993), therefore, the TRW stores different environmental signals as the sum of the EWW and LWW.

In the current study, we found close correlations among EWW, LWW, and TRW, indicating a very similar temporal pattern. This similarity encumbers their correlation with the environmental variables, and the explanation of the anatomical parameters and relation to physiological activities, thus decreasing their temporal resolution.

Many authors have already indicated the primary role of rainfall, and the secondary role of temperature on oak growth (*Haneca et al.,* 2009). Fall precipitation, and especially rainfall totals of the previous September positively correlates with EWW, and this correlation was inherited to the TRW. Exclusively for the EWW, correlation was found with the winter precipitation totals. Formation of the EW vessels at certain areas may occur at the end of the growth season, or in the case of embolism, at the beginning of the growth period, or may be renewed by prior to bud burst (*Lembourgeois et al.*, 2004). It is widely known that even prior to bud burst and the photosynthetically active period, ring-pore trees develop their EW vessels (*Wareing,* 1951; *Aloni,* 1995), therefore, carbohydrates, essential for cell-formation, are allocated from the preserves of the preceding year. In case of oak species, fall is the primary period for the development and storage of sugar and starch (*Lacointe,* 2000, *Barbaroux* and *Bréda,* 2002). *Aloni* (1991) further corroborates this fact, as he pointed out that auxin, essential for activation of the cambium, accumulates during the growth period of the previous year. Therefore, compounds and hormones, vital for cell development, are readily available before bud burst. Accordingly, the width of EW is primarily influenced by the climatic conditions and water budget of the previous fall and winter (*Orcel et al.,* 1992; *Santini et al.,* 1994; *Nola,* 1996). Additionally, vessel lumen area also impacts EW width, while lumen area changes as a function of available moisture. Moreover, commonly close correlation exists between the lumen area of the vessels of EW and LW (*Nola,* 1996; *Tardif,* 1996; *Lembourgeois et al.*, 2004). According to *Lembourgeois et al.* (2004), plant available and uptaken moisture is utilized for the mobilization of carbohydrates. *Sass-Klaassen* et al. (2011) claims the complete lack of EW formation of *Q. robur*

before bud burst, although these findings have not been verified for neither *Q. robur* nor *Q. cerris* by other studies. Our findings are clearly interpretable based on the aforementioned results, although, to identify the exact period of EW formation, multi-year sampling and monitoring is inevitable.

Due to the occasional two-stepped EW formation, signals contained by the EWW may differ in time. Due to the close correlations among the EWW, LWW, and TRW, explanation of this temporal difference is challenging. Nonetheless, all three parameters bear strong, climatic signals of the previous year. Seemingly, due to the environmental stress, trees prepare themselves for the next growth season, and may store and allocate a sufficient amount of carbohydrate for the growth of the subsequent year (*Bréda* and *Granier,* 1996). This process is likely positively influenced by the water supply of the moderately aridifying months. The low correlation with May precipitation is associated with LW development, since EW formation is terminated by this time. Oddly, neither negative, nor positive correlations were observed between the precipitation totals of the driest summer months and anatomical parameters, but it is explainable by the complexity of tree growth, as physiology far exceeds simple correlations (*Anning et al.,* 2013).

Due to the aridification of the area, moisture availability in the soils is highly variable in time. In areas of favorable water availability, *SM* shortage affects water availability in a delayed manner, and soil water potential should approach the permanent wilting point to exert a significant physiological effect on plants to generate distinct signals in the TRW (*Fritts,* 1952).

According to *Meyer* (2002), *SM* plays an important role in the germination of seedlings, and its impact is clearly observable in adult white oaks (*Quercus alba*). With the formation of EW, tree-ring generation is complete in 38% before the bud burst, indicating only a slight difference from *Quercus petreae*, where 43% was measured by *Bréda* and *Granier* (1996) and more than 30% by *Hinckley* and *Lasoie* (1981). Therefore, in theory, the impact of *SM* of the previous growth season on EW and TRW is 38%. During transpiration, plant available water of the capillary pores is taken up (*Nemani* and *Running,* 1989) that principally influences the leaf, and to a lesser degree, the TRW development (*Bréda* and *Granier,* 1996), but overall it supports the entire biomass of the tree (*Legg et al.,* 1979). The triggering factor of transpiration is canopy that develops simultaneously with the LW, therefore, the post-bud-burst (late spring and early summer) *SM* correlations may also be interpreted for LW. Based on our findings, it is obvious, that with increasing time, *SM* located at greater depths is taken up by the trees. In accordance with the conclusions of *Chen et al.* (2008), with decreasing moisture income in the topsoil, SM shortage and water uptake extends to greater depths over elongated dry spells. During late spring and summer, roots transport water, necessary for LW development and maintenance of physiological activities from greater depths. However, no significant correlation was found with *SM58*, which is explained by the time-shift of *SM* with increasing depth. Yet, mean *SM* of the entire profile does not provide sufficient information on the better understanding

of the anatomical patterns of the studied trees, as *SM* correlations at different depth are blurred this way. Correlations between *SM* and anatomical patterns are further refined by *Riedacker* (1976), according to whom, root growth is positively influenced by available *SM*, nutrients, but negatively affected by low soil temperatures. At adequate soil temperatures, root growth remain continuous over the fall months, therefore correlation with fall *SM* is possible.

5. Conclusion

According to our results, the study area has become increasingly dry over the studied period from 1979 to 2013, and the sessile oak-Turkey oak forest climate gradually changes to forest steppe climate. Climatic signals of the D9, D20, and D21, typical for forested grasslands, were persistently dominant. However, the desiccation of soils was undetectable in the model, likely due to the replenishment of soils from the excess moisture of the cooling and more humid months. The excess moisture of the months with increased precipitations and the slightly warming mean temperatures (e.g., March and September) counteract for the water shortage of the intensively aridifying months (e.g., January, April, June, July, August, and November). Moving to greater depths in the modeled soil, a pronounced delay was observable in terms of the impact of *SM* with a simultaneous decrease in *SM* amplitudes. Furthermore, D20 and D21 influenced all anatomical features and *SM* in all depths and correlated with weather data and *FAI*.

Due to the poor soil conditions and climatic aridification, the studied trees have developed sensitivity to environmental changes, hence they bear pronounced climatic signals. Nonetheless, anatomical features, due to their almost identical patterns, hold similar signals that make the interpretation of the observed correlations more challenging.

According to our model-based results, *SM* influences anatomical patterns most significantly among all the studied meteorological and pedological factors. Modeled *SM* impact was clearly detectable to a depth of 30 cm, while poor correlation was found with *SM58*, which is likely explained by the time-delay of SM at greater depths.

The direct impact of rainfall on growth was less pronounced during the growth season than in the preceding September. In contrary to former results, we found a poor correlation between May precipitation totals and growth rate. With the exception of June, correlation between mean monthly temperatures and growth rate were less than $r = 0.33$, therefore, they are not shown in Table 3. Mean June temperature adversely influenced growth rate with $r = –0.367$, $–0.373$, and $–0.377$ for EWW, LWW, and TRW, respectively.

Acknowledgements: The current research was partly funded by the Campus Hungary Higher Education Long Term Mobility Program (TAMOP-4.2.2B/2-11/1,B2/4H/12187). The present scientific contribution is dedicated to the 650th anniversary of the foundation of the University of Pécs, Hungary.

References

Aloni, R., 1991: Wood formation in deciduous hardwood trees. In (Ed.: Raghavendera, A.S.) Physiology of Trees. JohnWiley & Sons, New York, 175–197.

Aloni, R., 1995. The induction of vascular tissues by auxin and cytokinin. In (Ed.: Davis, P.J.) Plant Hormones. Kluwer Academic Publishers, Dordrecht, 531–546.

Anning, A.K., Rubino, D.L., Sutherland, E.K., and *McCarthy, B.C.,* 2013: Dendrochronological analysis of white oak growth patterns across a topographic moisture gradient in southern Ohio. *Dendrochronologia 31*, 120–128.

Auchmoody, L.R. and *Smith, H.C.,* 1979: Oak soil-site relationships in northwestern West Virginia. U.S. Department of Agriculture, Forest Service, Northeastern Forest Experiment Station.

Babák, K., Kiss, I., Kopecskó, Z., Kovács, I.P., and *Schweitzer, F.,* 2013: Regeneration process of the karst water springs in Transdanubian mountains, Hungary. *Hung. Geo. Bull. 62*, 247–265.

Babos, K., 1984: A csertölgy és néhány más fafaj évgyűrűszélessége és az éves csapadék összefüggés-vizsgálata. *Bot. Közlem. 71*, 123–132. (in Hungarian)

Barbaroux, C. and *Bréda, N.*, 2002: Contrasting distribution and seasonal dynamics of carbohydrate reserves in stem wood of adult ring- porous sessile oak and diffuse-porous beech trees. *Tree Physiol. 22*, 1201–1210.

Bartholy, J., Pongrácz, R., Torma, Cs., Pieczka, I., Kardos, P., and *Hunyady, A.,* 2008: Analysis of regional climate change modeling experiments for the Carpathian basin. *Int. J. Glob. Warming 1*, 238–252.

Bidló, A., Berki, A., Király, G., Koloszár, J., Mátyás, C., and *Víg, P.,* 2006: *Magyarország erdészeti tájai.* [Forest regions of Hungary.] Állami Erdészeti Szolgálat, Budapest (in Hungarian)

Bihari, D., 1979: Devecser. A Bakony hegység földtani térképe, 20 000-es sorozat. Magyar Állami Földtani intézet, Budapest (in Hungarian)

Bohn, P., (ed) 1983: Magyarország mélyfúrási alapadatai. II. Közép-Dunántúl, 1851–1973. Magyar Állami Földtani Intézet, Budapest (in Hungarian)

Bréda, N. and *Granier, A.,* 1996: Intra- and interannual variations of transpiration, leaf area index and radial growth of a sessile oak stand (*Quercus petraea*). *Ann. Sci. For. 53*, 521–536.

Bréda, N., Granier, A., and *Aussenac, G., 1995:* Effects of thinning on soil and tree water relations, transpiration and growth in an oak forest *(Quercus petraea (Matt.) Liebl.). Tree Physiology 15,* 295–306.

Butin, H. and *Shigo, A.L.,* 1981: Radial shakes and "frost cracks" in living oak trees. Northeast For. Exp. Stn., Broomall, Pa.

Caldwell, M.M., Dawson, T.E., and *Richards, J.H.*, 1998: Hydraulic lift: consequences of water efflux from the roots of plants. *Oecologia 113*, 151–161.

Chen, X., Rubin, Y., Ma, S., and *Baldocchi, D.,* 2008: Observations and stochastic modeling of soil moisture control on evapotranspiration in a Californian oak savanna. *Water Resour. Res. 44*, 1–13.

Cook, E.R., 1985: A time series approach to tree-ring standardization. Dissertation, University of Arizona.

Covey, K.R., Wood, S.A., Warren, R.J., Lee, X., and *Bradford, M.A.,* 2012: Elevated methane concentrations in trees of an upland forest. *Geophys. Res. Lett. 39,* L15705.

Cufar, K., Grabner, M., Morgós, A., del Castillo, E.M., Merela, M., and *de Luis, M.,* 2014: Common climatic signals affecting oak tree-ring growth in SE Central Europe. *Trees 28*, 1267–1277.

Csóka, Gy., Koltay, A., Hirka, A., and *Janik, G*., 2009: Az aszályosság hatása kocsánytalan tölgyesek és bükkösök egészségi állapotára. *„Klíma-21" Füzetek 57*, 64–73. (in Hungarian)

Di Filippo, A., Alessandrini, A., Biondi, F., Blasi, S., Portoghesi, L., and *Piovensan, G.* 2010: Climate change and oak growth decline: Dendroecology and stand productivity of Turkey oak (*Quercus cerris* L.) old stored coppice in Central Italy. *Ann. For. Sci. 67*, 706–706.

Dövényi, Z. (ed.) 2010: Magyarország kistájainak katasztere. MTA FKI, Budapest. (in Hungarian)

Echeverría, T., Ibarra, P., and *Martínez, J.* 2001: Soil moisture in oak-wood and pine-wood of the Mancayo (Iberian Range, Spain) *Cuadernos de Investigación Geográfica 27*, 17–26.

Eckstein, D., Frisse, E., and *Quiehl, F.,* 1977: Holzanatomische Untersuchungen zum Nachweis anthropogener Einflüsse auf die Umweltbedingungen einer Rotbuche. *Angew. Bot. 51*, 47–56. (in Deutsch)

Fender, A-C., Gansert, D., Jungkunst, H. F., Fiedler, S., Beyer, F., Schützenmeister, K., Thiele, B., Valtanen, K., Polle, A., and *Leuschner, C.* 2013: Root-induced tree species effects on the source/sink strength for greenhouse gases (CH_4, N_2O and CO_2) of a temperate deciduous forest soil. *Soil Biol. Biochem. 57*, 587–597.

Fritts, H.C., 1952: Radial Growth of Beech and Soil Moisture in a Central Ohio Forest during the Growing Season of 1952. *Ohio J. Sci. 56*, 17–28.

Fritts, H.C., 1976: Tree rings and climate. Academic Press, London

Führer, E., 2010: A fák növekedése és a klíma. *„KLÍMA-21" Füzetek 61*, 98–107. (in Hungarian)

Führer, E., Horváth, L., Jagodics, A., Machon, A., and *Szabados, I.,* 2011a: Application of a new aridity index in Hungarian forestry practice. *Időjárás 115*, 205–216.

Führer, E., Czupy, Gy., Kocsisné-Antal, J., and *Jagodics, A.* 2011b*:* Gyökérvizsgálatok bükkös, gyertyános–kocsányos tölgyes és cseres faállományban. *Agrokémia és Talajtan 60*, 103–118. (in Hungarian)

Graiser, R.N., 1951: Relation Between Topography, Soil Characteristics, and the Site index of White Oak in Southeastern Ohio. US Department of Agriculture, Forest Service, *Technical Paper 121*, 12 pp.

Gasson, P., 1987: Some implications of anatomical variations in the wood of pedunculate oak (*Quercus robur* L.). including comparisons with common beech (*Fagus sylvatica* L.). *IAWA J. 8*, 149–166.

Gencsi, L., Vancsura, R., 1992: Dendrológia. Erdészeti növénytan II. Mezőgazda Kiadó, Budapest, 260–267.

Gričar, J., de Luis, M., Hafner, P., and *Levanič, T.,* 2013: Anatomical characteristics and hydrologic signals in tree-rings of oaks (*Quercus robur* L.). *Trees 27*, 1669–1680.

Grossiord, C., Gessler, A., Granier, A., Berger, S., Bréchet, C., Hentschel, R., Hommel, R., Scherer-Lorenzen, M., and *Bonal, D.* 2014: Impact of interspecific interactions on the soil water uptake depth in a young temperate mixed species plantation. *J.f Hydrol. 519*, 3511–3519.

Haneca, K., Čufar, K., and *Beeckman, H.,* 2009: Oaks, tree-rings and wooden cultural heritage: a review of the main characteristics and applications of oak dendrochronology in Europe. *J. Archaeol. Sci. 36*, 1–11.

Hegedüs, P., Czigány, S., Pirkhoffer, E., Balatonyi, E., and *Hickey, R.,* 2015: Analysis of spatial variability of near-surface soil moisture to increase rainfall-runoff modelling accuracy in SW Hungary. *Open Geosci. 7*, 126–139.

Hinckley, T.M. and *Lassoie, J.P.*, 1981: Radial growth in conifers and deciduous trees: a comparison. *Mitt. Forstlichen Bundesversuchsanstalt* (Vienna) *142*, 17–56.

Holmes, R.L., 1983: Computer-assisted quality control in tree-ring dating and measurement. *Tree-Ring Bull. 43*, 69–75.

Jackson, R.B., Sperry, J.S., and *Dawson, T.E.,* 2000: Root water uptake and transport: using physiological processes in global predictions. *Trends Plant Sci. 5*, 482–488.

Jozsa, L.A., 1988: Increment core sampling techniques for high quality cores. Forintek Canada Corporation, Vancouver.

Kern, Z., *Grynaeus, A.,* and *Morgós, A.,* 2009: Reconstructed precipitation for southern Bakony Mountains (Transdanubia, Hungary) back to AD 1746 based on ring widths of oak trees. *Időjárás 113*, 299–314.

Kwiaton, M. and *Wang, J.R.*, 2015: Radial Growth Responses of Four Deciduous Species to Climate Variables in Central Ontario, Canada. *Am. J. Plant Sci. 6*, 2234-2248.

Klimo, E. and *Hager, H.,* 2001: Executive summary. In: (Eds.: *Klimo E, Hager H.*) The floodplain forests in Europe: current situation and perspectives. Brill, Leiden, pp vii–xi.

Kovács, G., Illés, G., Mészáros, D., Szabó, O., Vigh, A., and *Heil, B.,* 2012: A termőhelyi tényezők és a faállományviszonyok kapcsolatának jelenlegi és jövőbeli alakulása a noszlopi erdőtömbben I. *Erdészettud. Közl. 2*, 47–60. (in Hungarian)

Lacointe, A., 2000: Carbon allocation among tree organs: a review of basic processes and representation in functional-structural tree models. *Ann. For. Sci. 57*, 521–533.

Leal, S., Sousa, V.B., and *Pereira, H.,* 2007: Radial variation of vessel size and distribution in cork oak wood (*Quercus suber* L.). *Wood. Sci. Technol. 41*, 339-350.

Legg, B.J., Day, W., Lawlor, D.W., and *Parkinson, K.J.,* 1979: The effects of drought on barley growth: models and measurements showing the relative importance of leaf area and photosynthetic rate. *J. Agric. Sci. 92*, 706–716.

Lembourgeois, F., Cousseau, G., and *Ducos, Y.,* 2004: Climate-tree-growth relationships of *Quercus petraea* Mill. stand in the Forest of Bercé ("Futaie des Clos", Sarthe, France). *Ann. For. Sci. 61*, 1-12.

Mahmood, R. and *Hubbard, K.G.,* 2007: Relationship between soil moisture of near surface and multiple depths of the root zone under heterogeneous land uses and varying hydro climatic condition. *Hydrological Proc. 21*, 3449–3462.

Mátyás, Cs., Führer, E., Berki, I., Csóka, G., Drüszler, Á., Lakatos, F., Móricz, N., Razstovits, E., Somogyi, Z., Veperdi, G., Vig, P. and*, Gálos, B.,* 2010: Erdők a szárazsági határon. *Klíma-21. Füzetek 61*, 84–97. (in Hungarian)

Meyer, V.C., 2002: Soil Moisture Availability as a Factor Affecting Valley Oak (Quercus lobata Neé) Seedling Establishment and Survival in a Riparian Habitat, Cosumnes River Preserve, Sacramento County, California. *USDA Forest Service Gen. Tech. Rep.* PSW-GTR-184, 551–564.

Miniszteri tájékoztató, 2015: Magyarország erdőállományának 2014. évi helyzetéről, állapotáról. www.kormany.hu/download/1/27/80000/tajekoztato_erdoallomany_2014.pdf#!DocumentBrowse. Accessed 2 February 2016. (in Hungarian)

Molnár, S., Peszlen, I., and *Paukó, A.,* 2007: Faanatómia. Szaktudás Kiadó Ház, Budapest. (in Hungarian)

Montagnoli, A., Terzaghi, M., Di Iorio, A., Scippa, G.S., and *Chiatante, D.,* 2012: Fine-root morphological and growth traits in a Turkey-oak stand in relation to seasonal changes in soil moisture in the Southern Apennines, Italy. *Ecol. Res. 27*, 1015–1025.

Móricz, N., Rasztovits, E., Gálos, B., Berki, I., Eredics, A., and *Loibl, W.,* 2013: Modelling the potential distribution of three climate zonal tree species for present and future climate in Hungary. *Acta Silv. Lign. Hung. 9*, 85–96.

Nardini, A., Lo Gullo, M.A., and *Salleo, S.,* 1999: Competitive strategies for water availability in two Mediterranean *Quercus* species. *Plant Cell Environ. 22*, 109–116.

Nardini, A. and *Tyree, M.T.,* 1999: Root and shoot hydraulic conductance seven *Quercus* species. *Ann. For. Sci.* 56, 371–377.

Nemani, R.R.. and *Running, S.W.,* 1989: Testing a theoretical climate-soil-leaf area hydrologic equilibrium of forests using satellite data and ecosystem simulation. *Agric. For. Meteorol. 44*, 245–260.

Nobel, P.S., 1991. Phvsicochemical and environmental plant physiology. San Diego: Academic Press. Inc.

Nola, P., 1996: Climatic signal in earlywood and latewood of deciduous oaks from northern Italy. In (Eds.: *Dean, J.S., Meko, D.M., Swetnam, T.W.*), Tree Rings, Environment and Humanity, Radiocarbon. 249–258.

Norgler, P., 1981: Auskeilende und fehlende Jahrringe in absterbenden Tannen (*Abies alba* Mill.). *Allgemeine Forstzeitung 28*, 709–711. (in Deutsch)

Orcel, A., Orcel, C., Favre, A., Mohnhaupt, M., and *Hurni, J.P.*, 1992: Dendroclimatic model constructed with oakwoods of the Swiss Piémont Jurassien. In (Eds.: *Bartholin, T.S., Berglund, E., Eckstein, D., Schweingruber, F.H., Eggertsson, O.*) Tree Rings and Environment, Proceedings of the International Symposium, Ystad, South Sweden, 3–9 September, 1990, Lund University, Department of Quaternary Geology, Lund. 247–253.

Rao, R.V., Denne, M.P., and *Aebischer, D.P.,* 1997: Latewood density in relation to wood fibre diameter, wall thickness, and fibre and vessel percentages in *Quercus robur* L. *IAWA J 18*, 127-138.

Rice, A.L., Butenhoff, C.L., Shearer, M.J., Teama, D., Rosenstiel, T.N., and *Khalil, M.A.K.*, 2010: Emissions of anaerobically produced methane by trees. *Geophys. Res. Lett. 37*, L03807.

Riedacker, A., 1976: Rythmes de croissance et de régénération des racines des végétaux ligneux, *Ann. Sci. For. 33*, 109–138.

Santini, A., Bottacci, A., and *Gellini, R.*, 1994: Preliminary dendroecological survey on pedunculate oak (*Quercus robur* L.) stands in Tuscany (Italy). *Ann. Sci. For. 51*, 1–10.

Sass-Klaassen, U., Sabajo, C.R., and *den Ouden, J.*, 2011: Vessel formation in relation to leaf phenology in pedunculate oak and European ash. *Dendrochronologia 29*, 171–175

Schweingruber, F.H., 1993: Trees and wood in dendrochronology: Morphological, anatomical, and tree-ring analytical characteristics of trees frequently used in dendrochronology. Springer-Verlag, Berlin, 1–27.

Smith, P., Bustamante, M., Ahammad, H., Clark, H., Dong, H., Elsiddig, E.A., Haberl, H., Harper, R., House, J., Jafari, M., Masera, O., Mbow, C., Ravindranath, N.H., Rice, C.W., Robledo Abad, C., Romanovskaya, A., Sperling, F., and *Tubiello, F.,* 2014: Agriculture, Forestry and Other Land Use (AFOLU). In (Eds.: *Edenhofer, O., Pichs-Madruga, R., Sokona, Y., Farahani, E. Kadner, S., Seyboth, K., Adler, A., Baum, I., Brunner, S., Eickemeier, P., Kriemann, B., Savolainen, J., Schlömer, S., von Stechow, C., Zwickel, T., Minx, J.C.*) Climate Change 2014: Mitigation of Climate Change. Contribution of Working Group III to the Fifth Assessment Report of the Intergovernmental Panel on Climate Change. Cambridge University Press, Cambridge, United Kingdom and New York, NY, USA

Somogyi, Z., 2007: A klíma, a klímaváltozás és a fanövekedés néhány összefüggéséről. In: (Eds.: *Mátyás, Cs*. and *Vig, P*.): Erdő-klíma V. NyME, Sopron. 281–294. (in Hungarian)

Somogyi, Z., 2008: Recent Trends of Tree Growth in Relation to Climate Change in Hungary. *Acta Silv. Lign. Hung*. *4,* 17–27.

Speer, J., H., 2011: Fundamentals of tree-ring research. The University of Arizona Press. Tucson, p 76.

Stafasani, M. and *Toromani, E.,* 2015: Growth-climate response of young Turkey oak (*Quercus cerris* L.) coppice forest stands along longitudinal gradient in Albania. *South-East Eur. Forest. 6*, 25-38.

Stahle, D.W., Cook, E.R., Cleaveland, M.K., Therrell, M.D., Meko, D.M., Grissino-Mayer, H.D., Watson, E., and *Luckman, B.H.,* 2000 Tree-ring data document 16th century megadrought over North America. *EOS Earth Space Sci. News 81*, 121–125.

Stokes, M.A., and *Smiley, T.L.,* 1968: An Introduction to Tree-Ring Dating. University of Chicago Press.

Szabados, I., 2008: A csapadék hatása a cser évgyűrűméretére. *Erdészeti Kutatások 92*, 121–128. (in Hungarian)

Tardif, J. 1996: Earlywood, latewood and total ring width of a ring- porous species (Fraxinus nigra Marsh) in relation to climatic and hydrologic factors. In (Eds.: *Dean, J.S., Meko, D.M., Swetnam T.W.*): Tree Rings, Environment and Humanity. Radiocarbon. Dept. Univ. Arizona, Tucson, 315–324.

Thornthwaite, C.W., 1948. An approach toward a rational classification of climate. *Geograph.rev. 38*, 55–94.

Venkatesh, B., Lakshman, N., Purandara, B.K., and *Reddy, V.B.,* 2011: Analysis of observed soil moisture patterns under different land covers in Western Ghats, India. *J. Hydrol. 397*, 281–294.

Wareing, P.F., 1951: Growth studies in woody species. IV. The initia- tion of cambial activity in ring-porous species. *Physiol. Plant. 4*, 546–562.

Weigl, M., Grabner, M., Helle, G., Schleser, G.H., and *Wimmer, R.,* 2008: Characteristics of radial growth and stable isotopes in a single oak tree to be used in climate studies. *Sci. Total Environ. 393*, 154–161.

Woodhouse, C.A. and *Overpeck, J.T.,* 1998: 2000 years of drought variability in the central United States. *Bull. Amer. Meteorol. Soc.79*, 2693–2714.

Zapater, M., Hossann, C., Breda, N., Brechet, C., Bonal, D., and *Granier, A.,* 2011: Evidence of hydraulic lift in a young beech and oak mixed forest using ^{18}O soil water labelling. *Trees-Struct. Funct. 25*, 885–894.

IDŐJÁRÁS

Quarterly Journal of the Hungarian Meteorological Service
Vol. 121, No. 3, July – September, 2017, pp. 265–284

Leaf area index for common reed (*Phragmites australis*) with different water supplies in the Kis-Balaton wetland, Hungary, during two consecutive seasons (2014 and 2015)

Angéla Anda[1]*, **Gábor Soós**[1], and **Jaime A. Teixeira da Silva**[2]

[1]*Georgikon Faculty, University of Pannonia,*
Festetics Str. 7. Keszthely, H-8360, Hungary

[2]*Ikenobe 3011-2, Kagawa-ken, 761-0799, Japan*

**Corresponding author E-mail: anda-a@georgikon.hu*

(Manuscript received in final form November 5, 2016)

Abstract— Seasonal progression of common reed (*Phragmites australis*) growth has been described by leaf area index (*LAI*), a key variable of crop growth, during two consecutive seasons at the Kis-Balaton wetland (*KBW*) in Hungary. The key objective of this study was to quantify the morphometric variability of *LAI* among common reed beds while distinguishing between established plant canopies with standing water (*SR*) and without water cover (*DR*). Seasonal mean *LAI* of plants with unlimited access to water was 3.21 ± 0.36 and 2.66 ± 0.34 for 2014 and 2015, respectively, while that of plants growing without water cover was 1.11 ± 0.22 and 0.89 ± 0.19. Common reed may be more sensitive to the presence or lack of continuous water cover than to variable weather conditions. Weekly *LAI* curves with two different water supplies as a function of growing degree day *(GDD)* were conducted to estimate the timing of peak *LAI.* Modeling the sums of seasonal evapotranspiration (*ET*) of swamp reed in *SR* showed only slight increases (56.3 mm and 50.8 mm) in 2014 and 2015, respectively. Total *ET* showed significant variation between both seasons, with the 2015 sum of *ET* being almost twice that of 2014. The findings of this study improve our knowledge about the growth of common reed *LAI* under variable weather conditions and water cover. The response of a plant, including *LAI*, to varying environments, may illuminate a course of action in wetland conservation programs. In addition, estimates of *LAI* based on meteorological variables might serve as useful inputs for different *ET* and growth models.

Key-words: common reed, weather impacts, growing degree day, lead area index

1. Introduction

Common reed (*Phragmites australis* (Cav.) Trin. ex Steud.) is a cosmopolitan perennial vascular plant that occupies a wide range of climatic habitats, and is known as the most common wetland plant (*Lambertini et al.*, 2008). In the Northern hemisphere, common reed occurs at latitudes between 70° N and the tropics (*Clevering* and *Lissner*, 1999). Differences in the length of common reed's growing seasons witnessed at different latitudes may be a relatively simple evolutionary adjustment based on temperature (*Clevering et al.*, 2001). Among other stressors such as salinity, nutrient supply, cold or other severe or extreme weather conditions, one of the main ecological stressors in common reed stands that affects its growth capacity is water level (*Bresciani et al.*, 2011, *Engloner*, 2009).

Leaf area index (*LAI*), a key-variable for plant growth, is defined as half the total green leaf surface area per unit ground surface, and is a useful measure of seasonal canopy dynamics (*Savoy* and *Macay*, 2015). Leaf properties should be used as indicators of vegetation activity of the biosphere-atmosphere continuum (*Burba* and *Verma*, 2001). The period of activity of macrohyte vegetation can be typified by the seasonal pattern of green leaf area (*Burba et al.*, 1999). The *LAI* approach that allows plant growth to be monitored also has limitations associated with the time interval (10-14 days or longer) between plant sample collections (*Brenner* and *Ham*, 1999).

Size of the foliage area not only affects plant productivity but almost all characteristics related to the extent of evapotranspiration (*ET*) (*Burba* and *Verma*, 2001). Wetland-to-wetland differences in leaf area cause large variations in canopy *ET*, because one determinant of *ET* is biological control by manipulating the size of foliage (i.e., transpiration) area (*Pedescoll et al.*, 2013).

A concept used worldwide, growing degree days (*GDD*), is based upon the assumption that below a minimum (base) temperature (T_o), plant physiological processes are suspended (*McMaster* and *Wilhelm*, 1997). *Irmak et al.* (2013) suggested 7 °C for common reed T_o when calculating *GDD* for Nebraska, USA.

Zonation of emergent plants is the result of their adaptation to complete flooding and extended dry periods (*Sorrell et al.*, 2000). The phenotypic plasticity of common reed allows it to modify its morphological response by changing the photosynthetic area (*Clevering* and *Lissner*, 1999) hence its importance and link to *LAI*.

Morphological analyses of common reed canopies growing at different water depths frequently provide contradictory results (*Engloner*, 2009) most likely due to differences in observation sites and methods applied. Our area of investigation, the Carpathian Basin, is expected to have drought and floods creating extreme weather conditions with variable inter- and intra-annual temperature and precipitation events. Changeable weather makes the study site worthy of an *LAI* investigation, where summers may display either arid or humid conditions.

There is extremely scant literature that has examined the impact of water cover on common reed leaf expansion. Measurements related to a wetland's *LAI* are still uncommon, because they involve complex and time-consuming processes. To fill this gap, the primary goal of this study was to estimate *LAI* values by using easily accessible meteorological elements. Over a two-year period, two different water covers were studied, equivalent to two seasons in each year. Different models are in use to estimate wetland *ET*, where the most important input related to plant growth is *LAI* (WETSIM: *Poiani* and *Johnson*, 1993; TSEB: *Kustas* and *Norman*, 1999). The second objective of the present investigation was to parametrize *LAI* seasonal variation as an input of these models. Ultimately, we wanted to feature a distinct common reed-specific distribution curve throughout the growing season that was closely related to plant development. Poor analysis of the seasonal change in *LAI* may cause serious inaccuracies in estimating vegetation productivity and transpiration due to the close link between leaf size and carbon fluxes (*Ryu et al.*, 2008). Our results are important for further understanding of wetlands' characteristics, and for protecting their ecological function worldwide.

2. Materials and methods

2.1. Study site

Lake Balaton (surface area: 596 km^2, average depth: 3.25 m, water volume: 1.98 km^3) is a vulnerable shallow freshwater lake in Hungary, closely connected to the Kis-Balaton wetland (KBW), which serves as a filter for the lake. Artificial water reservoirs were also constructed, establishing the Kis-Balaton Water Protection System (KBWPS). As part of a two-step project, Hídvégi Pond (52 km^2, water retention time 30 days) and a part of Fenéki Pond (FP) (16 km^2, water retention period 90 days) started to function in 1985 and 1992, respectively (*Tátrai et al.*, 2000).

The sample site, FP [geographical position: 46º39′N; 17º12′E; mean elevation 104.5 m (max.: 106 m, min.: 103 m) above Baltic Sea level] is located on the south-west side of Lake Balaton (*Fig. 1*), 7.75 km far from the Meteorological Research Station of Keszthely. An average water depth of 0.4–0.6 m is maintained at about one-third of the study area (16 km^2). The remaining part of FP has no constant water cover and only residual water puddles may appear temporarily. The estimated area covered by residual water is less than 1%.

The characteristic soil is organic (peat), formed by excess moisture from groundwater and precipitation, and the shoreline is anchored, allowing it to dissipate erosive forces (*Istvanovics*, 1994).

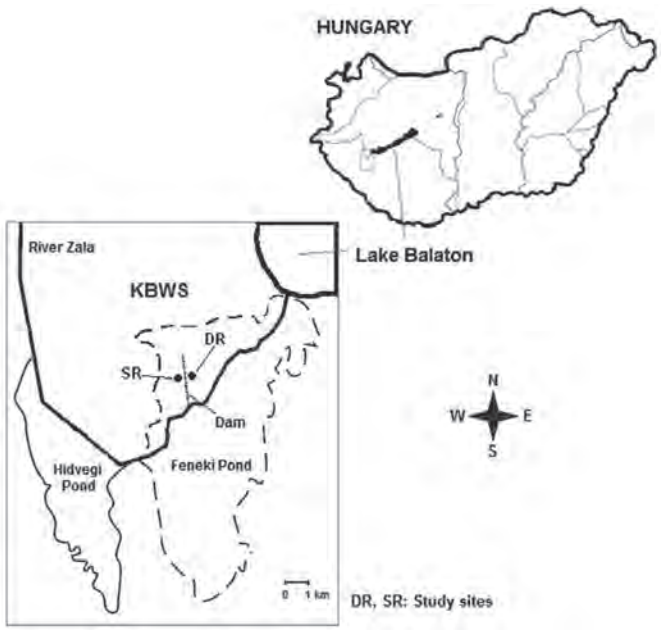

Fig. 1. Map of the Kis-Balaton wetland (KBWS: framed leftward graph) of Hungary, showing the location of Fenéki Pond, FP (study area – bordered by a continuous line) with sampling sites for dryland (DR) and water-covered (SR) common reed stands along the embankment (dam). Hídvégi Pond is highlighted by a dotted line. River Zala is the largest inflow of watershed, and is denoted by a thick line.

2.2. Macrophytes of sample site

Based on on-site macrophyte composition and cover observations (*Anda et al.*, 2014), the dominant emergent macrophytes at FP were common reed, cattail (*Typha angustifolia*, *Typha latifolia*), and sedge (*Carex acutiformis*, *Carex elata*, *Carex riparia*) accounting for about 70% of the canopy cover. The average ratio of the open water surface was only 6% in the long-term (about 30 years). Other minor plant categories, such as shrubs (*Salix cinerea*, *Salix alba*), tree patches (*Salix fragilis*, *Alnus glutinosa*, *Populus tremula*), or grassland (dominant species: *Festuca rupicola*, *Arrhenatherum elatior*, *Alopecurus pratensis*) were also identified with much less than 10% cover (*Anda et al.*, 2014). Common reed was used as the sample plant in our study as it accounted for more than 50% of the macrophyte vegetation cover of FP.

2.3. Weather with meteorological and related ET observations

Meteorological observations were carried out on the northern edge of KBW, at the Meteorological Research Station of Keszthely (latitude: 46°44′, longitude:

17°14′, elevation: 124 m above Baltic Sea level) with a QLC-50 (Vaisala, Helsinki, Finland) automatic climatic station equipped with a CM-3 pyranometer sensor (Kipp & Zonen Corp., Delft, the Netherlands). The combined sensors for air temperature (T_a) and relative humidity (*RH*) measurements were placed at 2 m above the soil surface. Signals from meteorological sensors were collected every 2 s, and 10-min means were logged by the climatic station.

The climate of the study site is temperate continental with an annual mean long-term (1871–2014) T_a of 10.5 °C showing a monthly minimum of –1.1 °C in January and reaching a maximum of 21.1 °C in July. The annual mean precipitation (*P*) is 673.3±137.9 mm with fairly large monthly variation. The monthly mean *P* varies between 32.7 mm and 76.1 mm in the driest January and wettest July, respectively. The rainfall distribution at KBW shows a special character and is concentrated between May and July, contributing to over half of the yearly sum. Yearly precipitation is highly variable due to characteristics of the Carpathian Basin.

The 2014 and 2015 seasons were warm with a T_a of 0.5 ($P(T<=t) = 0.349$) and 0.9°C ($P(T<=t) = 0.048$) higher than its long-term mean (*Table 1*).

Table 1. Mean monthly air temperatures (T_a) and monthly precipitation sums (*P*) for the study seasons. Data were calculated for the time period 1971–2000

	Apr	May	Jun	Jul	Aug	Sep	Oct
T_a [°C] 1971–2000	10.5	15.7	18.7	20.5	20.1	15.7	10.3
***P* [mm] 1971–2000**	50.5	59.6	78.5	73.5	65.1	57.1	49.0
T_a [°C] 2014	12.3	14.7	18.9	21.2	19.1	16.1	12.7
***P* [mm] 2014**	58.6	76.5	59.7	113.1	148.1	159.7	68.3
T_a [°C] 2015	10.8	15.6	19.5	22.9	22.6	16.6	9.7
***P* [mm] 2015**	4.0	102.3	20.9	60.9	70.3	62.9	151.6

Climatic norms of 1971–2000 were applied for comparison, and the *P* of both experimental seasons was contrasted. In the wetter year, 2014, the rainfall sum during the vegetation season was 44.8% ($P(T<=t = 0.035$) higher than the long-term average. By contrast, the growing season was dry in 2015, with 8.7% ($P(T<=t) = 0.794$) less than long-term mean sum of rainfall. However, the summer of 2015 was even drier, and the lack of rain water until September 1 was 17.9% lower than the climatic norm. The 156 mm monthly precipitation in October raised the seasonal mean precipitation of 2015, which might be considered to be less decisive for common reed development. Interannual variation in monthly mean T_a was large in July, +1.0 and +1.7 °C higher than the long-term average in 2014 and 2015, respectively, corresponding to the most

sensitive period of common reed growth patterns. In September 2014, serious flooding events occurred which increased the surface water level in part of the studied area (*Fig. 2*). The FP water level rose from 0.6–0.7 m in April to 1–1.5 m in September. At the same time, the area of our second (dry) sample site remained dry, without any surface water cover.

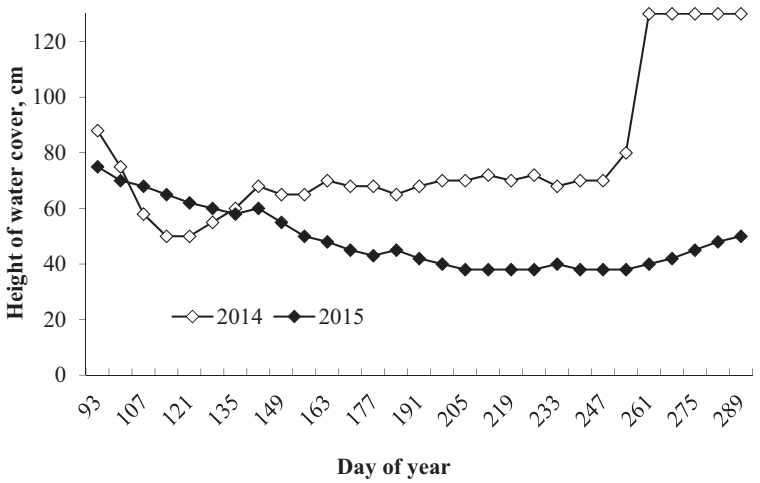

Fig. 2. Seasonal trend of standing water level measured on-site of SR relative to surface (0 cm) during the two seasons. In DR there was no standing water in both summers.

On the basis of six years of on-site observations, the *ET* of the reed bed was modeled using an earlier tested empirical approach for warm seasons (*Anda et al.*, 2014):

$$ET = 0.142R_n + 0.211T_a - 0.042RH + 0.134LAI + 1.082, \quad (1)$$

where R_n is the net radiation.

This model works on a daily basis. In this study, weekly *ET* sums were presented for two water levels, i.e., common reed standing in water (SR) and plants without water cover (DR).

2.4. Plant observations

In the present study, we distinguished *a priori* two different stand morphotypes (treatments) of common reed as the dominant macrophyte of FP:

– Plants standing in water, where evaporation from the water body would be limited only by available energy under the given surface and atmospheric conditions. These plants were grown in swampland areas (swamp-reed, or SR).

– Plants of dryland conditions (dry-reed, or DR), located at the foot of land sloping down to FP, where the latent heat, including evaporation, would be limited due to shortcomings in soil moisture.

Measurements of weekly *LAI* (dimensionless: size of green leaf area [m^2] above unit ground surface [m^2]) were used to estimate vegetation growth. After the plants emerged, leaf area was measured on 10 randomly chosen sample shoots every week using a portable automatic planimeter (LI-3000A, LI-COR Inc., Lincoln, NE, USA). Shoots that were selected were characteristic of the whole canopy plant stand within each water treatment. After manually counting shoot density from five subplots with an area of 0.25 m^2 within the wetland for each treatment, *LAI* was expressed every week. *LAI* measurements started when it was approximately 0.1–0.3 (day of year, *DOY* ~100), similar to earlier studies on common reed growth patterns (*Irmak et al.*, 2013, *Burba et al.*, 1999).

The *LAI* values were regressed against daily cumulative *GDD.* When calculating *GDD* for common reed, we used 7 °C as the base temperature T_o, because the on-site observed temperature for common reed emergence coincided with 7 °C in the first half of April:

$$GDD = \sum(T_a - T_0), \tag{2}$$

in which both temperatures, T_a and T_0, were considered on a daily basis.

2.5. Statistics

To compare the impacts of two water levels, a two-tailed *t*-test was used. Two-way analysis of variance (ANOVA/*t*-test) was performed to examine the impact of seasons and water cover on *LAI*. Differences were considered to be significant at $\alpha = 0.05$.

Multiple stepwise regression analysis was used to assess the influence of meteorological variables on *LAI*. To compare measured and simulated (based on meteorological variables) *LAI*, a linear regression ($y = a + bx$) was used (measured *LAI* data as dependent variable *y*, simulated *LAI* as independent variable *x*). The accuracy of the estimate was considered to be acceptable when the slope forced through the origin of the regression (1:1 line) was not significantly different from 1. All tests were carried out with SPSS Statistics version 17.0 software (IBM Corp., New York, USA).

3. Results

3.1. Impact of meteorological elements on LAI

Among the weekly-based meteorological variables, T_a, *RH*, and *P* were included in the analysis (*Table 2*). In both seasons, T_a influenced *LAI* the most (r = 0.78 – 0.9), irrespective of water supply. In 2014, only a mild correlation was found between *LAI* and *P* (r = 0.45 – 0.46). In 2015, the r values for *P* were 0.00 – 0.01 in both water supplies, when water shortage (summer drought) occurred. Irrespective of the season, a weak negative correlation was demonstrated for *RH* in both water levels ranging from r = 0.00 to –0.14. A high positive correlation was observed between the *LAI*s of the two water supplies (r = 0.99 – 0.99 for both water supplies). The probability levels are presented in *Table 2*.

Table 2. Correlation coefficients (r) for weekly mean leaf area index, *LAI* in dryland region (DR) and common reed stand with water cover (SR) during a two-season (2014–2015) study. T_a: weekly mean air temperature; *RH*: weekly mean relative humidity; *P*: weekly precipitation sum. Number of observations was 27 in 2014 and 32 in 2015 for each correlation

Season	T_a [°C]	*RH* [%]	*P* [mm]
DR-2014	0.783***	–0.036	0.448*
SR-2014	0.778***	–0.060	0.456*
DR-2015	0.9***	–0.009	–0.004
SR-2015	0.904***	0.005	0.011

* Marginally significant correlation |r|>0.1, p<0.01
** Marginally significant correlation |r||>0.1, p<0.001
*** Significant correlation |r||>0.4, p<0.0001

3.2. Growth curve for LAI

There was a gradual increase in weekly *LAI* until peak *LAI* and then a decline throughout both growing seasons associated with plant biological characteristics and meteorological conditions (*Fig. 3*). Irrespective of the year and water supply, leaves started to expand in April (*DOY*: 90–93), and exhibited an increasing trend with longer periods of solar radiation until the end of July (*DOY*: 200–205) corresponding to the most intense growth of common reed (*Fig. 3*). Thereafter, *LAI* decreased parallel to the decline in radiation throughout the remainder of the growing season (*DOY*: 290–294). The length of the growing season was about one week longer in 2014 than in 2015 (data not shown).

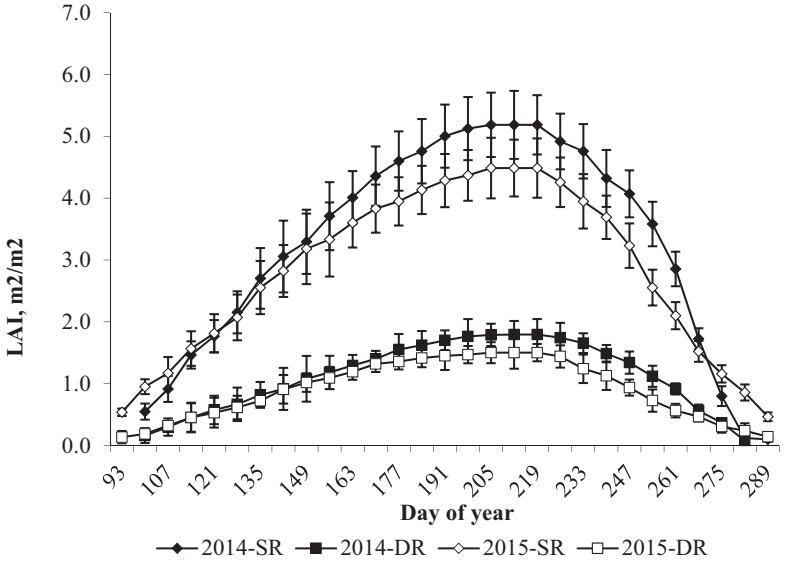

Fig. 3. Seasonal pattern of weekly mean leaf area index, *LAI,* in two growing seasons (2014 and 2015). DR and SR represent common reed without water cover and crops standing in water, respectively.

Weekly mean *LAI* in 2014 ranged from 0.1 to 0.3 at the beginning and at the end of the growing season, reaching 1.79 and 5.19 in DR and SR, respectively (*Fig. 3*). However, the initial and final *LAI* values remained similar for 2015, and the peak values were 1.50 for DR and 4.49 for SR. At both sites, maximum *LAI* peaked in the last 10 days of July, irrespective of seasonal weather. Seasonal means of common reed *LAI* with unlimited access to water were 3.21 ± 0.36 and 2.66 ± 0.34 for 2014 and 2015, respectively. The *LAI* of plants in DR were 1.11 ± 0.22 and 0.89 ± 0.19 for the same time period. Maximum average *LAI* of SR was 4.84 for the two growing seasons and was higher than the mean *LAI* of both seasons for DR, namely 1.64.

The response of common reed *LAI* to changing water level in the two seasons was similar: water shortage significantly decreased seasonal mean *LAI* by 99.7% ($P(T<=t) = 0.0001$) and 97.2% ($P(T<=t = 0.0001$) in 2014 and 2015, respectively. In the wet 2014 season, seasonal mean *LAI* was 21.1% ($P(T<=t) = 0.140$) and 18.7% ($P(T<=t) = 0.032$) higher in DR and SR, respectively, than in the dry 2015 season.

There are two basic factors that affect *LAI*, the size of the green leaf area per shoot and the shoot density. The impact of weather on seasonal mean leaf area per shoot was less pronounced, as only a 2.3% ($P(T<=t) = 0.366$) and 6.5%

($P(T<=t = 0.003$) increment in favor of wet 2014 was observed for SR and DR, respectively. In contrast, the effect of water cover was at least two-fold higher and the average leaf area per shoot in SR and DR was 12.2% ($P(T<=t) = 0.0001$) and 16.4% ($P(T<=t) = 0.0001$) higher in 2014 and 2015, respectively. Based on a two-season average, the mean shoot density for DR and SR stands was 22 ± 8.21 and 58 ± 21.64 shoot m^{-2}. No significant differences in shoot density between both seasons were observed [DR: ($P(T<=t) = 0.735$); SR: ($P(T<=t = 0.697$)]. The lack of water cover resulted in a 90.5% ($P(T<=t = 0.012$) and 90.9% ($P(T<=t) = 0.020$) decrease in average shoot density in the 2014 and 2015 growing seasons, respectively.

The maximum number of leaves on culms was 11.6 ± 3.0, 13.6 ± 2.33, 12 ± 2.45 and 14.4 ± 3.44 in DR (2014), SR (2014), DR (2015) and SR (2015), respectively, during flowering. The number of leaves per shoot was not strongly linked to season or water supply. This latter parameter tended to increase in approximately two leaf layers ($P(T<=t) = 0.129$ and $P(T<=t) = 0.061$ in 2014 and 2015, respectively) in SR stands. The change in the number of leaves between the seasons was also not significant (SR: $P(T<=t) = 0.541$; DR: $P(T<=t) = 0.648$).

Changes in seasonal *LAI* trends were plotted as a function of *GDD* (*Fig. 4*). Although the best fit was a three-degree polynomial in all treatments, the trend of the curves was impacted by different water supply levels, irrespective of the season (*Fig. 5*).

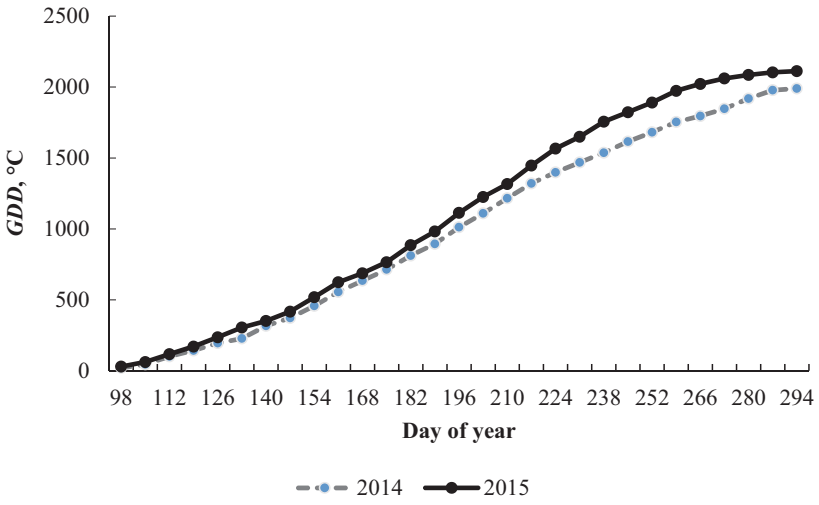

Fig. 4. Cumulative growing degree day, *GDD* (base temperature of 7°C) for common reed at the Kis-Balaton wetland, Hungary during the 2014 and 2015 growing seasons.

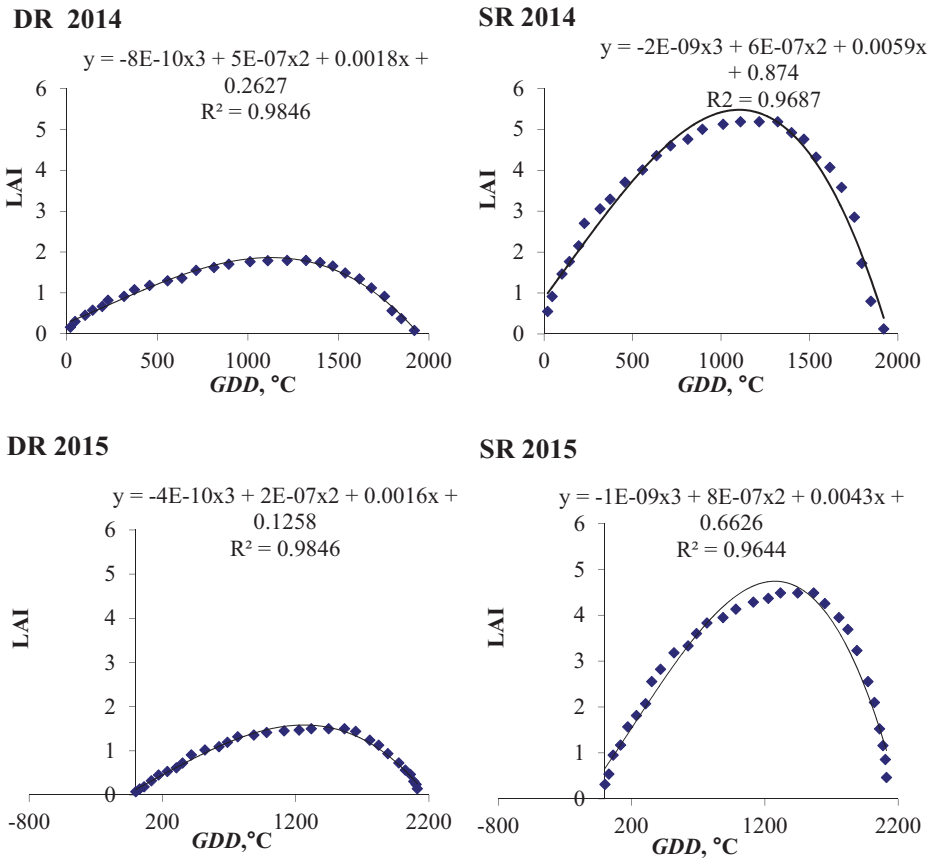

Fig. 5. Seasonal variation in weekly mean *LAI* for common reed as a function of growing degree days, *GDD* in 2014 and 2015. DR and SR represent common reed without water cover and crops standing in water, respectively.

In 2014, the cumulative *GDD* value was 1990 °C, whereas it was 2112 °C at the end of October in 2015 (*Fig. 4*). *GDD* curves were concurrent until the end of July. *LAI* curves for common reed in SR and DR zones were developed as a function of *GDD* (*Fig. 5*). Although the slopes and intercepts of the treatments that were studied differed, every curve followed a lowest applicable third-degree polynomial function with high R^2 and similar data scatter. The time at which peak *LAI* appeared (*DOY*: 200–210) was close to other *DOY* values in each water level. During peak *LAI*, a 300–400 °C higher *GDD* was measured in the warmer 2015 than in the 2014 season.

3.3. Estimation of common reed evaporation based on LAI measurements

The daily *ET* rates presented an obvious seasonal pattern. In 2014, daily mean *ET* rates averaged 4.2 and 4.5 mm day^{-1}, with a range of 0.2 to 8.1 and 0.4 to 8.5 mm day^{-1} for DR and SR, respectively. A moderate increase was observed in 2015 when daily *ET* rate means were 4.8 and 5.1 mm day^{-1}, with a range of 0.2–8.7 and 0.4–9.1 mm day^{-1}, for DR and SR, respectively.

Based on weekly *LAI* measurements, seasonal variations in weekly *ET* totals were plotted (*Fig. 6*). In both growing seasons, weekly *ET* sums followed the pattern of *LAI* and solar radiation. *ET* sums increased from about 13–15 mm week^{-1} in April to a peak magnitude of about 50 – 60 mm week^{-1} during July, and then decreased to below 16 –18 mm week^{-1} during October.

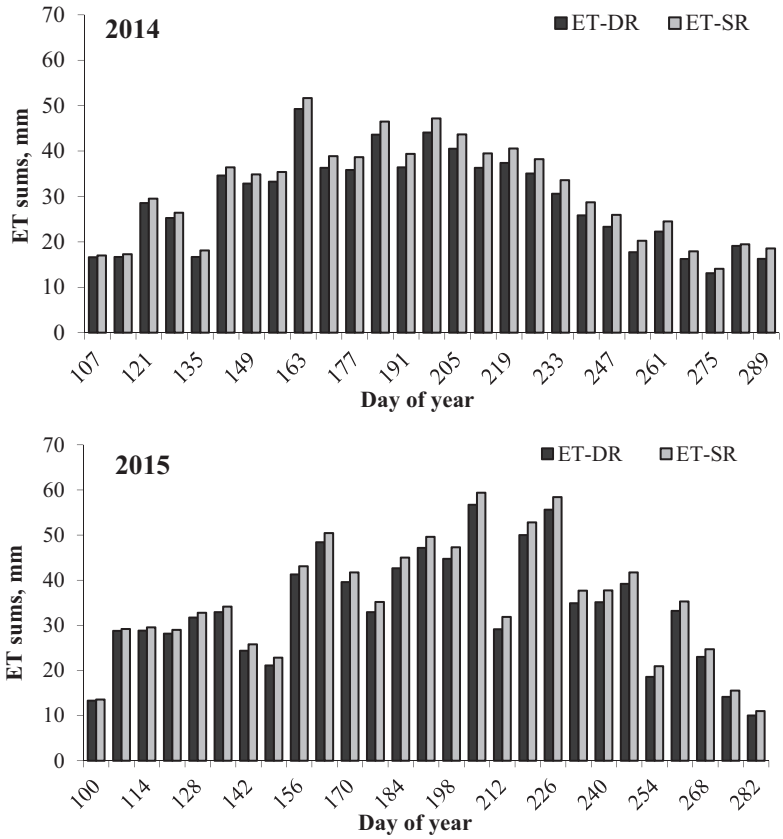

Fig. 6. Model results of weekly evapotranspiration (*ET*) sums for the 2014 and 2015 seasons. ET-DR and ET-SR represent common reed *ET* without water cover and crops standing in water, respectively.

Deviations of daily *ET* rates between seasons and water supply levels were highly significant. In the warm 2015 season, daily mean *ET* rates were larger than the *ET* rates of the previous wet season of 2014, with 13.3% ($P(T<=t) = 0.0001$) in DR and 12.5% $P(T<=t) = 0.0001$) in SR. The impact of changing water level was less noticeable and only 6.9% ($P(T<=t) = 0.004$) and 5.5% ($P(T<=t) = 0.0001$) increases were modelled for 2014 and 2015, respectively.

4. Discussion

4.1. Impact of weather

In this study, *LAI* was strongly correlated with weekly mean T_a, independently of the presence of standing water: 0.9 °C higher seasonal mean T_a in 2015 caused 18.7% and 21% lower mean *LAI* in SR and DR, respectively. Similar to our investigation, an increase in T_a of 1.5 °C reduced the *LAI* of common reed by 27% when averaged across the growing season at Yangtze Estuary, China (31°38′ N, 121° 58 ′ E) (*Zhong et al.*, 2014).

Univariate ANOVA showed a significant effect of season ($P(T<=t) = 0.008$) and water level ($P(T<=t = 0.0001$) on *LAI*, but there was no interaction between both variables, i.e., season × water ($P(T<=t) = 0.193$) (*Table 3*).

Table 3. Univariate analysis of variance for weekly mean leaf area index, *LAI,* compared to all treatments (2014 and 2015 seasons; two water supplies)

Source	Type III Sum of Squares	df	Mean Square	F	Sig.
Corrected Model	19.821[a]	3	6.607	81.444	.000
Intercept	77.028	1	77.028	949.499	.000
Season	.757	1	.757	9.326	.008
Water level	18.915	1	18.915	233.160	.000
Season × water level	.150	1	.150	1.845	.193
Error	1.298	16	.081		
Total	98.148	20			
Corrected Total	21.119	19			

[a.] $R^2 = 0.939$ (Adjusted $R^2 = 0.927$)

The quality of the influence, i.e., the correlation coefficient for *P*, was negligible not only in plant stands with no limited access to water (SR), but in the DR canopy as well. In 2014, multiple stepwise regression, in some cases, including three candidate explanatory meteorological elements (T_a, *RH*, and *P*)

in both SR and DR, produced more accurate results than a single correlation, because *LAI* responded to other meteorological factors as well. The adjusted coefficient of determination (r^2) produced by SPSS was used to check the model. In 2014, the best projections were those equations containing all meteorological elements (*Table 4*). In the next season, probably due to a dry summer, *P* and *RH* were excluded from the estimate. Stepwise regression analysis indicated that irrespectively of season and water supply, T_a was the driving force for *LAI* growth at the study site.

Table 4. Multiple stepwise regression models to predict leaf area index (*LAI*) from meteorological variables (T_a: weekly mean air temperature; *RH*: weekly mean relative humidity; *P*: weekly precipitation sum). Model fit was controlled by adjusted r^2

	Adjusted R^2	F	F sig.	SE of coefficient	Regression equation
DR-2014/1	0.597	39.567	0.000	Const.=0.337 T_a=0.019	LAI_{DR}=0.121T_a–0.964
DR-2014/2	0.756	41.268	0.000	T_a=0.759 *P*=0.403	LAI_{DR}=0.118T_a–0.011*P*–1.145
DR-2014/3	0.790	33.669	0.000	T_a=0.717 *P*=0.546 *RH*=–0.247	LAI_{DR}=0.111T_a+0.015*P*+0.021*RH*+0.521
SR-2014/1	0.589	38.26	0.000	Const.=0.988 T_a=0.056	LAI_{SR}=0.349T_a–2.645
SR-2014/2	0.755	41.141	0.000	Const.=0.773 T_a=0.044 *P*=0.008	LAI_{SR}=0.338T_a+0.033*P*–3.180
SR-2014/3	0.808	37.458	0.000	Const.=2.189 T_a=0.039 *P*=0.008 *RH*=0.027	LAI_{SR}=0.316T_a+0.46*P*–0.073*RH*+2.539
DR-2015	0.805	128.593	0.000	Const.=0.127 T_a=0.007	LAI_{DR}=0.083T_a–0.546
SR-2015	0.811	134.390	0.000	Const.=0.355 T_a=0.020	LAI_{SR}=0.237T_a–1.325

4.2. Common reed growth

In 2015, growth initiation was delayed by about one week compared to 2014, due to lower spring temperatures. This may be one reason why the mean peak *LAI* was also lower. *Soetaert et al.* (2004) found a pronounced effect of

postponing growth initiation (i.e., late timing of bud burst in spring) on common reed growth characteristics, including *LAI*.

The peak *LAI* was calculated from the inflection points of *Fig. 5* as the second derivative of the third-degree polynomial. Good agreement was found in calculated and measured *LAI* peaks (*Fig. 7*).

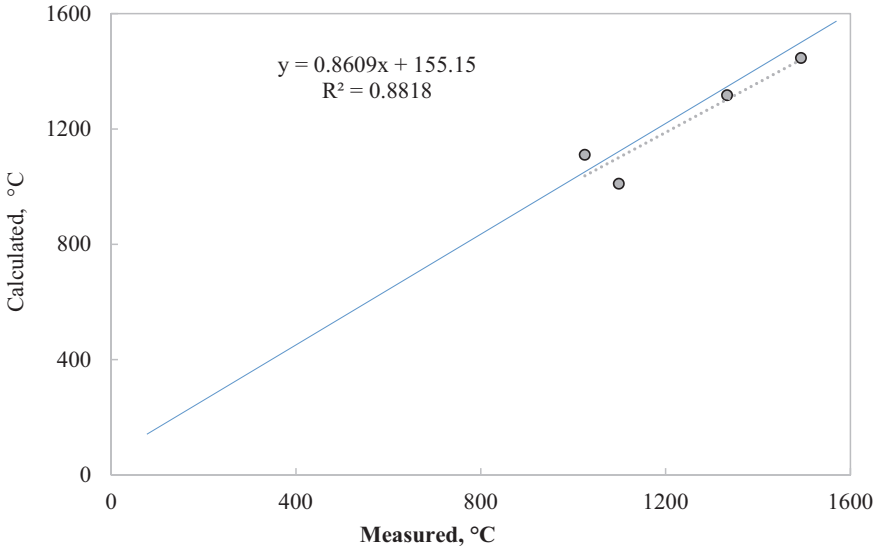

Fig. 7. Comparison of measured (*Fig. 3*) and calculated peak *LAI* using GDD concept during the 2014 and 2015 study period. The four calculated peak *LAI* are the inflection points determined from the 2nd derivative of the third-degree polynomials of *Fig. 5*.

Peak *LAI* was followed by plant senescence, and *LAI* values continued to decline slightly until the end of October (*GDD* ~ 2000 °C). Based on slopes of fitted least squared linear regression lines, there was significant variation in the descending branch (leaf withering) of weekly *LAI* curves (*Table 5*). Different slopes were found in the two growing seasons for each of the two water supplies. On the basis of these slopes, the steepest curve was observed in SR during 2014. Flooding during the fall of 2014 might have been the responsible driver of intense *LAI* decline in the SR canopy. In 2015, a more intense slope was also observed for SR than for DR.

Table 5. Linear regression equations (with slopes) of curves fitted to descendent branches of leaf area index, *LAI* vs. growing degree day, GDD (2014–2015). Abbreviations DR and SR are as in *Table 2*

Treatment	Regression equation	r^2
DR-2014	–0.0033x + 2.1632	0.96
SR-2014	–0.014x + 5.4377	0.97
DR-2015	–0.003x + 1.6331	0.97
SR-2015	–0.010x + 4.5386	0.97

Irrespectively of the season, the *LAI-GDD* curves were not identical on both sides of the graph, i.e., asymmetry was displayed, and the slopes of descending branches (leaf withering) were steeper than the ascending slopes (*Fig. 5*). The largest deviation in 2014 was associated with adverse meteorological conditions, mainly in the SR canopy. This part of the wetland was submerged in fall, and heavy storms and rough waves might have sped up leaf degradation. In all other periods, the water level of SR was at a constant height. In contrast, in the same time period, there was no water cover in DR. Two different water supplies in this study reflected differences in common reed *LAI* in wetland habitats due to changing water levels. *Windham* (1999) reported that, within a marsh, there are variations in the rate of expansion of common reed that are related to micro-site variations in water level.

Bresciani et al. (2011) found that water level is a driving factor for changes in *LAI* by forcing an abundance of stems in common reed at the lakeshore of Lake Garda, Italy. *Russell* and *Kraaij* (2008) found that common reed in wet zones formed more shoots (i.e., greater shoot density) than in drier zones in a South African estuarine lake system. In our study, the enhanced *LAI* of SR in both seasons is attributed to the constant (~0.5 m) water cover that induced higher shoot density. Irrespectively of the season, about 90% ($P(T<=t) = 0.012$–0.02) more shoots were counted in the SR stand (data not shown), similar to the observations of *Russell* and *Kraaij* (2008) in South Africa and *Coops et al.*, (2004) in the Netherlands for common reed stands with a 30–80 cm water depth. However, there are also some studies that show higher shoot density for common reed in dryland conditions (*Engloner*, 2004; *Bodensteiner* and *Gabriel*, 2003). *Coops et al.* (2004) investigated common reed expansion with fluctuating water levels at freshwater Lake Volkerak-Zoommeer in the Netherlands. The authors found that the best height of aboveground water level ranged between 25 and 40 cm, close to our standing water level. In our study, height of the water cover increased by 1–1.5 m only temporarily due to flooding in September 2014, which enhanced leaf withering (*Fig. 3*). Results of our study are comparable

with those of *Hudon et al.* (2005) for Quebec, Canada, in which common reed retreated when the water level in summer was higher than 50 cm.

A significant decline of 18.7% ($P(T<=t) = 0.032$) was observed in mean *LAI* of SR during 2015. At the same time, a 21.0% ($P(T<=t) = 0.140$) decrease in average *LAI* of DR stands was observed (*Fig. 3*). In the case of DR, warm weather in 2015 did not further enhance the negative impact resulting from the lack of water cover. Our investigations may be valid for shorter time periods only, as common reed is a wetland's macrophyte demanding fluctuating water cover for a longer time period (*Engloner*, 2009).

There was rather sharp decrease in the maximum *LAI* of DR due to limited water. Declines for DR were 97.1% ($P(T<=t) = 0.0001$) and 100% ($P(T<=t) = 0.0001$) for 2014 and 2015, respectively. When there was unlimited access to water, a 14.4% difference ($P(T<=t) = 0.045$) was found in seasonal peak *LAI*, in favor of the humid season in 2014. Peak *LAI* of the SR stand was intermediate between the results of *Zhou* and *Zhou* (2009) and *Herbst* and *Kappen* (1999) for reed wetland in northeast China (41° 08′ N) and Germany (54° 06′ N), respectively. The maximum *LAI* of the dryland reed stand was much lower than that observed in the literature (close common reed peak *LAI* results were published by *Sun* and *Song* (2008) for Sanjiang Plain, Northeast China, 47°35′N), and it can be attributed to on-site lack of water cover that is not a common and long-lasting occurrence in wetland habitats.

Using temporal variation in *LAI*, we are able to derive the complete seasonal progression of canopy growth dynamics. Thus, *LAI* serves as a suitable metric that quantifies seasonal patterns in plant development (*Savoy* and *Mackay*, 2015).

4.3. Estimation of ET for common reed

An empirical *ET* model developed using meteorological and a plant factor (*LAI*) was able to estimate differences in common reed *ET* rates with altered water supply with reasonable accuracy. Differences were noticed in total *ET* when both water supply and season were assessed. Modeling seasonal *ET* sums of SR showed only a slight increase of 56.3 mm and 50.8 mm in 2014 and 2015, respectively. *ET* total showed significant variation between both seasons, with the *ET* sum of 2015 being almost twice that of 2014 (118.8 mm in DR and 113.3 mm in SR). Changes in weather conditions might be responsible for interannual *ET* variation. *ET* has long been known to vary due to meteorological conditions (*Drexler et al.*, 2008), mainly due to available energy.

The modeled 4.2–5.1 mm of daily mean *ET* rates for common reed at the Kis-Balaton wetland in the current study shows a slightly higher value than the 4.3–4.4 mm daily mean *ET* rates reported by *Irmak et al.* (2013) for 2009 and 2010 and *Lenters et al.* (2011) for 2009 in Nebraska (40°17 ′ N and 41°79 ′ N) at slightly lower latitudes than our study site. During 2014, due to extreme wet

weather (and lower air temperatures), total *ET* of 783–842 mm per season was lower than the values reported by *Anda et al.* (2015) according to a 16-year mean on-site *ET* total of 807 mm.

5. Conclusions

Common reed *LAI* was negatively impacted by water limiting conditions, irrespectively of the season. Despite the fact that plants with unlimited access to water showed a similar seasonal trend in leaf growth with common reed standing in water, a significant change in the size of *LAI* was observed. In our two-season study, common reed seemed to be more sensitive to the presence or lack of continuous water cover than to variable seasonal weather conditions.

Comparison of the *GDD*-based estimates for peak *LAI* with measured values showed that the performance of a third-degree polynomial model was acceptable to project maximum *LAI* in two water supply levels. Peak *LAI* was projected between ~1000 °C (wet season) and ~1200 °C (dry season) *GDD* values.

The larger the *LAI* (stand density), the larger the *ET* rates (totals) observed during the two-season monitoring period. In spite of abundant literature about the impact of fluctuating water levels on *ET* and biomass of common reed belts, less information is available about changing architecture (*LAI*) of plants due to variable water conditions. *Ehrenfeld* (2000) stressed the importance of structural alteration of hydro-hygrophilous environments as one of the causes of wetland degradation. Results of our study on common reed *LAI* grown in both wet and dry conditions may contribute to avoid this negative phenomenon of natural wetlands. *LAI* estimates based on meteorological variables may provide useful inputs for *ET* and growth models.

Acknowledgement: We thank our student *Angéla Szanati* for help in sampling at the Kis-Balaton wetland.

References

Anda, A., Soos, G., and *Teixeira da Silva, J.A.,* 2015: Regional evapotranspiration from a wetland in Central Europe, in a 16-year period without human intervention. *Agric Forest Meteorol 205*, 60–72.

Anda, A., Teixeira da Silva J.A., and *Soos, G.,* 2014: Evapotranspiration and crop coefficient of common reed at the surroundings of Lake Balaton, Hungary. *Aquat Bot 116*, 53–59.

Brenner, D.J. and *Ham, J.M.,* 1999: Effects of spring burning on the surface energy balance in a tallgrass prairie. *Agric Forest Meteorol 97,* 43–54.

Bodensteiner, L.R. and *Gabriel, A.O.,* 2003: Response of mid-water common reed stands to water level variation and winter conditions in Lake Poygan, Wisconsin, USA. *Aquat Bot 76*, 49–64.

Bresciani, M., Sotgia, C., Fila, G.L., Musanti, M., and *Bolpagni, R.,* 2011: Assessing common reed bed health and management strategies in Lake Garda (Italy) by means of Leaf Area Index measurements. *Ital J Remote Sens 43*, 9–22.

Burba, G.G., Verma, S.B., and *Kim, J.*, 1999: Surface energy fluxes of *Phragmites australis* in a prairie wetland. *Agric Forest Meteorol 94*, 31–51.
Burba, G.G. and *Verma, S.B.,* 2001: Prairie growth, PAR albedo and seasonal distribution of energy fluxes. *Agric Forest Meteorol 107*, 227–240.
Clevering, O.A., Brix, H., and *Lukavská, J.,* 2001: Geographic variation in growth responses in *Phragmites australis*. *Aquat Bot 69*, 89–108.
Clevering, O.A. and *Lissner, J.,* 1999: Taxonomy, chromosome numbers, clonal diversity and population dynamics of *Phragmites australis* (Cav.) Trin. ex Steud. *Aquat Bot 64*, 185–208.
Coops, H., Theo, Vulink, J.T, and *van Nes E.H.,* 2004: Managed water levels and the expansion of emergent vegetation along a lakeshore. *Limnologica 34,* 57–64.
Drexler, J.Z., Anderson, F.E., and *Snyder, R.L.,* 2008: Evapotranspiration rates and crop coefficients for a restored marsh in the Sacramento-San Joaquin Delta, California, USA. *Hydrol Process 22*, 725–735.
Ehrenfeld, J.C., 2000: Evaluating wetlands within an urban context. *Ecol Engin 15*, 253–265.
Engloner, A., 2009: Structure, growth dynamics and biomass of reed (*Phragmites australis*) – A review. *Flora 204*, 331–346.
Engloner, A., 2004: Annual growth dynamics and morphological differences of reed (*Phragmites australis* [Cav.] Trin. ex Steudel) in relation to water supply. *Flora 199*, 256–262.
Fogli, S., Brancaleoni, L., Lambertini, C., and *Gerdol, R.,* 2014: Mowing regime has different effects on reed stands in relation to habitat. *J Environ Manage 134,* 56–62.
Herbst, M., and *Kappen, L.,* 1999: The ratio of transpiration versus evaporation in a reed belt as influenced by weather conditions. *Aquat Bot 63*, 113–125.
Irmak, S., Kabenge, I., Rudnicka, D., Knezevic, S., Woodward, D., and *Moravek M.,* 2013: Evapotranspiration crop coefficients for mixed riparian plant community and transpiration crop coefficients for common reed, cottonwood and peach-leaf willow in the Platte River Basin, Nebraska-USA. *J Hydrol 481*, 177–190.
Hudon, C., Gagnon, P., and *Jean, M.*, 2005: Hydrological factors controlling the spread of common reed (*Phragmites australis*) in the St. Lawrence River (Québec, Canada). *Ecoscience 12*, 347–357.
Istvanovics, V., 1994: Fractional composition, adsorption and release of sediment phosphorus in the Kis-Balaton reservoir. *Wat Res 28,* 717–726.
Kustas, W.P. and *Norman, J.M.*, 1999: Reply to comments about the basic equations of dual-source vegetation-atmosphere transfer models. *Agric Forest Meteorol* 94:275-278.
Lambertini, C., Gustafsson, M.H.G., Frydenberg, J., Speranza, M., and *Brix, H.,* 2008: Genetic diversity patterns in *Phragmites australis* at the population, regional, and continental scales. *Aquat Bot* 88:160–170.
Lenters, J.D., Cutrell, G.J., Istanbulluoglu, E., Scott, D.T., Herrman, K.S., Irmak, A., and *Eisenhauer, D.E.,* 2011: Seasonal energy and water balance of a *Phragmites australis*-dominated wetland in the Republican River basin of south-central Nebraska (USA). *J Hydrol 408*, 19–34.
Mc Master, G.S. and *Wilhelm, W.W.*, 1997: Growing degree-days: one equation, two interpretations. *Agric Forest Meteorol 87*, 291–300.
Pedescoll, A., Sidrach-Cardona, R.J., Sanchez, C., and *Bécares, E.,* 2013: Evapotranspiration affecting redox conditions in horizontal constructed wetlands under Mediterranean climate: Influence of plant species. *Ecol Eng 58*, 335– 343.
Poiani, K.A. and *Johnson, W.C.*, 1993: A spatial simulation model of hydrology and vegetation dynamics in semipermanent prairie wetlands. *Ecol Appl* 3:279–293.
Russell, I.A. and *Kraaij, T.*, 2008: Effects of cutting *Phragmites australis* along an inundation gradient, with implications for managing reed encroachment in a South African estuarine lake system. *Wetland Ecol Man* 16:383–393.
Ryu, S.R., Chen, J., Noormets, A., Bresee, M.K., and *Ollinger, S.V.*, 2008: Comparisons between PnET-Day and eddy covariance based gross ecosystem production in two Northern Wisconsin forests. *Agric Forest Meteorol 148,* 247–256.
Savoy, P. and *Mackay, D.S.*, 2015: Modeling the seasonal dynamics of leaf area index based on environmental constraints to canopy development. *Agric Forest Meteorol 200*, 46–56.
Soetaert, K., Hoffman, M., Meire, P., Starink, M., van Oevelen, D., Van Regenmortel, S., and *Cox, T.,* 2004: Modeling growth and carbon allocation in two reed beds (*Phragmites australis*) in the Scheldt estuary. *Aquat Bot 79*, 211–234.

Sorrell, B.K., Mendelssohn, I.A., McKee, K.L., and *Woods, R.A.,* 2000: Ecophysiology of wetland plant roots: A modelling comparison of aeration in relation to species distribution. *Aquat Bot 86,* 675–685.

Sun, L. and *Song, C*., 2008: Evapotranspiration from freshwater marsh in the Sanjiang Plain, Northeast China. *J Hydrol 352*, 202–210.

Tátrai, I., Mátyás, K., Korponai, J., Paulovits, G., and *Pomogyi P.*, 2000: The role of the Kis-Balaton Water Protection System in the control of water quality of Lake Balaton. *Ecol Eng 16,* 73–78.

Windham, L., 1999: Microscale spatial distribution of *Phragmites australis* (common reed) invasion into *Spartina patens* (salt hay)-dominated communities in bractidal marsh. *Biol Invasions 1*, 137–148.

Zhong, Q., Gong, J., Wang, K., and *Zhang, C.,* 2014: Effects of 3-year air warming on growth of two perennial grasses (*Phragmites australis* and *Imperata cylindrica*) in a coastal salt marsh reclaimed for agriculture. *Aquat Bot 117*, 18–26.

Zhou, L., and *Zhou, G.*, 2009: Measurement and modelling of evapotranspiration over a reed (*Phragmites australis*) marsh in Northeast China. *J Hydrol 372*, 41–47.

IDŐJÁRÁS

Quarterly Journal of the Hungarian Meteorological Service
Vol. 121, No. 3, July – September, 2017, pp. 285–301

Analysis of the impacts of global warming on European bat species's range area in the 21st century using regional climate model simulation

Júlia Anna Nagy[1]*, **Judit Bartholy**[1], **Rita Pongrácz**[1], **Ildikó Pieczka**[1], **Hajnalka Breuer**[1], and **Levente Hufnagel**[2]

[1]*Department of Meteorology, Eötvös Loránd University, Pázmány Péter sétány 1/A, H-1117 Budapest, Hungary*

[2]*Crop Production Institute, Szent István University, Páter Károly u. 1, H-2100, Gödöllő, Hungary*

**Corresponding author E-mail: julcsi@nimbus.elte.hu*

(Manuscript received in final form October 12, 2016)

Abstract—Due to the projected climate change, the living territory of wild animals may be reshaped in the future, some of the species may even suffer extinction. The aim of this research is to make a comparative case study for the future predictions of the European terrestrial mammals' vulnerability to the climate change, by using their current range area maps (on the basis of The Atlas of the European Mammals). To characterize the climate indicators of the animals, we use the annual means and/or extremes of four climatic parameters (daily mean temperature, daily minimum temperature, daily maximum temperature, daily precipitation sum) based on the gridded E-OBS dataset for 1961–1990. Then, we determine specific percentiles of the climatic parameters for given species. The range area within the specific climatic intervals formed by the selected percentile pairs are mapped for the recent past (1961–1990), and also for the middle (2021–2050) and the end (2071–2100) of the 21st century using the RACMO (Regional Atmospheric Climate Model) simulation for the SRES A1B scenario. Our results suggest that, the optimal climatic requirements of the *Pipistrellus pipistrellus* may decrease and shift northward until the end of the 21st century. Moreover, this anaysis based on the climate indicator profile technique suggests a remarkable change in the habitats of all studied European bat species, and their northward migration in order to find their optimal conditions. As a result, from the recent past time period of 1961–1990, 63% of the studied European bat species will probably suffer habitat decrease, while 30% are likely to experience habitat increase, and 7% is projected to disappear by the end of the 21st century. Due to the projected regional climate change in Europe, habitat loss and degradation are the greatest threats to the studied bat species.

Key-words: mammals, bat species, temperature, precipitation, migration, ecology

1. Introduction

The results of the ENSEMBLES project predictions concerning Europe suggest that under the A1B medium-high emission scenario (*Nakicenovic* and *Swart*, 2000) without mitigation, yearly mean temperature may rise by 1–2 °C by 2021–2050, and 1,5–4 °C by 2071–2100 relative to the baseline period 1961–1990 (*van der Linden* and *Mitchell*, 2009). The greatest warming in both periods is likely to occur in northeastern and southern parts of the continent. The projections indicate large differences across Europe for yearly precipitation sum and both the overall intensity and frequency of extreme precipitation events. In the northern areas, an overall increase in precipitation is projected, whereas drying trend is likely to occur in southern Europe (*van der Linden* and *Mitchell*, 2009).

Changing climate affects not only humans and, therefore, the urban environment, but also the living conditions of wild animals. One of the most important impacts of climate change may be that animals tend to occupy geographical regions with climatic conditions, which become suitable to the specific requirements of the given species. Therefore, local extinctions may arise and populations may suffer fragmentation (e.g., *Thomas et al*., 2004; *Peterson* and *Williams*, 2004; *Pounds et al*., 2006). The extinction and their survival in unconnected populations may cause reduction of genetic variability and high levels of inbreeding (*Ezard* and *Travis*, 2006).

The relationship between global warming and the response of the wildlife is obviously strong (*Williams et al*., 2003). The analysis of geographical impacts of climate change to wildlife is an increasingly popular research topic (*Thomas et al.*, 2004; *Diós et al*., 2009; *Drégelyi-Kiss* and *Hufnagel*, 2009*; Chen et al*., 2011; *Bartholy et al.,* 2012), however, the projections of future conditions are rarely investigated due to the lack of suitable model simulation outputs and the complex interdisciplinary methodology.

Climate is one of the abiotic factors, which controls primarily the range areas of the wildlife. If the climate significantly changes in a particular region, it may disturb the ecosystem and increase the chance of extinction. According to *Williams et al*. (2007), under the SRES A2 scenario (*Nakicenovic* and *Swart*, 2000) assumptions, 12–39% of the Earth's terrestrial surface is likely to experience significantly different climate conditions from the current climate.

Due to the anthropogenic activity, Europe is one of the most highly fragmented continents of the globe. Consequently, only about 1% of the surface area of the continent can be considered as wilderness, with the old-growth forests of Scandinavia, Poland, and Russia (*Jaeger et al*., 2011). Landscape fragmentations caused by roads, highways, and other artificial surfaces, have a number of detrimental effects, i.e., reduction in size and persistence of wildlife populations, and can provide great barriers to migrating animals (*Hanski*, 2005). Species' adaptation to current habitat fragmentation, and additionally to projected future climate change is an essential ecological problem. The key to this issue is

providing increased connectivity, which could be the most significant aspect of mammal conservation in Europe (*Temple* and *Terry*, 2007).

Increasing temperature is estimated to cause significant loss of appropriate environment of all regionally endemic animals. On a European scale, roughly 25% of the wild terrestrial mammals are endemic to the continent (*Chen et al.,* 2011). The species that are affected the most negatively by climate change are the habitat specialists, and the species being less mobile. Species that live in fragmented landscapes may also struggle with the negative impacts of climate change, because they are not able to colonize the area (*Chen et al*., 2011).

According to *Temple* and *Terry* (2007), 15% of all wild European terrestrial and marine species are threatened, and 9% are listed near threatened, furthermore, 1.3% are already regionally or globally extinct. Nowadays, the rate of species extinctions worldwide is 100 to 1,000 times greater compared to the natural rate and is rapidly accelerating (*May et al.*, 1995). To moderate and delay the negative impacts of climate change on species' loss is both urgent and probably the most important issue for ecological researchers (*Bátori et al*., 2014).

In the regional ecosystems, bats are highly vulnerable to changing climate (*Burns et al*., 2003; Rebelo et al., 2010), that is why they can be considered as important indicator species, which may facilitate in identifying areas where conservation efforts should focus on. For instance, a few recent studies (e.g., *Rebelo et al*., 2010, *Prydatko et al*., 2011; *Sherwin et al*., 2013) demonstrate how the predicted climate change will affect the distribution of different bat species. According to *Petersen et al*. (2014), in the past three decades, there has been a significant increase in bat records in Iceland and the Faroes, which could probably be linked to climate change. It has also been reported that the analyzed time period of 2001–2010 was the warmest in the Faroes since 1890 (*Cappelen,* 2011). Additionally, climate change may result in many other impacts on bat species around the world. For example, a recent study by *Luo et al*. (2014) shows that global warming is likely to alter the prey detection ability of echolocating bats. This may affect the bat species' community structure and their distribution, as well as those of their insect prey.

The above mentioned studies all highlight the importance of this global issue and the need for further research to understand the mechanisms of climate stress to ecosystems. Such detailed analysis may help to minimize the negative impacts of global warming to the wildife and ecosystems before it would be irreversible.

The aim of our research is to make a comparative study for the future predictions of the European terrestrial mammals' vulnerability to the climate change. In the current study, fine (25 km) resolution, bias-corrected outputs of the RACMO (Regional Atmospheric Climate Model) simulation taking into account the SRES A1B intermediate emission scenario are analyzed for the entire 21st century. First, the data describing climatic conditions are identified for each mammal species. Then, the values of the four climate variables are presented on maps for the past (1961–1990), the middle (2021–2050), and the end (2071–2100)

of the 21st century. Finally, changes in the future potential spatial status and size of given species' habitat are calculated.

2. Materials and methods

2.1. Data used in the analysis

Our analyses are based on the following databases: (1) The Atlas of European Mammals (available from Societas Europaea Mammalogica) is used for defining the range area of species. This database was compiled in 1999 (*Mitchell-Jones et al.*, 1999) and has been widely used as reference dataset. It separately contains data for the pre-1970 and post-1970 presence of mammal species in Europe. (2) To characterize the climate indicators of the animals, we use the 30 years means of four climatic variables (daily mean temperature, daily minimum temperature, daily maximum temperature, daily precipitation sum) based on the gridded E-OBS dataset (*Haylock et al*., 2008) using 25 km horizontal resolution. This database was compiled from quality controlled daily data of national meteorological station networks. (3) For the future, predictions of the temperature and precipitation for time periods 2021–2050 and 2071–2100 considering SRES A1B (Nakicenovic and Swart, 2000) scenario, we use the bias-corrected outputs of RACMO simulation (*van Meijgaard et al*., 2008), which was completed by KNMI (Royal Netherlands Meteorological Institute) in the framework of the ENSEMBLES project (*van der Linden* and *Mitchell*, 2009). Bias correction of daily data was completed on the basis of monthly quantile matching technique (*Pongrácz et al*., 2014) for the time period of 1961–2100.

2.2. Species' climate indicator profile

According to *Vaughan et al.* (2000) estimations, every endotherm has a thermal neutral zone (TNZ), which covers the temperature tolerance range. Within the species' TNZ the organisms do not need to produce extra energy to keep itself warm, neither cooling themselves. Therefore, minimum, maximum, and mean temperatures were used as species' climate indicator variables. In addition, precipitation sum also influences the wild mammals by controlling their resource availability (*Hooper et al*., 2005), that is why precipitation is also considered as climate indicator variable.

Each European bat species was characterized by specific percentile pairs related to the four climate describing variables (mean temperature, precipitation sum, minimum temperature, maximum temperature) and the climatic values that mostly cover the current spread of the species in Europe. The specific percentiles were determined on the basis of the E-OBS datasets representing the observations (*Haylock et al.,* 2008), and using combined analysis of digitalized distribution maps by The Atlas of European Mammals (*Mitchell-Jones et al*., 1999). We have

evaluated the bat species in Europe by their climatic requirements. During this process, on the basis of all the values of the climatic variables where the Atlas shows the presence of the species, the empirical distribution is determined. From this distribution, a „lower" and an „upper" percentile can be selected using the step value of 0.01 in the empirical cumulative relative frequency; i.e., the minimum value is paired to the 1st, 2nd, ..., 100th percentiles; the 1st percentile is paired to the 2nd, 3rd, ..., 100th percentiles; ..., the 99th percentile is paired to the 100th percentile. Thus, altogether 5050 (101·100/2) possible pairs are evaluated for each climatic variable. For this purpose, specific percentile pairs were determined from the following gridcell-based values of the climatic variables:

- annual mean values of the daily mean temperature data averaged for 30 years;
- annual maximum values of the daily maximum temperature data averaged for 30 years;
- annual minimum values of the daily minimum temperature data averaged for 30 years;
- annual sum values of the daily precipitation data averaged for 30 years.

Two percentiles were selected to form an interval, which were used to calculate the number of gridcells according to the following criteria:

- *A* indicates the number of gridcells where particular species could live under temperature and precipitation conditions, and it actually lives (located in the area between the two percentile values, and it actually is included in the Atlas).
- *B* indicates the number of gridcells where particular species could live under the temperature and precipitation conditions, but does not live (located in the area between the two percentile values, but there is no recorded presence according to the Atlas).
- *C* indicates the number of gridcells, where particular species could not live under the actual temperature and precipitation conditions, but it actually lives (the climatic value is not between the two percentiles, but there is a recorded presence in the Atlas).

These criteria were analyzed for all possible pairwise selection of the "lower" and "upper" percentiles (5050 percentile pairs), then, the value of *Q* was calculated using the following formula:

$$Q = A / (A + B + C) \quad (1)$$

The final "lower" and "upper" percentiles were determined for each climatic variable (mean temperature, precipitation sum, minimum temperature, maximum temperature), where the procedure leads to the regional maximum value of Q. The interval between these "lower" and "upper" percentiles describes the climatic requirements of a given species.

We prepared the index graphs for all the mammal species including the bat species analyzed in this paper. The values of the four climatic variables (mean temperature, precipitation sum, minimum temperature, maximum temperature) were mapped for the recent past (1961–1990) and for two future time periods (2021–2050, 2071–2100) based on the simulation outputs. Moreover, the projected changes of the size and spatial status of the area (range) were also mapped for the mid- and late-century.

2.3. Spatial scale of the analysis

The applied study area was limited by the simulation domain of RACMO, which extends from 34°N to 74°N latitude, and from 11°W to 41°E longitude, this includes western Europe, with the eastern borders of Finland, the Baltic states, Poland, Slovakia, Hungary, Romania, Bulgaria, and European Turkey (Thrace) forming the eastern border. Moreover, from the Atlantic, the Faroe Islands were included, as were the Portuguese and Spanish islands of Macaronesia. In the south, Malta was included. The range area maps were scaled to a fine (25 km) horizontal resolution of the E-OBS climate data and the RACMO simulated data.

3. Results

This analysis based on the climate indicator profile technique enables us to estimate the possible regional impacts of the projected climate change to the living territory and conditions of the European bat species. These species have been selected, because recent studies suggest that bat species are affected negatively by climate change (*Burns et al*., 2003; *Rebelo et al*., 2010), and their responses have been rarely studied.

Among the results, a methodological case study based on the simultaneous analysis of the current range map from The Atlas of European Mammals and the E-OBS observations database for 1961–1990 is analyzed here, through the example of the common pipistrelle (*Pipistrellus pipistrellus, Temminck, 1840*). The climate indicator maps for the mid-century (2021–2050) and the end of the 21st century (2071–2100) characterize the sensitivity of the estimated changes in the habitat of species *Pipistrellus pipistrellus*, due to the projected regional climate change in Europe. Then, using the current range maps from the Atlas of European Mammals, changes in the future potential spatial status and size of 30 European bat species' habitat were calculated. Moreover, we have determined the most endangered wild European mammals for the entire 21st century, to be focused for future action plans and protect these species. Such detailed analysis may help to minimize these negative impacts of global warming.

Based on the current range map of the common pipistrelle, this species is present in 4,216 grid cells in Europe (*Fig. 1*). Its conservation status is 'least concern' (*Temple* and *Terry*, 2007), nevertheless, it is protected in Hungary. The

species is listed in Appendix III of the Bern Convention – i.e., Convention on the Conservation of European Wildlife and Natural Habitats, 1979 –, and Appendix II of the Bonn Convention – i.e., Convention on the Conservation of Migratory Species of Wild Animals, 1979 (*Battersby,* 2005).

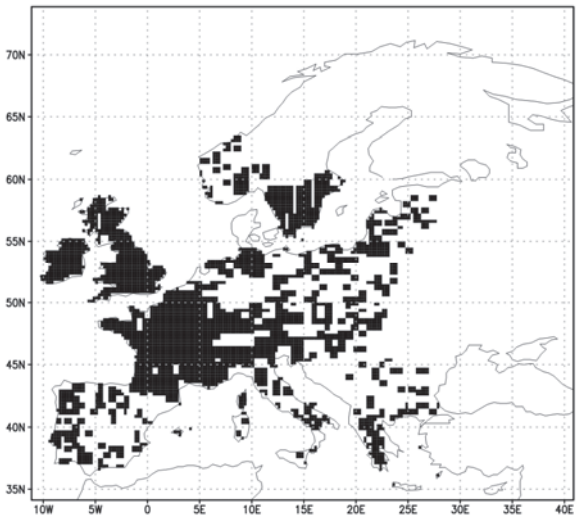

Fig. 1. The range map of *Pipistrellus pipistrellus* on the base of the Atlas of European Mammals. Shaded area indicates the occurrence of the species.

Fig. 2 represents how the procedure leads to the regional maximum value of the *Q*, based on the systematic estimation process using the percentile pairs. The four climate indicator variables together describe the optimal climatic requirements of the *Pipistrellus pipistrellus* species. It can be seen from *Fig. 2a* that the maximum *Q* value in case of the mean temperature climate variable is 28.5% (which is reached in case of using the 48th and 86th percentiles). The maximum *Q* value in case of the precipitation sum presented in *Fig. 2b* is 38.3% (when using the 82nd and 100th percentiles). *Fig. 2c* shows the maximum *Q* value in case of the minimum temperature, which is 33.9% (when using the 61st and 86th percentiles). Finally, the maximum *Q* value in case of the maximum temperature is 15.9% (when using the 1st and 77th percentiles) as shown in *Fig. 2d*.

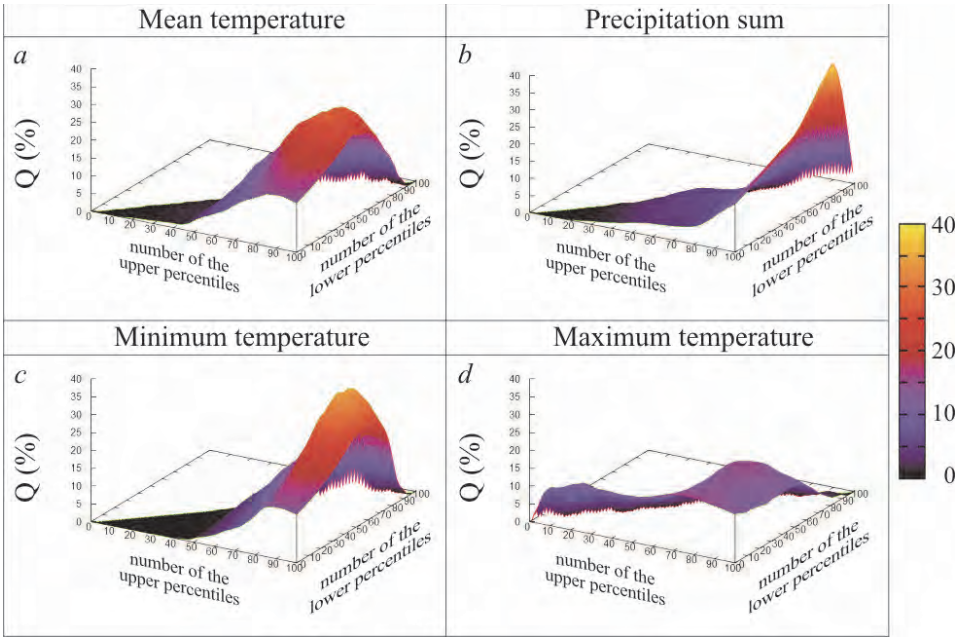

Fig. 2. Graphs of *Pipistrellus pipistrellus'* climate indicators, based on the observed annual mean values of the four climate describing variables. The graphs refer to the upper and lower percentiles on the horizontal axes. The values of *Q* (expressed in %) are shown on the vertical axis.

The maps based on the observed values of mean temperature (*Fig. 3a*), minimum temperature (*Fig. 3c*), maximum temperature (*Fig. 3d*), and precipitation sum (*Fig. 3b*) together explain the current boundaries of the European *Pipistrellus pipistrellus*. Colored areas show the following intervals of the variables' values on the maps:

- a) for mean temperature: 5.7 °C – 13.5 °C (48th–86th percentiles),
- b) for precipitation sum: 626 mm – 3347 mm (82nd–100th percentiles),
- c) for minimum temperature: –17.5 °C – –4.9 °C (61st–86th percentiles),
- d) for maximum temperature: 18.5 °C – 35.0 °C (1st–77th percentiles).

The map based on the observed values of the maximum temperature shows (*Fig. 3d*) the almost full optimal coverage in Europe for this species, because of the wide interval of the values. Thus, analyzing the maps of all the four variables provides an estimate of the animal's current spread within Europe.

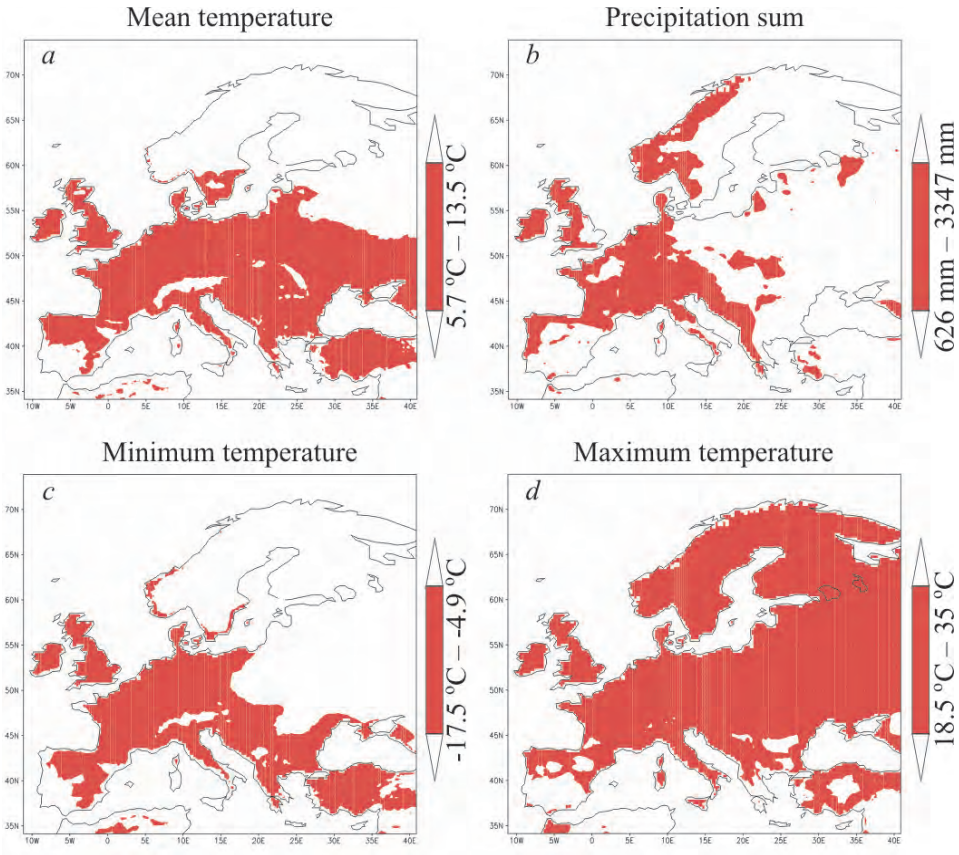

Fig. 3. Individual maps of the climate indicators for *Pipistrellus pipistrellus*, based on the observed annual values of the four climatic variables.

The model simulations for the periods 2021–2050 and 2071–2100 show a northward shift of the optimal climatic conditions of the *Pipistresllus pipistrellus* species, which is very likely due to global warming (*Fig. 4*).

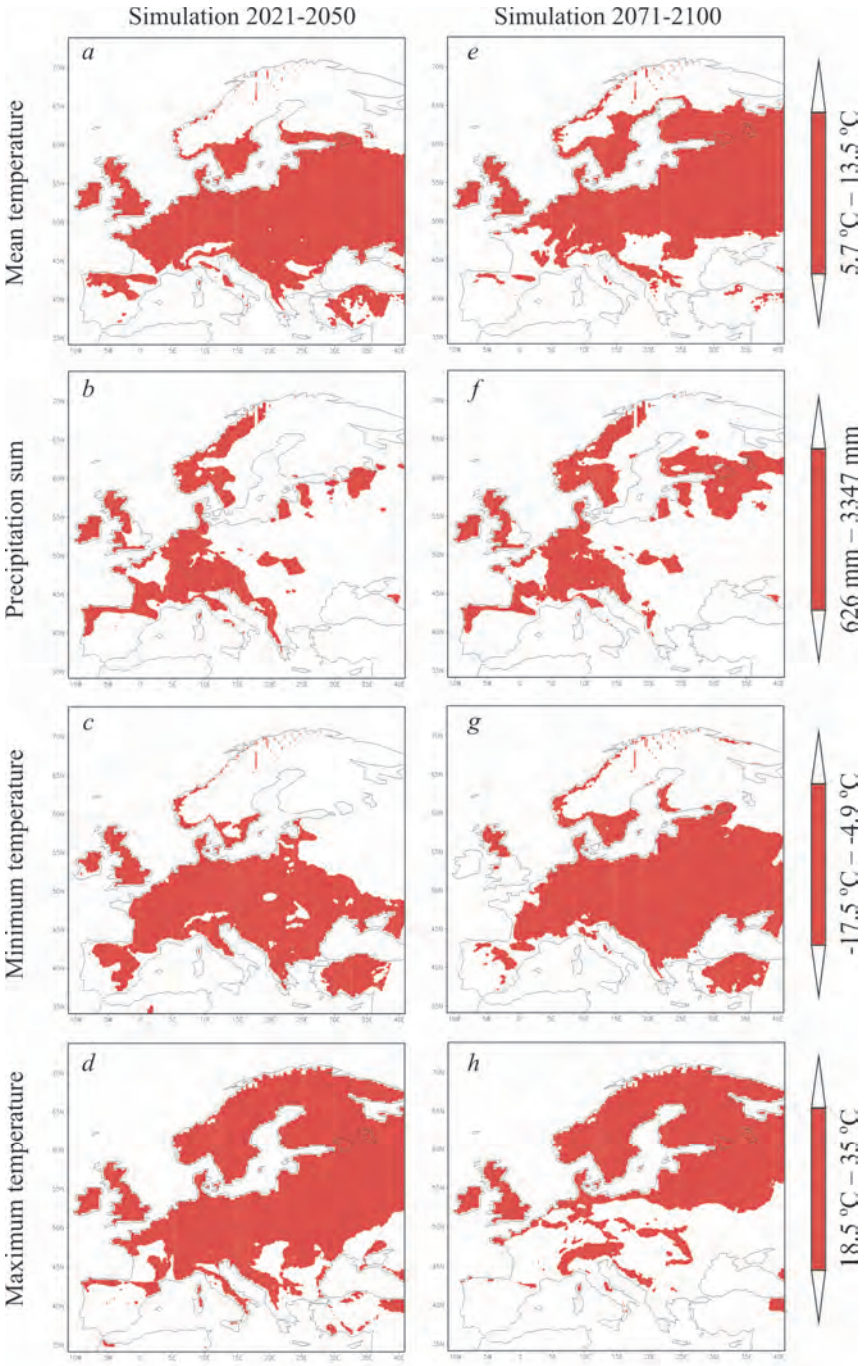

Fig. 4. Individual maps of the climate indicators for *Pipistrellus pipistrellus*, based on the annual values of the four climatic variables for the simulated periods of 2021–2050 (a-d) and 2071–2100 (e-h).

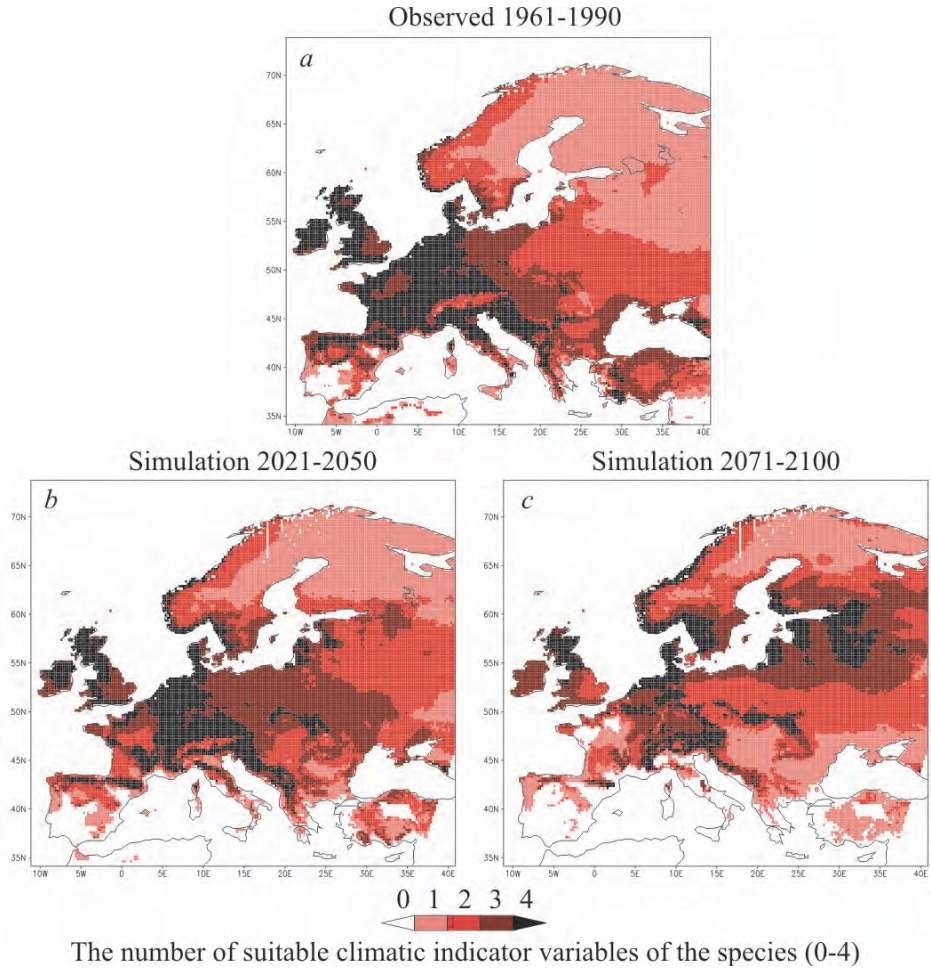

Fig. 5. Composite maps of *Pipistrellus pipistrellus'* climate indicators, based on the annual values of the four climatic variables for the observation period of 1961–1990 (a), and for simulated periods of 2021–2050 (b) and 2071–2100 (c).

Several shades are used on the composite maps (*Fig. 5*) of the *Pipistrellus pipistrellus* species' climate indicator areas, corresponding to how many variables are within the optimal ranges in the given grid cells (0–4). The darkest shade indicates the composite area, where each analyzed variables can be found within the optimal range of the *Pipistrellus pipistrellus* in the given grid cell. Our estimation, based on the composite maps of the *Pipistrellus pipistrellus* species illustrates a fitting similarity of 81% between the current range area and the composite climate indicator variables.

The composite maps present a major northward shift and an overall decline of the composite climate indicator area of the *Pipistrellus pipistrellus* species (*Fig. 5d*). As can be seen in *Table 1*, the composite climate indicator range will probably decrease from 1,498,350 km^2 to 948,761 km^2 until the end of the 21st century, which means 37% area decline, compared to the observed time period of 1961–1990.

Table 1. Comparison of the size of the composite range area of *Pipistrellus pipistrellus*, based on the climate indicator values in different time slices

Climatic indicator variable	Observed 1961–1990 (km^2)	Simulation 2021–2050 (km^2)	Simulation 2071–2100 (km^2)
Mean temperature	4,667,650	4,891,376	4,275,980
Minimum temperature	3,414,878	4,112,801	4,625,866
Maximum temperature	6,844,172	5,495,416	3,493,743
Precipitation sum	2,409,654	2,040,029	2,428,300
Composite area	1,498,350	1,154,040	948,767

All the studied bat species have 8,551 grid cells together (shaded area in *Fig. 6*), summarized from their current range maps. The greatest bat biodiversity is located in western Europe and in the mountainous regions of Mediterranean and temperate Europe (*Fig. 6*).

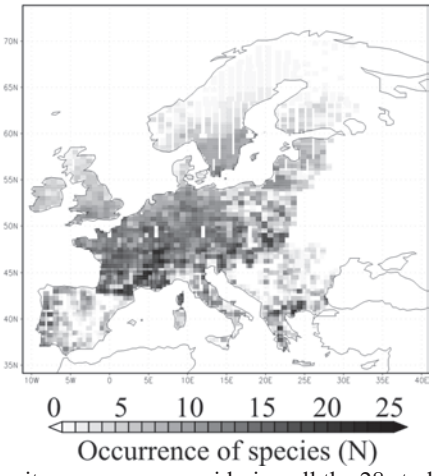

Fig. 6. The current composite range map considering all the 28 studied bat species, based on the Atlas of European Mammals.

The composite maps for the projected time periods 2021–2050 and 2071–2100 indicate remarkable change in the spatial status and size of the studied European bat species climate indicators. The composite range area will probably shift to the Baltic region and to the mountainous regions of eastern Europe and western Russia, considerably by the end of the 21st century (*Fig. 7c*).

Our estimations suggest that, compared to the recent past time period of 1961–1990, 93% (N=26, where N is the number of the bat spices) of the studied European bat species will suffer habitat decrease (*Table 2*), while 7% (N=2) are likely to experience habitat increase till the mid-century (2021–2050). Furthermore, compared to the recent past time period of 1961–1990, 96% (N=27) of the studied European bat species are projected to suffer habitat decrease, while 4% (N=1) may disapear till the end of the 21st century (2071–2100).

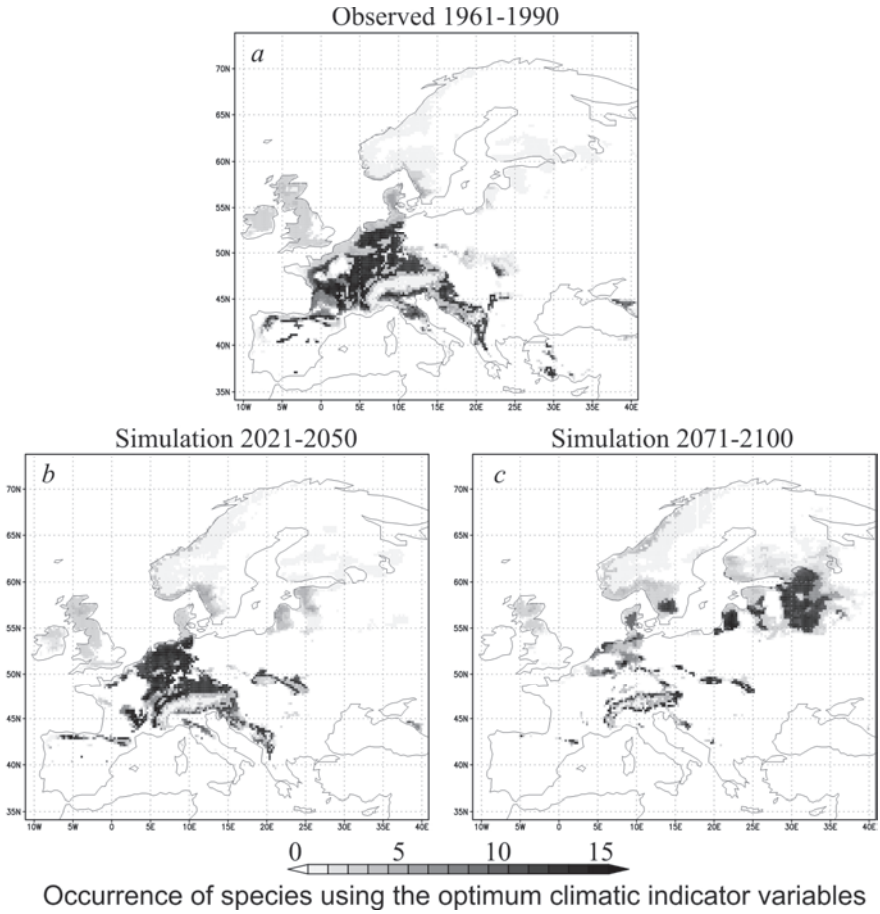

Fig. 7. Size of the composite range area of all studied European bat species, based on the climate indicator values for the past and future time slices.

We have determined the most endangered European bat species by the middle and also by the end of the 21st century to be focused for future action plans and protecting these species. The results suggest that, from the studied 30 bat species, *Rhinolophus mehelyi*'s optimal climatic conditions are projected to disappear by 2071–2100. This species is narrowly distributed on the continent nowadays, and is also present in relatively few grid cells. Consequently, it might have narrower climatic niche.

Table 2. English and Latin name of all studied bat species and the projected habitat change by the middle and the end of the 21st century (relative to the 1961–1990 reference period)

English name	**Latin name**	**by 2021–2050**	**by 2071–2100**
Barbastelle	*Barbastella barbastellus*	decrease	decrease
Northern bat	*Eptesicus nilssonii*	decrease	decrease
Serotine	*Eptesicus serotinus*	decrease	decrease
Schreibers' bat	*Miniopterus schreibersii*	decrease	decrease
Bechstein's bat	*Myotis bechsteinii*	decrease	decrease
Lesser mouse-eared bat	*Myotis blythii*	decrease	decrease
Brandt's bat	*Myotis brandti*	increase	decrease
Long-fingered bat	*Myotis capaccinii*	decrease	decrease
Pond bat	*Myotis dasycneme*	decrease	decrease
Daubenton's bat	*Myotis daubentonii*	decrease	decrease
Geoffroy's bat	*Myotis emarginatus*	increase	decrease
Greater mouse-eared bat	*Myotis myotis*	decrease	decrease
Whiskered bat	*Myotis mystacinus*	decrease	decrease
Natterer's bat	*Myotis nattereri*	decrease	decrease
Leisler's bat	*Nyctalus leisleri*	decrease	decrease
Noctule	*Nyctalus noctula*	decrease	decrease
Kuhl's pipistrelle	*Pipistrellus kuhlii*	decrease	decrease
Nathusius' pipistrelle	*Pipistrellus nathusii*	decrease	decrease
Common pipistrelle	*Pipistrellus pipistrellus*	decrease	decrease
Savi's pipistrelle	*Pipistrellus savii*	decrease	decrease
Brown long-eared bat	*Plecotus auritus*	decrease	decrease
Grey long-eared bat	*Plecotus austriacus*	decrease	decrease
Mediterranean horseshoe bat	*Rhinolophus euryale*	decrease	decrease
Greater horseshoe bat	*Rhinolophus ferrumequinum*	decrease	decrease
Lesser horseshoe bat	*Rhinolophus hipposideros*	decrease	decrease
Mehely's horseshoe bat	*Rhinolophus mehelyi*	decrease	disapear
European free-tailed bat	*Tadarida teniotis*	decrease	decrease
Parti-coloured bat	*Vespertilio murinus*	decrease	decrease

4. Discussion and conclusions

The purpose of this reasearch was to analyze the possible regional impacts of the global warming to the living territory and conditions of the European bat species. Our predictions, based on the climate indicator profile technique of the 30 studied European bat species are consistent with the analysis of *Rebelo et al*. (2010) about these species' rapid potential northward migration due to the projected regional climate change during the 21st century. Furthermore, these species may suffer decrease in their size of habitats and disappearance from their current range areas. Estimations of *Rebelo et al.* (2010) were based on SRES A1FI, A2, B1, and B2 scenarios (*Nakicenovic* and *Swart*, 2000), our results conclude similar projections even though they consider a different (A1B) scenario. Consequently, all future scenarios predict reduction in European bat species richness in Europe, compared to the current conditions. The northward shift of the daily mean, minimum, and maximum temperature could imply a significant change in habitats. Meanwhile, the projected precipitation change is not likely to affect the possible migration of bat species in Europe. Other studies mention signs about European bats having already suffered from the impacts of regional climate change. For instance, due to response to warmer temperature conditions in the past 15 years, the species *Pipistrellus kuhlii*'s range area has expanded northwards (*Sachanowicz et al*., 2006), whereas in southern regions of Spain, the parturition in *Myotis myotis* has occurred up to 6 months before the expected birth period (*Ibanez*, 1997). As an overall result, habitat conditions are likely to decrease in continental climate regions during the 21st century. Due to the projected regional climate change in Europe, habitat loss and degradation is the greatest threat to the studied bat species.

Acknowledgements: Research leading to this paper has been supported by the following sources: the AGRÁRKLIMA2 project (VKSZ_12-1-2013-0034) and the Research Centre of Excellence-8526-5/2014/TUDPOL. The ENSEMBLES data used in this work was funded by the EU FP6 Integrated Project ENSEMBLES (Contract number 505539) whose support is gratefully acknowledged. Furthermore, we acknowledge the E-OBS dataset from the EU-FP6 project ENSEMBLES (http://ensembles-eu.metoffice.com), and the data providers in the ECA&D project (http://eca.knmi.nl).

References

Bartholy J., Pongracz R., Nagy J., Pieczka I., and *Hufnagel L*., 2012: Regional climate change impacts on wild animals' living territory in central Europe. *Appl. Ecol. Environ. Res. 10*, 107–120.

Bátori, Z., Lengyel, A., Maróti, M., Körmöczi, L., Tölgyesi, C., Biró, A., Tóth, M., Kincses, Z., and *Erdős, L.,* 2014: Microclimate-vegetation relationships in natural habitat islands: species preservation and conservation perspectives, *Időjárás 118*, 257–281.

Battersby, J. 2005: UK Mammals: Species Status and Population Trends. First Report by the Tracking Mammals Partnership. JNCC / The Tracking Mammals Partnership.

Burns C.E., Johnston K.M., and *Schmitz O.J.,* 2003: Global climate change and mammalian species diversity in U.S. national parks. *Proc. Nat. Acad. Sci. 100*, 11474–11477.

Chen, I.C., Hill, J.K., Ohlermüller, R., Roy, D.B., and *Thomas, C.D.,* 2011: Rapid range shifts of species associated with high levels of climate warming. *Science 333*, 1024–1026.

Cappelen, J., 2011: Denmark's climate 2010 in Torshavn, Faroe islands and Nuuk, Greenland. Technical report 11–01. Danmarks Meteorologiske Institut, Kobenhavn. Available at www.dmi.dk/dmi/tr11-01. 72p. (in Danish, with English summary).

Diós, N., Szenteleki, K., Ferenczy, A., Petrányi, G., and *Hufnagel, L*. 2009: A climate profile indicator based comparative analysis of climate change scenarios with regard to maize (zea mays l.) Cultures. *Appl. Ecol. Environ. Res. 7*, 199–214.

Drégelyi-Kiss, Á., and *Hufnagel, L*., 2009: Simulations of Theoretical Ecosystem Growth Model (TEGM) during various climate conditions. *Appl. Ecol. Environ.Res. 7,* 71–78.

Ezard T.H.G., and *Travis J.M.J.,* 2006: The impact of habitat loss and fragmentation on genetic drift and fixation time. *Oikos 114*, 367–375.

Haylock, M.R., Hofstra, N., Klein Tank, A.M.G., Klok, E.J., Jones, P.D., and *New, M.,* 2008: A European daily high-resolution gridded dataset of surface temperature and precipitation. *J. Geophys. Res. (Atmospheres) 113*, D20119.

Hanski, I., 2005: Landscape fragmentation, biodiversity loss and the societal response. *EMBO reports* 6, 388–392.

Hooper, D.U., Chapin, F.S., Ewel, J.J., Hector, A., Inchausti, P., Lavorel, S., Lawton, J.H., Lodge, D.M., Loreau, M., Naeem, S., Schmid, B., Setälä, H., Symstad, A.J., Vandermeer, J., and *Wardle, D.A.,* 2005: Effects of biodiversity on ecosystem functioning: A consensus of current knowledge. *Ecol.Monogr. 75*, 3–35.

Ibanez, C. 1997: Winter reproduction in the greater mouse-eared bat (Myotis myotis) in South Iberia. J. *Zoology 243*, 836–840.

Jaeger, J.A.G., Soukup, T., Madriñán, L.F., Schwick, C., and *Kienast, F.*, 2011: Landscape fragmentation in Europe. *EEA Report* No 2/2011.

van der Linden, P. and *Mitchell, J.F.B*., (Eds.), 2009: ENSEMBLES: Climate Change and its Impacts: Summary of research and results from the ENSEMBLES project. Met Office Hadley Centre, UK.

Luo J., Koselj K., Zsebők, S., Siemers B., and *Goerlitz, H.R.,* 2014: Global warming alters sound transmission: differential impact on the prey detection ability of echolocating bats. *J. R. Soc. Interface 11*, 20130961.

May, R.M., Lawton, J.H., and *Stork, N.E.,* 1995: Assessing extinction rates. In: (Eds. *Lawton, J.H., May R.M.*) Extinction rates. Oxford University Press, New York, NY, USA. 1–24.

van Meijgaard, E., van Ulft, L.H., van de Berg, W.J., Bosveld, F.C., van den Hurk, B.J.J.M., Lenderink, G., and *Siebesma, A.P.,* 2008: The KNMI regional atmospheric climate model RACMO version 2.1, Technical Report.

Mitchell-Jones, A.J., Amori, G., Bogdanowicz, W., Krystufek, B., Reijnders, P.J.H., Spitzenberger, F., Stubbe, M., Thissen, J.B.M., Vohlarik, V., and *Zima, J.,* 1999: The Atlas of European Mammals. T A & D Poyser.

Nakicenovic, N. and *Swart, R.,* (Eds), 2000: Emissions Scenarios. A special reports of IPCC Working Group III. Cambridge University Press, UK., 570p.

Petersen, A., Jens-Kjeld, J., Paulina, J., Bloch D., and *Finnur, I.,* 2014: A review of the occurrence of bats (Chiroptera) on islands in the North East Atlantic and on North Sea installations. *Acta Chiropterologica 16*, 169–195.

Peterson O., Phillips L. and *Williams S.E*., 2004: Extinction risk from climate change. *Nature 427*, 145–148.

Pongrácz R, Bartholy J, and *Kis A.,* 2014: Estimation of future precipitation conditions for Hungary with special focus on dry periods. *Időjárás 118*, 305–321.

Pounds, J.A., Bustamante, M.R., Coloma, L.A., Consuegra, J.A., Fogden, M.P.L., Foster, P.N., La Marca, E., Masters, K.L., Merino-Viteri, A., Puschendorf, R., Ron, S.R., Sanchez-Azofeifa, G.A., Still, C.J., and *Young, B.E.,* 2006: Widespread amphibian extinctions from epidemic disease driven by global warming. *Nature 439*, 161–167.

Prydatko, V., Makarenko, V., and *Kolomytsev, G.,* 2011: Lesser Noctule (Nyctalus leisleri) habitats change modelling in EEBIO Region in scope of the IMAGE climate change data: GLM scenario by 2050. Biomodel. Vefsíða. Available at: http://bio model.info/species/lesser-noctule-nyctalus-leisleri/.

Rebelo, H.,Tarroso, P., and *Jones, G.,* 2010: Predicted impact of climate change on European bats in relation to their biogeographic patterns. *Glob. Change Biol. 16*, 561–576.
Sachanowicz, K., Wower, A., and *Bashta A-T.,* 2006: Further range extension of Pipistrellus kuhlii (Kuhl, 1817) in central and eastern Europe. *Acta Chiropterologica 8*, 543–548.
Sherwin, H. A., Montgomery, W. I., and *Lundy, M.G.,* (2013): The impact and implications of climate change for bats. *Mammal Rev. 43*, 171–182.
Temple, H.J. and *Terry, A.* (Compilers), 2007: The Status and Distribution of European Mammals. Office for Official Publications of the European Communities, Luxembourg.
Thomas C.D., Cameron A., Green R.E., Bakkenes M., Beaumont L.J., Collingham Y.C., Erasmus B.F.N., Ferreira de Siquera M., Grainger A., Hannah L., Hughes L., Huntley B., van Jaarsveld A. S., Midgley G.F., Miles L., Ortega-Huerta M.A., Townsend ,A., Peterson O., Phillips L. and *Williams S.E*., 2004: Extinction risk from climate change. *Nature 427*, 145–148.
Vaughan, T.A., Ryan, J.M., and *Czaplewski N.J*., 2000: Mammalogy. 4th ed. Saunders College Publishing, Fort Worth, Texas
Williams, J.W., Jackson, S.T., and *Kutzbach, J.E.,* 2007: Projected distributions of novel and disapearing climates by 2100 AD. *Proc. Nat. Acad. Sci. 104*, 5738–5742.
Williams, S.E., Bolitho, E.E., and *Fox, S.,* 2003: Climate change in Australian tropical rainforests: An impending environmental catastrophe. *Proc. Biol. Sci. 270*, 1887–1892.

IDŐJÁRÁS

Quarterly Journal of the Hungarian Meteorological Service
Vol. 121, No. 3, July – September 2017, pp. 303–328

Meteorological conditions associated with West Nile fever incidences in Mediterranean and continental climates in Europe

Attila J. Trájer*

University of Pannonia, Department of Limnology
Egyetem utca 10, H-8200 Veszprém, Hungary

**Corresponding author E-mail: attilatrajer@gmail.com*

Abstract—West Nile fever (WNF) is the most important mosquito-borne disease in several countries of Europe. The annual phenology of the infection is mainly influenced by the seasonal activity of mosquitoes and humans. Culicid mosquitoes, the main vectors of West Nile virus prefer humid and warm conditions. This study was aimed at analyzing the West Nile fever season in Greece, Hungary, Israel and the Palestinian territories, Italy, Romania, and Serbia comparing the effect of ambient temperatures and precipitation sums on the case number of the disease. The countries were divided into two main groups – Mediterranean and continental – based on their climate. Epidemiological data of the European Centre for Disease Prevention and Control and climatic data of the European Climate Assessment and Dataset were used in the analysis. In each of the studied countries, positive correlations ($0.202 < r^2 < 0.746$; average: 0.531, SD: 0.23) were found between the monthly mean temperature and WNF case numbers. In contrast, in each of the studied countries negative correlations ($-0.131 < r^2 < -0.717$; average: –0.360; SD: 0.25) were found between the monthly precipitation sums and WNF case numbers. The mean monthly temperature in months when WNF cases were observed ranged between 15.8–28.1 °C (SD: 4.73). The case number weighted mean of the monthly temperature during the WNF-affected months varied between 17.4 to 28.8 °C (SD: 4.40). West Nile fever seasons started in June or July at 18.9–24.0 °C mean monthly temperatures (average: 21.6 °C, SD: 1.65). The WNF season ended in October or November at 18.7–5.3 °C mean monthly temperature regimes (average: 10.1 °C, SD: 5.43). The maximum lengths of the seasons were 3 to 5 months. WNF cases mainly occur in the warm or hot summer continental, the hot and dry summer Mediterranean, and the subtropical areas of Europe. The found different strength of impacts of the precipitation sums on the WNF case numbers in the Mediterranean and temperate climate countries in summer can be explained by the fact that while in humid temperate regions mosquitoes can find their breeding habitats without extreme rainfall events, in the Mediterranean countries, heavy rainfalls create suitable breeding habitat waters for mosquitoes.

Key-words: West Nile fever, temperature, precipitation, Köppen-Geiger climate classification

1. Introduction

West Nile fever (WNF) is an important mosquito-borne infection in the temperate regions of the Northern Hemisphere. The first WNF cases were detected in Europe (Albania) in 1958. Notable outbreaks were recorded already in the 1960s, the 70s and the 90s on the Old Continent (*Bardos*, 1959). Now, WNF is prevalent in the entire Mediterranean region and the continental parts of East Europe (*Hubálek* and *Halouzka*, 1996), but it is also an emerging disease in North America and North Africa. West Nile virus (WNV), the etiologic agent of WNF (*Goldblum et al.*, 1954) was first isolated in Uganda, in 1937 (*Barzon et al.*, 2015; *Kuno et al.*, 1998). The virus is the member of Flaviviridae, belonging to the Japanese encephalitis antigenic group of Flavivirus. Based on the glycoprotein envelope of the virus, two major human pathogenic lineages were distinguished: Lineage-1 and Lineage-2 strains (*Kemenesi et al.*, 2014; *Pachler et al.*, 2014; *Bakonyi et al.*, 2006). In 20–30% of the cases, WNV causes flu-like symptoms after a 2 to 14-day latency period, although about 70–80% of the cases is asymptomatic, and neurological symptoms appear in less than 1% of the cases. Individuals above the age of 65 have higher risk for morbidity and neurological manifestations (*Barzon et al.*, 2015; *Hayes et al.*, 2005). The most serious manifestation of the diseases is the rare lethal encephalomyelitis in humans. The case fatality rate is about 10% in the neurological infections (*CDC, West Nile virus, Symptoms & Treatment*). The virus is transmitted by mosquitoes from avian hosts in most of cases.

The predominant vectors of WNV are different culicid mosquitoes (*Koopmans et al.*, 2007). Occasionally, WNF can be transmitted by milk to breastfeeding babies or by organ transplantation (*Sambri et al.*, 2013; *Sampathkumar*, 2003). Imported human cases are also known from the literature (*Ivanov et al*., 1986; *Draganescu et al.,* 1977). The most characteristic, predominant mosquito vectors of WNV are the different *Culex* species (*Hannoun et al.*, 1964; *Hubálek et al*., 1999; *Kilpatrick et al*., 2006; *Kostyukov et al.*, 1986; *Szentpáli-Gavallér*, 2014; *Tsai et al.*, 1998; *Work et al.*, 1955). Argasid and ixodid ticks are vectors of WNV in Moldavia and Southern Russia (*Lawrie et al.*, 2004; *L'vov et al.,* 2002). Several of the vertebrae hosts of WNV are migratory birds (*Erdélyi et al.*, 2006, 2007), but the virus was also isolated in mammals (*Molnár et al.*, 1975). Antibodies were detected from humans, wetland birds (including wetland passerines), and other wild birds (e.g., migratory birds), chickens, domestic mammals as, e.g., cattle and other domestic ruminants, dogs, horses, game animals, and wild rodents. The normal cycle of the virus requires the presence of a vertebrae host, which is mainly a bird and an ornithophilic mosquito (or sometimes a hard tick) vector. It was found that two basic, bird-to-mosquito (*Hubálek* and *Halouzka*, 1999) and an alternative, bird-to-tick transmission cycles exist in East Europe (*Butenko et al.*, 1968; *Chumakov et al.*, 1968).

Climatic factors have a major effect on the range and seasonal activity of many arthropod vectors as ticks, sandfly species, and vector mosquitoes

determining the seasonality and incidence of the transmitted diseases. Mosquitoes, being poikilothermic organisms, are sensitive to the changes of temperature conditions. Rising air temperature can influence positively each elements of the WNF's vector chain including the abundance and the activity of the mosquito vectors, the viral replication rate of the virus, and the spatial range of WNF (*Reisen et al.*, 2006, *Paz et al.,* 2013, *Kinney et al.,* 2006; *Kilpatrick et al.,* 2008; *Andrade et al*., 2011). *Reeves et al.* (1994) and *Reiter et al.* (2001) found that WNF abundance and incidence are influenced by several environmental factors as heavy rains, irrigation, floods, dry and warm weather, unusually warm weather. The occurrence and incidence of the disease are primarily the function of the vector abundance. The virus is transmittable under very different climatic conditions from the cold temperate regions to the tropics. *Reisen et al.* (2006) proved that above-average summer temperatures in the United States resulted in an increased incidence of WNF due higher transmission rate of the virus by a *Culex* species to humans. The positive effect of increasing temperature on the minimum transmission rate of WNV were showed also in a modeling study (*Ruiz et al.,* 2010). Higher ambient temperatures also shorten the generation time of blood questing female mosquitoes and accelerate the evolution of the virus (*Paz et al.,* 2013; *Kilpatrick et al.,* 2008; *Meyer et al.,* 1990; *Ruiz et al.,* 2010). Positive correlations were observed between extreme high temperatures during heat-waves and the outbreak intensities of human WNF epidemics in many cases (*Dohm et al.,* 2002; *Cornel et al.,* 1993; *Epstein,* 2001; *Pats et al.,* 2003; *Paz,* 2006). It is also known that extreme hot temperature conditions can influence negatively the survival of mosquitoes (*Reisen,* 1995) and the replication of WNV in the vector mosquito organisms (*Reisen et al*., 2006).

The ontogeny of mosquitoes requires a certain threshold temperature. Experimental investigations reveal that there is a temperature limit of the infection of *Cx. pipiens* mosquitoes with WNV (*Dohm et al.,* 2002; *Dohm* and *Turell,* 2001): the ambient temperature limit is about 14 °C (*Cornel et al.* 1993). In a laboratory experiment, *Kilpatrick et al.* (2008) confirmed that the transmission of WNV is the exponential function of degree days. Elevated temperatures not only promote the increase of the mosquito populations (*Paz* and *Albersheim,* 2008), but shorten the full replication cycle of WNV in the infected mosquitoes (*Jia et al.,* 2007; *Kunkel et al.,* 2006) and accelerate the transmission of WNV (*Kilpatrick et al.,* 2008).

The role of precipitation in the determination of the WNF season and prevalence is more controversial (*Moudy et al.,* 2007) than that of the ambient temperature, and strongly depends on the climate of a certain region. At first inspect, it seems to be obvious that higher summer precipitation sums promote the population boom of mosquitoes providing more stable and extent aquatic habitats for the vectors. In the USA, indeed, it was found that precipitation above average can promote both the boom of mosquito populations and the above-average WNF incidences (*Soverow et al.,* 2009; *Takeda et al.,* 2003). Under tropical savannah

climate, where rainy and dry seasons alternate, the rainy season provide better conditions for the population growth of mosquitoes (*Campbell et al*., 2002). In Gibraltar, which area belongs to the Mediterranean climate region, WNF case number starts to increase in late summer parallel with the increase of precipitation, (*Paz et al.,* 2013). In contrast, there are evidences that expressly heavy rainfalls also can wash out the mosquito larvae from stagnant pools, channels, or even technotelmata causing the elimination of a complete mosquito generation (*Shaman et al.,* 2002; *Koenraadt et al.,* 2008). The role of the previous year's precipitation sums on the next year's WNF case numbers is also controversial. Higher precipitation sums in the previous year can either increase or decrease the current year's WNV transmission depending on the geographical location of the certain subtropical areas (*Paz* and *Semenza,* 2013; *Uejio et al.,* 2012; *Ruiz et al.,* 2010).

The aim of this study was the investigation of the influence of climatic factors on WNF case numbers in three Mediterranean (Greece, Italy, Israel, and the Palestinian Territories) and three continental climate countries (Hungary, Serbia, and Romania).

It was hypothesized that temperature has positive effect on WNF case numbers both in the Mediterranean and the temperate climate areas since temperature has general positive effect on mosquito ontogeny and the replication and transmission rate of the virus. Since under Mediterranean climate, summer is the driest season and in general, the rainy seasons provide better conditions for the population growth of mosquitoes, it was hypothesized that there is negative correlation between precipitation sums and West Nile fever case numbers in the Mediterranean countries. In contrast, it was also hypothesized that under continental climate, this correlation can be weaker than in the Mediterranean. In the continental parts of Europe, June can be the wettest month during the year creating good breeding sites for mosquitoes.

2. Materials and methods

2.1. Data

The historical West Nile fever data were derived from the ECDC's (European Center for Disease Control and Prevention) database in monthly temporal resolution (*ECDC: West Nile fever historical data 2011-2015)*. Both probable and confirmed cases were involved into the study. Data for Greece for 2015 and for Serbia for 2010 are missing. Case numbers were not converted into incidence values due to the relatively short studied period. The monthly precipitation sums and monthly mean temperature values were gained from the KNMI Climate Explorer (*Klein Tank et al.,* 2002) of the European Climate Assessment and Dataset (*Haylock et al.*, 2008), and they were averaged according to the covering grids of the NUTS3 regions where WNF cases occurred in 2011–2015. It means

that the selected grids cover only the areas where West Nile fever occurred in the given country in the period 2011–2015. *Table 1* shows the employed covering grids of the WNF case containing areas.

Table 1. Coordinates of the covering grids by countries (GR: Greece, HUN: Hungary, IT: Italy, RO: Romania, ISR: Israel and the Palestinian territories, and SRB: Serbia). Note that the selected covering grids are smaller than the total covering grids of the countries

Country	N(°)	E(°)
GR	38.00 to 41.50	20.25 to 25.50
HUN	45.75 to 48.50	16.00 to 23.00
IT	44.25 to 46.50	6.75 to 13.50
RO	43.75 to 47.25	23.00 to 29.50
ISR	29.75 to 33.25	34.25 to 35.75
SRB	42.25 to 46.00	19.25 to 22.75

2.2. Statistics and plot

Multiple linear regression method was used. Only the seasonal cases were involved into the study; the extra seasonal January, February, and December WNF cases of 2011, 2012, and 2013 in Hungary were neglected in the analysis. Case number data were involved in the study only if the monthly total or mean WNF case value was above 0. Temperature values below 0°C were not plotted in the diagrams due to the representation of the temperature and case number values on a common (second) y-axis. Although in case of two countries, the WNF case numbers of one-one year were missing from the database, the temperature and precipitation values of these years were plotted in the diagrams.

The average temperature values during the WNF seasons were calculated according to two different approaches:

1) The mean temperatures of the affected months when WNF cases occurred were averaged based on the following equation:

$$T_m = \frac{\sum_{i=1}^{n} T_{monthly\ mean,i}}{n} \quad (1)$$

where T_m is the mean temperature of the affected months, $T_{monthly\ mean,\ i}$ is the mean temperature of the *i*th month when WNF cases occurred, and *n* is the number of months when WNF cases occurred.

2) The temperature values were weighted with the number of WNF cases in each month when WNF cases occurred according to the following formula:

$$T_{mw} = \frac{\sum_{i=1}^{n}(T_{monthly\ mean,i} \times N_{WNF\ monthly,i})}{\sum_{i=1}^{n} N_{WNF\ monthly,i}}, \quad (2)$$

where T_{mw} is the weighted mean temperature of the affected months, $T_{monthly\ mean,\ i}$ is the mean temperature of the *i*th month and the $N_{WNF\ monthly,\ i}$ is the number of WNF cases in the *i*th month.

3. Results

3.1. Mediterranean countries

3.1.1. Greece

In Greece, the WNF season started in July (at 24.0 °C) and ended in October (at 14.9 °C). The highest cumulative case number was observed in August (55.52% of the total). The majority (93.1%) of the cases occurred from July to August in the period 2011–2014, when the mean temperature was 24.2 °C. In July and August, the driest months during the period of 20112014, the mean precipitation sum was 13.5 mm month^{-1}, that is 27.6% of the monthly mean precipitation sum (48.7 mm month^{-1}). In Greece, the peak of the annual case number approximately coincided with the annual temperature maximum and precipitation minimum (*Fig. 1*).

The mean monthly temperature was 21.8 °C, the mean air temperature weighted with the number of cases was 24.4 °C in the months of observations of the autochthon cases (maximum: 26.1 °C, minimum: 13.1 °C). The maximum length of the season was 3 months. The data of 2015 is missing. The maximum length of the season was 4 months (excluding the imported cases; *Fig. 2*).

Based on the multiple regression analysis, strong negative correlation exists between the mean monthly precipitation sums and the corresponding WNF case numbers. In contrast, strong positive correlation was found between the mean monthly temperatures and WNF case numbers in Greece (*Table 2*).

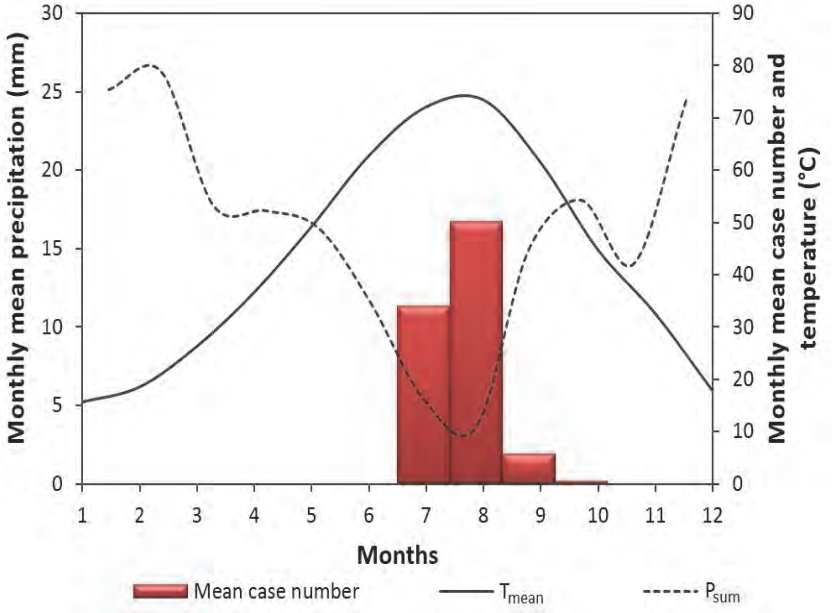

Fig.1. The mean monthly case numbers compared to the run of the mean monthly temperatures and the precipitation sums in Greece, 2011-2014.

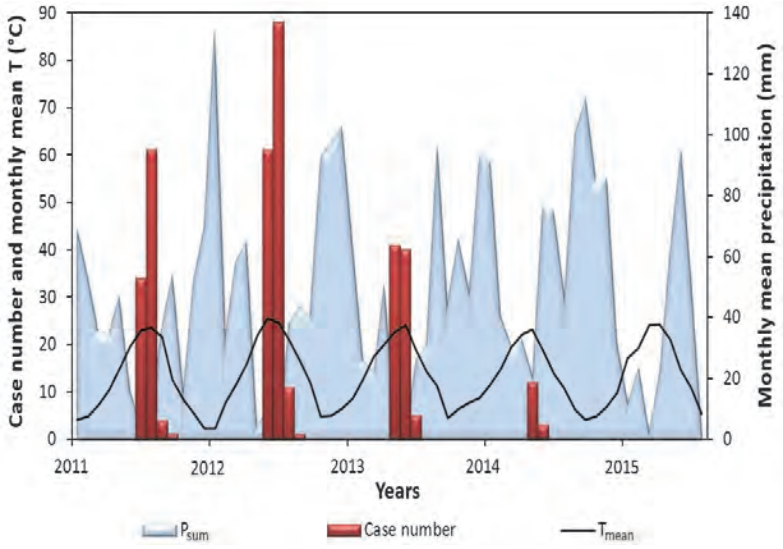

Fig.2. The number of WNF cases in 2011 to 2014 in Greece and the run of the monthly mean temperature averaged to the grid of the affected areas of the country. The WNF data of 2015 is missing from the ECDC's public historical database.

Table 2. The results of the multiple regressions in case of Greece.

Correlation matrix	T_{mean}	P_{sum}	Case number
T_{mean}	1	–0.818	0.743
P_{sum}	–	1	–0.717
Case number	–	–	1
Multiple R^2=0.5879			
Adjusted multiple R^2=0.5055			

3.1.2. Israel and the Palestinian territories

In Israel and the Palestinian territories, most of the WNF cases (the 83.74% of the total) occurred in June, July, and August (*Fig. 3*). The WNF season started before the warmest months in June (at 21.6 °C) and ended in October (at 18.75 °C). In July and August during 2011–2015, in Israel and the Palestinian territories, the mean precipitation sum was 0.2 mm month^{-1}, that is the 0.4% of the monthly mean precipitation sum (42.7 mm month^{-1}). The peak of the annual case number coincided with the annual temperature maximum and the precipitation minimum (*Fig. 3*).

The mean monthly temperature was 28.1 °C, the mean air temperature weighted with the number of cases was 28.8 °C in the months of observations of the autochthon cases (maximum: 30.4 °C, minimum: 23.1 °C). The maximum length of the season was 3 months (*Fig. 4*).

According to the multiple regression analysis, moderate strong negative correlation exists between the mean monthly precipitation sums and the corresponding WNF case numbers. In contrast, strong positive correlation was found between the mean monthly temperatures and WNF case numbers in Israel and the Palestinian territories (*Table 3*).

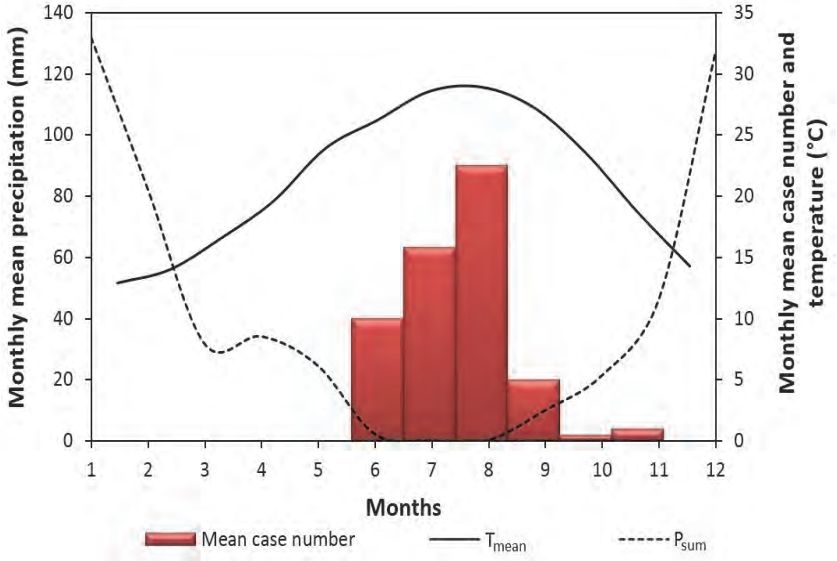

Fig.3. The mean monthly case numbers compared to the run of the mean monthly temperatures and the precipitation sums in Israel and the Palestinian territories, 2011-2015.

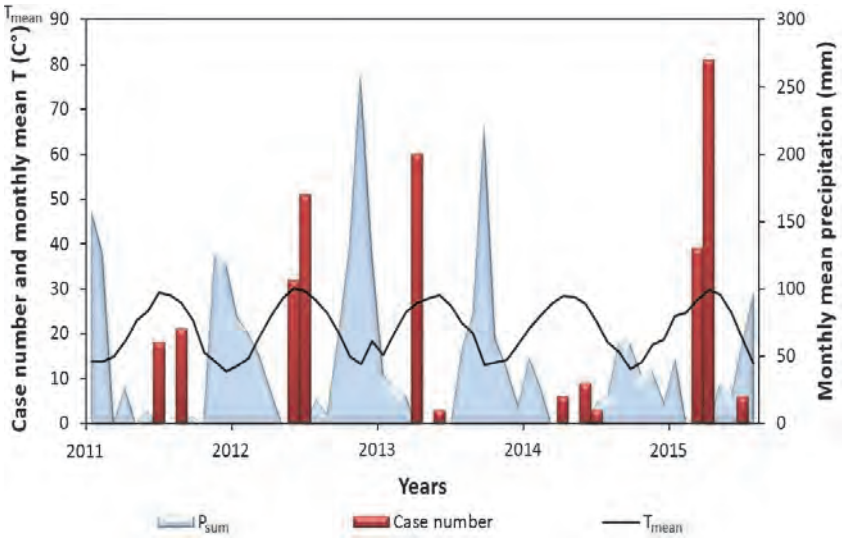

Fig.4. The number of WNF cases from 2011 to 2015 in Israel and the Palestinian territories, and the run of the monthly mean temperature averaged to the grid of the affected areas of the country.

Table 3. The results of the multiple regressions in case of Israel and the Palestinian territories

Correlation matrix	T_{mean}	P_{sum}	Case number
T_{mean}	1	–0.885	0.746
P_{sum}	–	1	–0.566
Case number	–	–	1
Multiple R^2=0.5966			
Adjusted multiple R^2=0.507			

3.1.3. Italy

In Italy, the WNF season started in August (at 22.3 °C) and ended in November (at 8.6 °C). Most of the WNF cases (89.17%) occurred in August and September. The peak of the annual case number (the 55.5% of the cases) was observed in August. The first annual cases appeared in the warmest month and showed a clear decreasing trend from July to November. In August and September during 2011–2015 in Italy, the mean precipitation sum was 76.1 mm month^{-1}, that is the 91.5% of the monthly mean precipitation sum (83.2 mm month^{-1}). In Italy, the peak of the annual case number immediately followed the annual temperature maximums and coincided with the precipitation minimum (*Fig. 5*).

The mean monthly temperature was 15.8 °C, the mean air temperature weighted with the number of cases was 18.5°C in the months of observations of the autochthon cases (maximum: 22.8 °C, minimum: 6.3 °C). The maximum length of the season was 3 months (*Fig. 6*).

According to the multiple regression analysis, moderate strong negative correlation exists between the mean monthly precipitation sums and the corresponding WNF case numbers. In contrast, strong positive correlation was found between the mean monthly temperatures and WNF case numbers in Italy (*Table 4*).

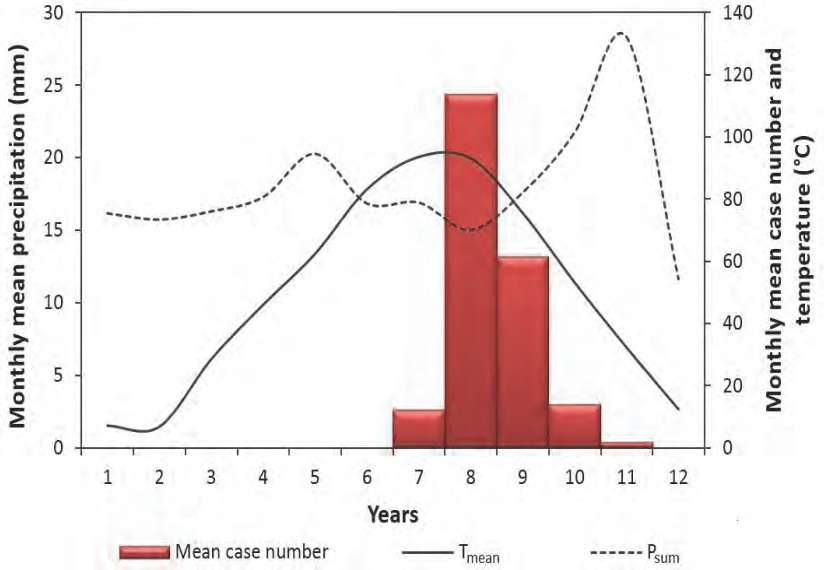

Fig. 5. The mean monthly case numbers compared to the run of the mean monthly temperatures and the precipitation sums in Italy, 2011–2015.

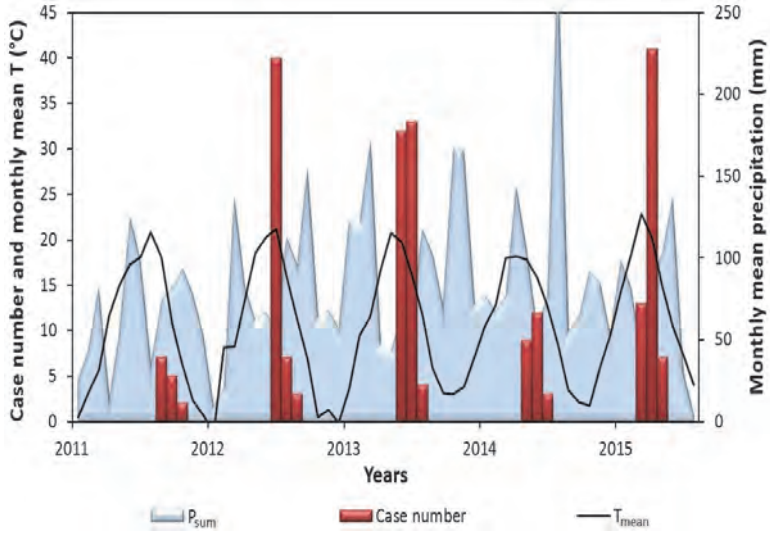

Fig. 6. The number of WNF cases from 2011 to 2015 in Italy, and the run of the monthly mean temperature averaged to the grid of the affected areas of the country.

Table 4. The results of the multiple regressions in case of Italy

Correlation matrix	T_{mean}	P_{sum}	Case Number
T_{mean}	1	–0.533	0.661
P_{sum}	–	1	–0.426
Case Number	–	–	1
Multiple R^2=0.44444			
adjusted multiple R^2=0.3433			

3.2. Continental countries

3.2.1. Hungary

In Hungary, the WNF season started in July (at 21.3 °C) and ended in November (at 6.1 °C) excluding the imported cases. In 2011, only one imported case was explored. From 2013, most of the cases were observed in September. In 2013 and 2014, each of the autochthon cases was recorded from August to October. The 64.5% of the total cases occurred in September. In August and September during 2011–2015 in Hungary, the mean precipitation sum was 51.6 mm month^{-1} that is the 114.9% of the monthly mean precipitation sum (44.9 mm month^{-1}). In Hungary, the peak of the annual case number followed the annual temperature maximum and the precipitation minimum (*Fig. 7*).

The mean monthly temperature was 16.7 °C, the mean air temperature weighted with the number of cases was 17.4°C in the months of observations of the autochthon cases (maximum: 23.5 °C, minimum: 7.6 °C). The maximum length of the season was 3 months (excluding the extra seasonal cases; *Fig. 8*).

According to the multiple regression analysis, very weak negative correlations exists between the mean monthly precipitation sums and the corresponding autochthonous WNF case numbers. In contrast, weak positive correlation was found between the mean monthly temperatures and WNF case numbers in Hungary (*Table 5*).

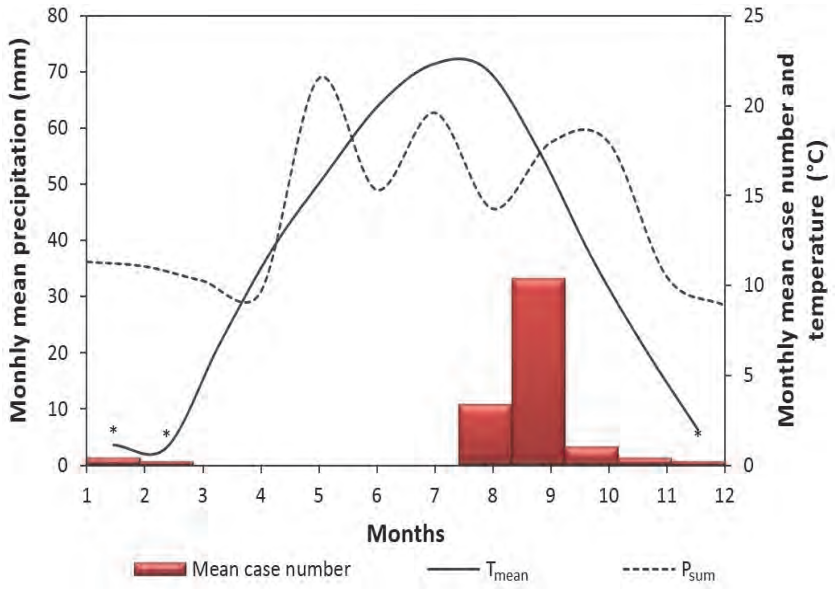

Fig. 7. The mean monthly case numbers compared to the run of the mean monthly temperatures and the precipitation sums in Hungary, 2011–2015; *: extra seasonal cases.

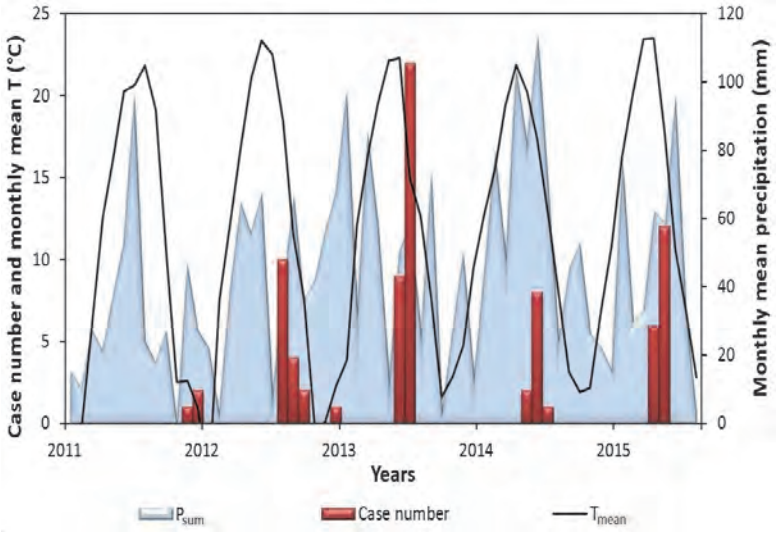

Fig. 8. The number of WNF cases from 2011 to 2015 in Hungary, and the run of the monthly mean temperature averaged to the grid of the affected areas of the country.

Table 5. The results of the multiple regressions in case of Hungary.

Correlation matrix	T_{mean}	P_{sum}	Case Number
T_{mean}	1	0.181	0.202
P_{sum}	–	1	–0.131
Case Number	–	–	1
Multiple R^2=0.0696			
adjusted multiple R^2=0			

3.2.2. Serbia

In Serbia, the WNF season started in June and lasted to November. Most of the WNF cases (87.8%) occurred in June, July, and August. The WNF season started before the warmest months in June (at 18.9 °C) and ended in October (at 7.0 °C). In June to August during 2012–2015 in Serbia, the mean precipitation sum was 49.1 mm month^{-1}, that is the 79.8% of the monthly mean precipitation sum (61.5 mm month^{-1}). In Serbia, the peak of the annual case number preceded the annual temperature maximum and the precipitation minimum (*Fig. 9*).

The mean monthly temperature was 17.3 °C, the mean air temperature weighted with the number of cases was 19.5 °C in the months of observations of the autochthon cases (maximum: 23.6 °C, minimum: 7.4 °C). The maximum length of the season was 5 months (*Fig. 10*).

According to the multiple regression analysis, very weak negative correlation was found between the mean monthly precipitation sums and the corresponding WNF case numbers. In contrast, weak positive correlation was found between the mean monthly temperatures and WNF case numbers in Serbia (*Table 6*).

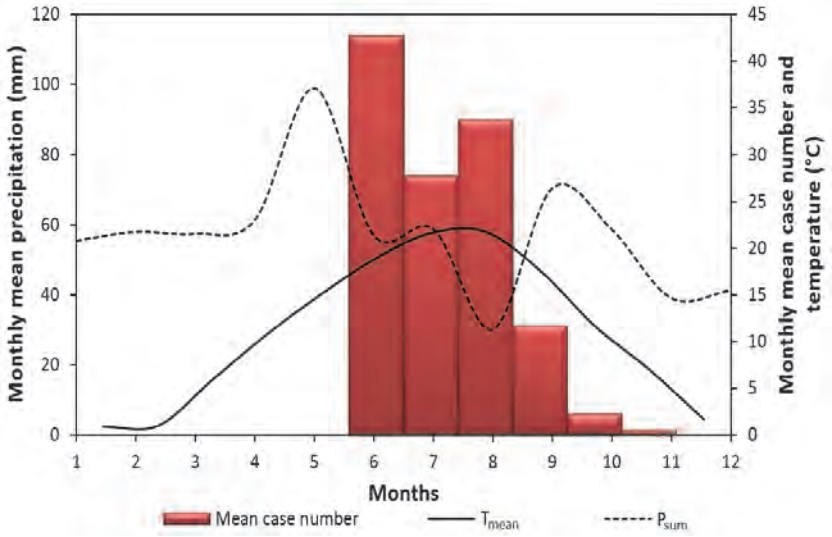

Fig. 9. The mean monthly case numbers compared to the run of the mean monthly temperatures and the precipitation sums in Serbia, 2012–2015.

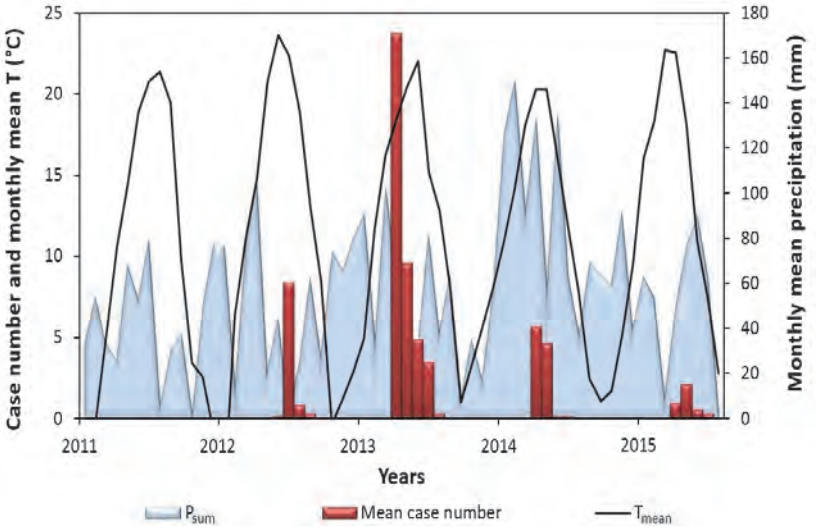

Fig. 10. The number of WNF cases from 2012 to 2015 in Serbia, and the run of the monthly mean temperature averaged to the grid of the affected areas of the country. The WNF data of 2011 is missing from the ECDC's public historical database.

Table 6. The results of the multiple regression analysis in case of Serbia

Correlation matrix	T_{mean}	P_{sum}	WNF
T_{mean}	1	–0.289	0.317
P_{sum}	–	1	–0.141
WNF	–	–	1
Multiple R^2=0.1031			
Adjusted Multiple R^2=0			

3.2.3. Romania

In Romania, the WNF season started in July (at and 21.6 °C) ended in November (at 5.3 °C). Most of the WNF cases (88.8%) occurred in August and September. (Fig.10) of which 48.5% in August. The first cases appeared in the warmest months and WNF season lasted from summer to the end of the vegetation season. In August and September during 2011–2015 in Romania the mean precipitation sum was 40.6 mm month^{-1} that is the 88.0% of the monthly mean precipitation sum (46.2 mm month^{-1}). In Romania, the peak of the annual case number occurred after the annual temperature maximum and precipitation minimum (*Fig. 11*.)

The mean monthly temperature was 17.0 °C, the mean air temperature weighted with the number of cases was 19.1 °C in the months of observations of the autochthon cases (maximum: 22.9 °C, minimum: 5 °C). The maximum length of the season was 3 months (*Fig. 12*).

According to the multiple regression analysis, very weak negative correlation exists between the mean monthly precipitation sums and the corresponding WNF case numbers. In contrast, moderate strong positive correlation was found between the mean monthly temperatures and WNF case numbers in Romania (*Table 7*).

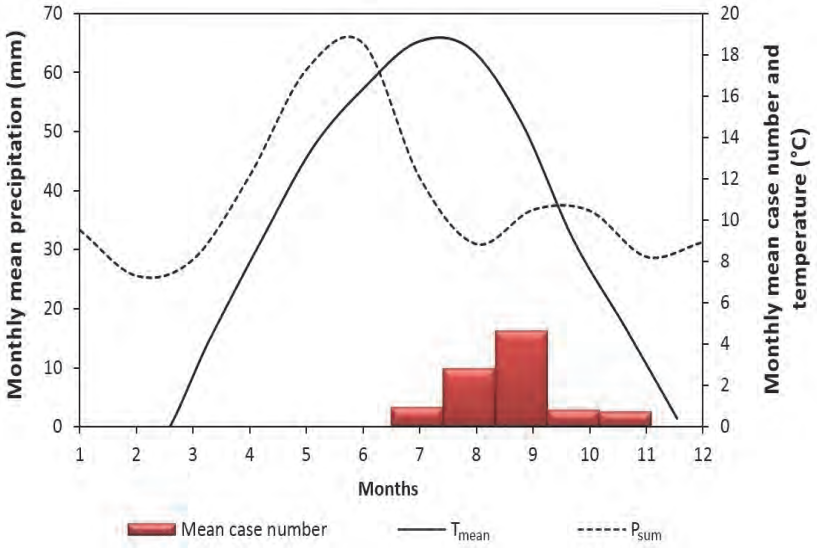

Fig.11. The mean monthly case numbers compared to the run of the mean monthly temperatures and the precipitation sums in Romania, 2011–2015.

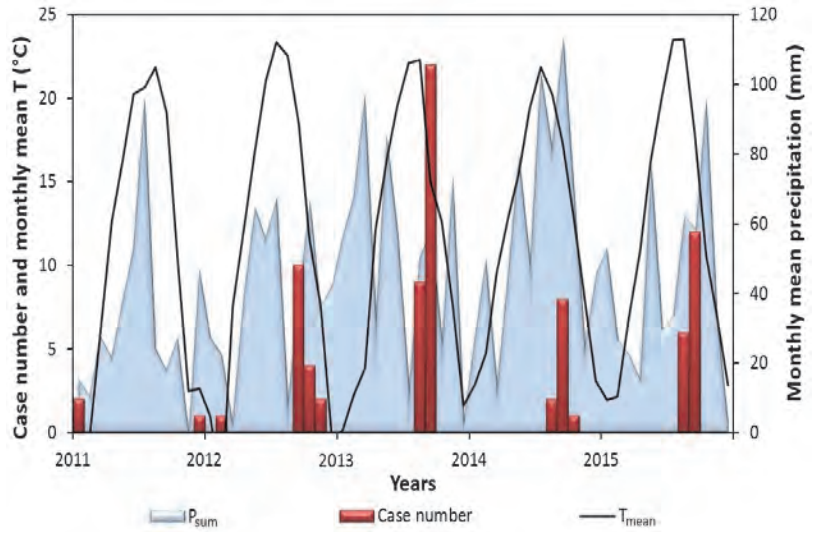

Fig.12. The number of WNF cases in 2011 to 2015 in Romania and the run of the monthly mean temperature averaged to the grid of the affected areas of the country.

Table 7. The results of the multiple regressions in case of Romania

Correlation matrix	T_{mean}	P_{sum}	Case
T_{mean}	1	0.573	0.522
P_{sum}	–	1	–0.183
Case	–	–	1
Multiple R^2=0.6182			
Adjusted multiple R^2=0.5333			

3.3. Comparisons

The mean monthly temperature in the months, when WNF cases were observed, was between 15.8–28.1 °C (SD: 4.73). The case number weighted mean of the monthly temperature during the WNF cases-related months ranged between 17.4 and 28.8 °C (SD: 4.40). West Nile fever seasons started in June or July in the studied countries at 18.9–24.0 °C mean monthly temperatures (average: 21.6 °C, SD: 1.65). The WNF season ended in October or November at 18.7–5.3 mean monthly temperatures (average: 10.1 °C, SD: 5.43). The highest summarized case numbers were observed in June (Serbia), August (Greece, Israel and the Palestinian territories, and Italy), or September (Hungary and Romania; *Table 8*).

In each of the studied countries positive correlations ($0.202<r^2<0.746$; average: 0.531, SD: 0.23) were found between the monthly mean temperature and the WNF case number sums. In contrast, in each of the studied countries negative correlations ($-0.131>r^2>-0.717$; average: –0.360; SD: 0.25) were found between the monthly precipitation sums and the WNF case number sums (*Table 9*).

Table 8. The mean temperature and the case-weighted temperature values under the months when WNF occurred and the average monthly temperature values at the start and the end of the seasons (GR: Greece, HUN: Hungary, IT: Italy, RO: Romania, ISR: Israel and the Palestinian territories, and SRB: Serbia)

Country	Tmean(°C)	Tmean weighted (°C)	T_{Start} (°C)	T_{End} (°C)
GR	21.8	24.4	24.0	14.9
HUN	16.7	17.4	21.3	6.1
IT	15.8	18.5	22.3	8.6
RO	17.0	19.1	21.6	5.3
ISR	28.1	28.8	21.6	18.7
SRB	17.3	19.5	18.9	7.0

Table 9. The regression coefficient according to the multiple regression results of the climatic variables and the case number values of the identical months (GR: Greece, HUN: Hungary, IT: Italy, RO: Romania, ISR: Israel and the Palestinian territories, and SRB: Serbia)

Country	R^2 T_{mean} (°C) x Case number	R^2 P_{sum} (mm) x Case number
GR	0.743	–0.717
HUN	0.202	–0.131
IT	0.661	–0.426
RO	0.522	–0.183
ISR	0.746	–0.566
SRB	0.317	–0.141

WNF cases mainly occur in the warm Mediterranean and the warm/hot summer continental areas of Europe. The warm or hot summer continental (Dfa, Dfb; e.g., the main part of Hungary) and the hot and dry summer Mediterranean climate (Csa; e.g., the main part of Greece or the north part of Israel), or the subtropical areas (Cfa; in the Mediterranean mountain ranges of Italy) are the most frequent climates where WNF occur in Europe. WNF is missing from the polar, alpine, and atlantic climate areas of the continent, excluding the maritime temperate regions (Cfb; southern slopes of the Alps in Italy). In Levant, WNF cases occur in hot summer Mediterranean (Csa); and warm semi-arid climates (Bsh; according to the Köppen-Geiger climate classification system (Table 10).

Table 10. Climate zones of the areas where WNF occurred in the studied countries according to the Köppen-Geiger climate classification system (BSh: warm semi-arid [hot steppe] climate, Csa: warm Mediterranean climate, Cfa: subtropical climate, Cfb: oceanic cimate, Dfa: hot summer continental climate, Dfb: warm summer continental climate; GR: Greece, HUN: Hungary, IT: Italy, RO: Romania, ISR: Israel and the Palestinian territories, and SRB: Serbia)

Country	Köppen-Geiger climate classification
GR	Csa, (Cfa, Dfb)
HUN	Dfb, (Dfa)
IT	Dfa, Cfa, Cfb, (Csa)
RO	Dfa, Dfb
ISR	Csa, BSh
SRB	Dfa, (Dfb)

4. Discussion

Temperature, rainfall, and humidity predominate the occurrence, morbidity and transmission dynamics of vector-borne diseases (*Githeko et al.*, 2000; *Gubler et al.*, 2001; *Gubler*, 1998), which is especially true for mosquito-borne infections (*Reiter*, 2001). Climate projections predict decreases in rainfall and temperature, and such changes have the potential to increase the risk of arbovirus transmission by increasing the distribution and abundance of vectors, and the length of mosquito vector and arbovirus seasons (*Russel*, 1998). *Whelan et al.* (2003) pointed out that rainfall is an important, positive risk indicator of mosquito abundance and mosquito-borne arbovirus incidence. In contrast, it was found that temperature and precipitation have different strength of impacts on the WNF case numbers in the Mediterranean and temperate climate countries. In general, monthly case number of WNF showed stronger correlations with the two climatic variables in the Mediterranean countries than in the continentals: strong positive correlations (Pearson's correlation coefficients were between 0.6 and 0.7) were found between the monthly mean temperatures and the WNF case numbers in the Mediterranean and weak to moderate strong (Pearson's correlation coefficients were between 0.2 and 0.5) positive correlations in the continental climate countries. Strong and moderately strong negative correlations (Pearson's correlation coefficients were between –0.7 and –0.4) were found between the monthly sum of precipitation and the WNF case numbers in the Mediterranean and very weak (Pearson's correlation coefficients were –0.1) negative correlations in the continental climate countries. These results are in accordance with the observations that under summer arid Mediterranean, climatic conditions, the positive effect of precipitation (mainly of heavy rainfalls) is more obvious and expressed on mosquito populations (*Paz* and *Albersheim,* 2008) than in the humid temperate regions, where the mosquitoes can find their breeding habitats without extreme rainfall events in summers (*Trawinski et al.,* 2008).

Platonov et al. (2008) found that WNF incidence was higher in the years with mild winter and hot summer. Rainy and cold summers, which occur in the Atlantic coasts are not favorable for mosquitoes. A very similar correlation was found in case of the distribution limiting factors of another Diptera vector group: the climatic requirements of *Phlebotomus* species. Sandflies avoid the Atlantic coasts of Western Europe due to the relatively cold, rainy summers, and only few sandfly species – e.g., *Phlebotomus perniciosus* Newstead (1911) – can tolerate the rainy summer climate of these areas (*Trájer et al.*, 2013). In Hungary, the effect of floods on the case number of WNF and the effect of river regulation on the mosquito abundance and diversity were demonstrated previously (*Trájer et al.*, 2014; *Trájer et al.*, 2015). The positive effect of temperature on the case number is clear and well-interpretable based on the ecology of the main vector *Culex* mosquitoes. Higher temperatures increase the mosquito activity and shorten the ontogeny time. Using climate envelope modeling, *Trájer et al.* (2014) found that global warming can enhance the European range of WNF.

As it was shown, the negative correlation between WNF case numbers and precipitation sums with a varying regression coefficient was observed in each country. This apparent contradiction between the findings of *Whelan et al.* (2003) and the results of this study partly can be resolved by the hypothesis, that not the higher mean precipitation itself, but the occasional heavy rainfalls can increase the case number of WNF under certain, mainly Mediterranean climatic areas. These occasional rainfalls do not increase significantly the summer mean precipitation sums providing a misleading consequence, that precipitation is a negative effector.

Summer drought has some potentially beneficial effects on mosquito populations. Water level decrease of different standing waters (e.g., backwaters and shallow lakes) during the dry period of summer may provide excellent habitats for mosquito larvae (*Shaman et al.,* 2002). Concerning even the 2 to 14 days latency, it can be concluded that low precipitation has no negative effect on the monthly mean WNF case number. In the Mediterranean and continental parts of Europe, summers are hot and dry excluding the westernmost part of the Mediterranean basin and the highest elevations of the Mediterranean mountain ranges. Nevertheless, the rapid evaporation of small and medium-sized waters in summer may result in the desiccation of the potential mosquito breeding habitats. Desiccating backwaters provide continuously warm mosquito larva habitats with flourishing algal communities, which conditions are highly preferable for several mosquito species. The desiccation of these larva habitats can explain the fact that the season of WNF is no longer in warmer climate conditions than in the colder parts of Europe. It is also known that the larvae of some mosquito species as *Aedes albopictus* Skuse (1894) or *Ochlerotatus sticticus* Meigen (1838) can survive the total desiccation of their habitats persisting in the wet mud of the former small waters (*Schäfer* and *Lundström,* 2006). Eutrophication cause the bloom of cyanobacteria and green algae, the accumulation of organic materials, while the consequent depletion of the soluble oxygen content is highly detrimental for fish predators. Algae and organic particles provide plentiful food for mosquito larvae, which organisms gain the oxygen directly from the atmospheric air storage. *Roehr* (2012) also found in the arid and semi-arid areas, where streams frequently dry up in summer, that the decreased water flow and the consequently appearing small waters provide ideal breeding habitats for mosquitoes. These facts can explain why in continental areas the hot and dry summers facilitate the outbreak of certain mosquito populations (*Reisen,* 1995). Shrinking water surfaces also can facilitate the contacts between vector mosquito and host bird populations (*Shaman et al.,* 2005). As already was mentioned, *Soverow et al.* (2009) and *Takeda et al.* (2003) found that in the USA, the average-exceeding precipitation conditions increase the WNF incidences. We should accept the conclusion of *Landesman et al.* (2007), that the effect of precipitation on mosquito populations and mosquito-borne diseases depends on the ecology of the mosquito vectors, the geographic location, and the characteristic climate of the area.

Temperature and precipitation affect the case numbers of mosquito-borne diseases in different ways. For example, the historical analysis of the effect of mean monthly temperature values and monthly precipitation sums on the autochthonous malaria cases of Hungary showed, that while temperature was the primary modulator of the relative annual run of the disease, the absolute malaria case number still depended on the summer precipitation patterns (*Trájer* and *Hammer,* 2016). The relatively late, mainly July and August onset of WNF remained a not completely understood phenomenon. Although birds are the main hosts of the virus, and the transmission of WNF from birds to humans requires a certain time through the increasing population of the infected mosquitoes in summer, the latency of the outbreak of the onset seems to be somewhat prolonged. It is known that, e.g., the former autochthonous malaria season reached its peak in June following the late spring-early summer boom of the potential mosquito populations in Hungary. It should be added, that the main vectors of malaria and WNF are not the same. This is an interesting outcome in the light of the observations that WNV plausibly can persist also in chronically infected vertebrates and hibernating female *Culex* mosquitoes (*Cornel et al.*, 1993; *Nasci et al.*, 2001 and *Taylor et al.*, 1956). This result is not supported by the always changing regional distribution of the disease in Hungary (*Trájer et al.*, 2014) and also in several parts of Europe, which partly can be the consequence of the re-introduction of the virus by migratory birds as it was hypothesized as an important determinant of the observed seasonality by *Chunikhin et al.* (1973), *Ernek et al.* (1977). The more rapid decrease of the case number compared to the mosquito activity may underline the role of human activity on the run of the case number and the temperature-dependent transmission rate of WNV.

5. Conclusions

Based on the Köppen-Geiger climate classification system, the hot summer continental and hot and dry summer Mediterranean climate zones are the most suitable areas for the West Nile virus and its vectors. The range of WNV avoids the boreal, oceanic, and mountainous climate zones of Europe. In contrast to the prior expectations, in each of the studied countries, negative correlations were found between the monthly precipitation sums and WNF case numbers. However, it can be rather the consequence of the fact, that, rainy summers occur in the Atlantic coasts of Europe, where summer temperatures are less than the activity and developmental optimum of the mosquito vectors, than a direct negative correlation between rainfall and case number. Although heavy rainfall events and the consequent floods may have positive influence on the population size of mosquitoes, in each of the studied countries, negative correlations were found between WNF incidences and precipitation sums. The lengths of the main part of the WNF seasons are similar and not clearly dependent on the geographical position of a given country, but in fact, in Israel and the Palestinian territories, the

WNF season starts two months earlier than in Hungary. It is plausible, that the annual migration activity of birds and the activity of the mosquito vectors are also strongly influenced by the length of the daytime hours.

Acknowledgement: The author acknowledges the E-OBS dataset from the EU-FP6 project ENSEMBLES (http://ensembles-eu.metoffice.com) and the data providers in the ECA&D project (http://www.ecad.eu)" Haylock, M.R., N. Hofstra, A.M.G. Klein Tank, E.J. Klok, P.D. Jones and M. New. 2008: A European daily high-resolution gridded dataset of surface temperature and precipitation. J. Geophys. Res (Atmospheres), 113, D20119, doi: 10.1029/2008JD10201. The study was supported by EFOP-3.6.1-16-2016-00015.

References

Andrade, C.C., Maharaj, P.D., Reisen, W.K., and Brault, A.C., 2011: North American West Nile virus genotype isolates demonstrate differential replicative capacities in response to temperature. *J. Gen. Virol. 92*, 2523–2533.

Bakonyi, T., Ivanics, É., Erdélyi, K., Ursu, K., Ferenczi, E., Weissenböck, H., and *Nowotny, N.,* 2006: Lineage 1 and lineage 2 strains of encephalitic West Nile virus, Central Europe. *Emerg. Infect. Dis. 12,* 618–623.

Bardos, V., Adamcová, J., Dedei, S., Gjini, N., Rosický, B., and *Simkova, A*., 1959: Neutralizing antibodies against some neurotropic viruses determined in human sera in Albania. *J. Hyg. Epidemiol. Microbiol. Immunol. 3,* 277–282.

Barzon, L., Pacenti, M., Ulbert, S., and *Palù, G*., 2015: Latest developments and challenges int he diagnosis of human West Nile virus infection. *Expert Rev. Anti. Infect. Ther. 13,* 327–342.

Butenko, A.M., Chumakov, M.P., Bashkirtsev, V.N., Tkachenko, E.A., Rubin, S.G., and *Stolbov, D.N.,* 1968: New investigations of West Nile virus infections in the USSR-Astrakhan region. *Materialy XV Nauchnoi Sessii Instituta Poliomielita i Virusnykh Encefalitov (Moskva) 3,* 175–6.

Campbell, G.L., Marfin, A.A., Lanciotti, R.S., Gubler, D.J., 2002: West Nile Virus. *Lancet Infect. Dis. 2,* 519–529.

CDC, West Nile Virus, Symptoms & Treatment: https://www.cdc.gov/westnile/symptoms/index.html. [accessed: 02. 08. 2016].

Chumakov, M.P., Belyaeva, A.P., Butenko, A.M., and *Martyanova, L.I.,* 1968: Isolation of West Nile virus from *Hyalomma plumbeum plumbeum* Panz. ticks. *Tr. Inst. Polio. Virusn. Encefalitov. (Moskva) 13,* 365.

Chunikhin, S., 1973: Introduction to the ecology of arboviruses. *Meditsinskaya virusologia 21*, 7–88.

Cornel, A.J., Jupp, P.G., and *Blackburn, N.K.,* 1993: Environmental temperature on the vector competence of *Culex univittatus* (Diptera: Culicidae) for West Nile virus. *J. Med. Entomol. 30*, 449–456.

Dohm, D.J. and *Turell, M. J.,* 2001: Effect of incubation at overwintering temperatures on the replication of West Nile Virus in New York *Culex pipiens* (Diptera: Culicidae). *J. Med. Entomol. 38,* 462–464.

Dohm, D.J., O'Guinn, M. L., and *Turell, M. J.,* 2002: Effect of environmental temperature on the ability of *Culex pipiens* (Diptera: Culicidae) to transmit West Nile Virus. *J. Med. Entomol*. *39,* 221–225.

Drägänescu, N., 1977: Epidemic outbreak caused by West Nile virus in the crew of a Romanian cargo ship passing through the Suez Canal and the Red Sea on route to Yokohama. *Rev. Roum. Med. Ser. Virol. 28*, 259–262.

ECDC: West Nile fever historical data 2011-2015 – „European Center for Disease Control and Prevention, ECDC. West Nile fever maps.," [Online]. http://ecdc.europa.eu/en/healthtopics/west_nile_fever/West-Nile-fever-maps/pages/index.aspx [accessed: 02. 08. 2016].

Epstein, P. R., 2001: West Nile Virus and the climate. *J. Urban Health 78,* 367–371.

Erdélyi, K., Ursu, K., Ferenczi, E., Szeredi, L., Rátz, F., Skáre, J,. and *Bakonyi, T., 2006:* Clinical and pathologic features of Lineage 2 West Nile virus infections in birds of prey in Hungary. *Vector Borne Zoonotic Dis. 7,* 181–188.

Ernek, E., Kozuch, O., Nosek, J., Teplan, J., and *Folk, C.,* 1977: Arboviruses in birds captured in Slovakia. *J. Hyg. Epidemiol.* Microbiol. *Immunol. 21,* 353–359.

Githeko, A.K., Lindsay, S.W., Confalonieri, U.E., and *Patz, J.A.,* 2000: Climate change and vector-borne diseases: a regional analysis. *Bull. World. Health. Organ. 78*, 1136–1147.

Goldblum, N., Sterk, V.V., and *Paderski, B.,* 1954: West Nile Fever. The clinical features of the disease and the isolation of West Nile Virus from the blood of nine human cases. *Am. J. Hyg. 59,* 89–103.

Gubler, D.J., Reiter, P., Ebi, K. L., Yap, W., Nasci, R., and *Patz, J.A.,* 2001: Climate variability and change in the United States: potential impacts on vector-and rodent-borne diseases. *Environ. Health Perspect. 109(Suppl 2),* 223.

Gubler, D. J., 1998: Resurgent vector-borne diseases as a global health problem. *Emerg. Infect. Diseases 4,* 442.

Hannoun, C., Panthier, R., Mouchet, J. and Eouzan, J. P., 1964: Isolement en France du virus West-Nile à partir de malades et du vecteur *Culex modestus* Ficalbi. *C. R. Hebd.* Seances *Acad. Sci. 259,* 4170.

Hayes, E.B., Sejvar, J.J., Zaki, S.R., Lanciotti, R.S., Bode, A.V., and *Campbell, G.L.,* 2005: Virology, Pathology, and Clinical Manifestations of West Nile Virus Disease. *Emerg Infect Dis. 11.*

Haylock, M.R., Hofstra, N., Klein Tank, A.M.G., Klok, E.J., Jones, P.D., and New, M., 2008: A European daily high-resolution gridded data set of surface temperature and precipitation for 1950–2006. *J. Geophys. Res.: Atmos. 113*(D20).

Hubálek, Z. and *Halouzka, J., 1999:* West Nile Fever – a reemerging mosquito-borne viral disease in Europe. *Emerg. Infect. Dis. 5,* 643–650.

Hubálek, Z. and *Halouzka, J.,* 1996: Arthropod-borne viruses of vertebrates in Europe. Institute of Landscape Ecology, Brno; pp.95.

Ivanov, K. S., Lobzin, I., and *Nikolaev, V. P.,* 1986: [West Nile fever (West Nile encephalitis)]. *Zh. Mikrobiol. Epidemiol. Immunobiol*. *7*, 110–113.

Jia, Y., Moudy R. M., Dupuis II A. P., Ngo K. A., Maffei, J. G., Jerzak, G. V., Franke, M. A., Kauffman, E. B., and *Kramer, L. D.* 2007: Characterization of a small plaque variant of West Nile Virus isolated in New York in 2000. *Virology 367,* 339–347.

Kemenesi, G., Dallos, B., Oldal, M., Kutas, A., Földes, F., Németh, V., Reiter, P., Bakonyi, T., Bányai, K., and *Jakab, F.,* 2014: Putative novel lineage of West Nile virus in *Uranotaenia unguiculata* mosquito, Hungary. *Virus Dis. 25*, 500–503.

Kilpatrick, A.M., Meola, M.A., Moudy, R.M., and *Kramer, L.D.,* 2008: Temperature, viral genetics, and the transmission of West Nile virus by *Culex pipiens* mosquitoes. *PLoS Pathog. 4,* e1000092.

Kilpatrick, A.M., Kramer, L.D., Jones, M.J., Marra, P.P., and *Daszak, P.,* 2006: West Nile virus epidemics in North America are driven by shifts in mosquito feeding behavior. *PLoS Biol. 4,* e82.

Kinney, R.M., Huang, CY. H., Whiteman, M.C., Bowen, R.A., Langevin, S.A., Miller, B.R., and Brault, A.C., 2006: Avian virulence and thermostable replication of the North American strain of West Nile virus. J. Gen. Virol. *87*, 3611-3622.

Klein Tank, A.M.G., Wijngaard, J.B., Können, G.P., Böhm, R., Demarée, G., Gocheva, A., Mileta, M., Pashiardis, S., 2002*: Hejkrlik, L., Kern-Hansen, C., Heino, R., Bessemoulin, P., Müller-Westermeier, G., Tzanaoku, M., Szalai, S., Pálsdóttir, T., Fitzgerald, D., Rubin, S., Capaldo, M., Maugeri, M., Leitass, A., Bukantis, A., Aberfeld, R, van Engelen, A. F. V., Forland, E., Mietus, M., Coelho, F., Mares, C., Razuvaev, V., Nieplova, E., Cegnar, T., Antonio López, J., Dahlstöm, B., Moberg, A., Kirhhofer, W., Ceylan, A., Pachaliuk, O., Alexander, L.V.,* and *Petrovic, P.,* 2002: Daily dataset of 20th-century surface air temperature and precipitation series for the European Climate Assessment. *Int. J. Climatol. 22*, 1441–1453.

Koenraadt, C.J.M. and *Harrington, L.,* 2008: Flushing effect of rain on container-inhabiting mosquitoes *Aedes aegypti* and *Culex pipiens* (Diptera: Culicidae). J. Med. Entomol. *45*, 28–35.

Koopmans, M., Martina, B., Reusken, C., and *van Maanen, K.,* 2007: West Nile virus in Europe: waiting for the start of the epidemic? In (Ed.: *Takken, W*. and *Knols, B.G.J.*) Emerging pests and vector-borne diseases in Europe, Ecology and control of vector-borne diseases Vol 1. Vageningen Academic Publishers, The Netherlands, 123–151.

Kostyukov, M. A., Alekseev, A. N., Bulychev, V. P., and Gordeeva, Z. E., 1986: Experimental infection of *Culex pipiens* mosquitoes with West Nile virus by feeding on infected *Rana ridibunda* frogs and its subsequent transmission. *Med. Parazitol. (Mosk) 6*, 76–78.

Kunkel, K.E., Novak, R.J., Lampman, R. L., and *Gu, W.,* 2006: Modeling the impact of variable climatic factors on the crossover of *Culex restauns* and *Culex pipiens* (Diptera: Culicidae), vectors of West Nile Virus in Illinois. *Am. J. Trop. Med. Hyg. 74,* 168–173.

Kuno, G., Chang, G.J., Tsuchiya, K.R., Karabatsos, N., and *Cropp, C.B.,* 1998: Phylogeny of the Genus Flavivirus. *J. Virol. 72*, 73–83.

Landesman, W.J., Allan, B.F., Langerhans, R.B., Knight, T.M., and *Chase, J.M.,* 2007: Inter-annual associations between precipitation and human incidence of West Nile Virus in the United States. *Vector Borne Zoonot. 7,* 337–343.

Lawrie, C.H., Uzcátegui, N.Y., Gould, E.A., and *Nuttall, P.A.,* 2004: Ixodid and argasid tick species and West Nile virus. *Emerg. Infect. Dis. 10*, 653–657.

L'vov, D.K., Dzharkenov, A.F., L'vov, D.N., Aristova, V.A., Kovtunov, A.I., Gromashevskii, V.L., Vyshemirskiĭ, O.I., Galkina, I.V., Al'khovskiĭ, S.V., Samokhvalov, E.I., Prilipov , A.G., Deriabin, P.G., Odolevskiĭ, E.I, and *Ibragimov, R.M.,* 2002: Isolation of the West Nile fever virus from the great cormorant *Phalacrocorax carbo*, the crow *Corvus corone*, and *Hyalomma marginatum* ticks associated with them in natural and synanthroic biocenosis in the Volga delta (Astrakhan region, 2001). *Vopr. Virusol. 47*, 7–12.

Meyer, R.; Hardy, J.; and *Reisen, W.,* 1990: Diel changes in adult mosquito microhabitat temperatures and their relationship to the extrinsic incubation of arboviruses in mosquitoes in Kern County, California. *J. Med. Entomol. 27,* 607–614.

Molnár, E., Gulyas, M. S., Kubinyi, L., Nosek, J., Kozuch, O., Ernek, E., Labuda, M., and *Grulich, I.,* 1975: Studies on the occurrence of tick-borne encephalitis in Hungary. *Acta. Vet. Acad. Sci. Hung. 26*, 419–437.

Moudy, R.M.; Meola, M.A.; Morin, L.L.L., Ebel, G.D., and *Kramer, L.D.,* 2007: A newly emergent genotype of West Nile Virus is transmitted earlier and more efficiently by *Culex* mosquitoes. *Am. J. Trop. Med. Hyg. 77*, 365–370.

Nasci, R.S., Savage, H.M., White, D.J., Miller, J.R., Cropp, B.C., Godsey, M.S., Kerst, A.J., Bennett, P., Gottfried, K., and *Lanciotti, R. S.,* 2001: West Nile virus in overwintering *Culex* mosquitoes, New York City, 2000. *Emerg. Infect. Dis. 7*, 742.

Pachler, K., Lebl, K., Berer, D., Rudolf, I., Hubalek, Z., and *Nowotny, N.,* 2014: Putative new West Nile virus lineage in *Uranotaenia unguiculata* mosquitoes, Austria, 2013. *Emerg. Infect. Dis. 20*, 12.

Pats, J. A., Githeko, A. K., McCarty, J. P., Hussain, S., Confalonieri, U., de Wet, N., 2003: Climate Change and infection Disease. In (Eds.: *McMichael, A.J., Campbell-Lendrum, D.H., Corvalán, C.F., Ebi, K.L., Githeko, A.K., Scheraga, J.D., Woodward, A.*) Climate Change and Human Health—Risks and Responses; WHO: Geneva, Switzerland, 103–132.

Paz, S., 2006: The West Nile Virus outbreak in Israel (2000) from a new perspective: The regional impact of climate change. *Int. J. Environ. Health Res. 16*, 1–13.

Paz, S. and *Albersheim, I.,* 2008: Influence of warming tendency on *Culex pipiens* population abundance and on the probability of West Nile Fever outbreaks (Israeli Case Study: 2001–2005). *EcoHealth 5*, 40–48.

Paz, S. and *Semenza, J.C.,* 2013: Environmental drivers of West Nile fever epidemiology in Europe and Western Asia—a review. *Int. J. Environ. Res. Public Health 10*, 3543–3562.

Paz, S., Malkinson, D., Green, M.S., Tsioni, G., Papa, A., Danis, K., Sirbu, A., Ceianu, C., Krisztalovics, K., and *Ferenczi, E.,* 2013: Permissive summer temperatures of the 2010 European West Nile Fever upsurge. *PloS One 8*, e56398.

Platonov, A.E., Fedorova, M.V., Karan, L.S., Shopenskaya, T.A., Platonova, O.V., and *Zhuravlev, V.I.,* 2008: Epidemiology of West Nile infection in Volgograd, Russia, in relation to climate change and mosquito (Diptera: Culicidae) bionomics. *Parasitol. Res. 103*, 45–53.

Reeves, W.C., Hardy, J.L., Reisen, W.K., and *Milby, M.M.,* 1994: Potential effect of global warming on mosquito-borne arboviruses. *J. Med. Entomol. 31*, 323–332.

Reisen, W.K., 1995: Effect of temperature on *Culex tarsalis* (Diptera: Culicidae) from the Coachella and San Joaquin Valleys of California. *J. Med. Entomol. 32*, 636–645.

Reisen, W.K., Fang, Y., and *Martinez, V.M.,* 2006: Effects of temperature on the transmission of West Nile virus by *Culex tarsalis* (Diptera: Culicidae). *J. Med. Entomol. 43*, 309–317.

Reiter, P., 2001: Climate change and mosquito-borne disease. *Environ. Health Perspect. 109(Suppl 1),* 141.

Roehr, B., 2012: US hit by massive West Nile Virus outbreak centred around Texas. *Brit Med J. 345,* e5633.

Ruiz, M.O., Chaves L.F., Hamer, G.L., Sun, T., Brown, W.M., Walker, E.D., Haramis, L., Goldberg, T. L., and *Kitron, U.D.* 2010: Local impact of temperature and precipitation on West Nile Virus infection in *Culex* species mosquitoes in Northeast Illinois, USA. *Parasites Vector. 3,* 1–16.

Russell, R.C., 1998: Mosquito-borne arboviruses in Australia: the current scene and implications of climate change for human health. *Int. J. Parasitol. 28*, 955–969.

Sambri, V., Capobianchi, M., Charrel R., Fyodorova, M., Gaibani, P., Gould, E., Niedrig, M., Papa, A., Pierro, A., Rossini, G., Varani, S., Vocale, C., and Landini, M.P., 2013: West Nile virus in Europe: emergence, epidemiology, diagnosis, treatment, and prevention. *Clin. Microbiol. Infect. 19*, 699–704.

Sampathkumar, P., 2003: West Nile virus: Epidemiology, Clinical presentation, Diagnostic, and Prevention. *Mayo Clin. Proc. 78,* 1137–1144.

Schäfer, M.L. and *Lundström, J.O.,* 2006: Different responses of two floodwater mosquito species, *Aedes vexans* and *Ochlerotatus sticticus* (Diptera: Culicidae), to larval habitat drying. *J. Vector Ecol. 31,* 123-128.

Shaman, J., Day, J.F., Stieglitz, M., 2005: Drought-induced amplification and epidemic transmission of West Nile Virus in Southern Florida. *J. Med. Entomol. 42,* 134–141.

Shaman, J., Stieglitz, M., Stark, C., Le Blancq, S., and *Cane, M., 2002:* Using a dynamic hydrology model to predict mosquito abundances in flood and swamp water. *Emerg. Infect. Dis*. *8,* 8–13.

Soverow, J.E., Wellenius, G.A., Fisman, D.N., and *Mittleman, M.A.,* 2009: Infectious disease in a warming world: How weather influenced West Nile Virus in the United States (2001–2005). *Environ. Health Perspect*. *117*, 1049–1052.

Szentpáli-Gavallér, K., Antal, L., Tóth, M., Kemenesi, G., Soltész, Z., Dán, A., Erdélyi, K., Bányai, K., Bálint, Á., Jakab, F., and *Bakonyi, T.,* 2014: Monitoring of West Nile virus in mosquitoes between 2011–2012 in Hungary. *Vector Borne Zoonotic Dis. 14*, 648–655.

Takeda T., Whitehouse, C.A., Brewer, M., Gettman, A.D., and *Mather, T.N.* 2003: Arbovirus surveillance in Rhode Island: Assessing potential ecologic and climatic correlates. *J. Am. Mosq. Control Assoc. 19*, 179–189.

Taylor, R.M., Work, T.H., Hurlbut, H.S., and *Rizk, F.,* 1956: A study of the ecology of West Nile virus in Egypt. *Am. J. Trop. Med. Hyg. 5*, 579–620.

Trájer, A. and *Hammer, T.,* 2016: Climate-based modeling of temperate malaria based on the epidemiological data of 1927-1934, Hungary. *Időjárás 120,* 331–351.

Trájer, A., Farkas-Iványi, K., and *Padisák, J.,* 2015: Area-based historical modeling of the effects of the river bank regulation on the potential abundance of eleven mosquito species in the River Danube between Hungary and Slovakia. *Adv. Oceanogr. Limnol. 6,* 1/2.

Trájer, A., Bede-Fazekas, Á., Bobvos, J., and *Páldy, A.,* 2014: Seasonality and geographical occurrence of West Nile fever and distribution of Asian tiger mosquito. *Időjárás 118*, 19–40.

Trájer, A., Bede-Fazekas, Á., Hufnagel, L., Horváth, L., and *Bobvos, J.,* 2013: The effect of climate change on the potential distribution of the European *Phlebotomus* species. *AEER 11*, 189–208.

Trawinski, P. and *Mackay, D.,* 2008: Meteorologically conditioned time-series predictions of West Nile Virus vector mosquitoes. *Vector Borne Zoonot. Dis*. *8,* 505–522.

Tsai, T.F. Popovici, F., Cernescu, C., Campbell, G.L., and *Nedelcu, N.I.,* 1998: West Nile encephalitis epidemic in southeastern Romania. *Lancet. 352*, 767–771.

Uejio, C.K., Kemp, A., and *Comrie, A.C.,* 2012: Climatic controls on West Nile Virus and Sindbis Virus transmission and outbreaks in South Africa. *Vector Borne Zoonot.Dis. 12,* 117–125.

Whelan, P.I., Jacups, S.P., Melville, L., Broom, A., Currie, B.J., Krause, V.L., Brogan, B., Smith, F, and *Porigneaux, P.,* 2003: Rainfall and vector mosquito numbers as risk indicators for mosquito-borne disease in Central Australia. *Commun. Dis. Intell. 27,* 110–116.

Work, T.H., Hurlbüt, H., and *Taylor, R.M.,* 1955: Indigenous wild birds of the Nile Delta as potential West Nile virus circulating reservoirs. *Am. J. Trop. Med. Hyg*. *4*, 872–888.

INSTRUCTIONS TO AUTHORS OF *IDŐJÁRÁS*

The purpose of the journal is to publish papers in any field of meteorology and atmosphere related scientific areas. These may be

- research papers on new results of scientific investigations,
- critical review articles summarizing the current state of art of a certain topic,
- short contributions dealing with a particular question.

Some issues contain "News" and "Book review", therefore, such contributions are also welcome. The papers must be in American English and should be checked by a native speaker if necessary.

Authors are requested to send their manuscripts to

Editor-in Chief of IDŐJÁRÁS
P.O. Box 38, H-1525 Budapest, Hungary
E-mail: journal.idojaras@met.hu

including all illustrations. MS Word format is preferred in electronic submission. Papers will then be reviewed normally by two independent referees, who remain unidentified for the author(s). The Editor-in-Chief will inform the author(s) whether or not the paper is acceptable for publication, and what modifications, if any, are necessary.

Please, follow the order given below when typing manuscripts.

Title page: should consist of the title, the name(s) of the author(s), their affiliation(s) including full postal and e-mail address(es). In case of more than one author, the corresponding author must be identified.

Abstract: should contain the purpose, the applied data and methods as well as the basic conclusion(s) of the paper.

Key-words: must be included (from 5 to 10) to help to classify the topic.

Text: has to be typed in single spacing on an A4 size paper using 14 pt Times New Roman font if possible. Use of S.I. units are expected, and the use of negative exponent is preferred to fractional sign. Mathematical formulae are expected to be as simple as possible and numbered in parentheses at the right margin.

All publications cited in the text should be presented in the *list of references*, arranged in alphabetical order. For an article: name(s) of author(s) in Italics, year, title of article, name of journal, volume, number (the latter two in Italics) and pages. E.g., *Nathan, K.K.,* 1986: A note on the relationship between photosynthetically active radiation and cloud amount. *Időjárás 90,* 10-13. For a book: name(s) of author(s), year, title of the book (all in Italics except the year), publisher and place of publication. E.g., *Junge, C.E.,* 1963: *Air Chemistry and Radioactivity.* Academic Press, New York and London. Reference in the text should contain the name(s) of the author(s) in Italics and year of publication. E.g., in the case of one author: *Miller* (1989); in the case of two authors: *Gamov* and *Cleveland* (1973); and if there are more than two authors: *Smith et al.* (1990). If the name of the author cannot be fitted into the text: *(Miller,* 1989); etc. When referring papers published in the same year by the same author, letters a, b, c, etc. should follow the year of publication.

Tables should be marked by Arabic numbers and printed in separate sheets with their numbers and legends given below them. Avoid too lengthy or complicated tables, or tables duplicating results given in other form in the manuscript (e.g., graphs).

Figures should also be marked with Arabic numbers and printed in black and white or color (under special arrangement) in separate sheets with their numbers and captions given below them. JPG, TIF, GIF, BMP or PNG formats should be used for electronic artwork submission.

More information for authors is available: journal.idojaras@met.hu

Published by the Hungarian Meteorological Service

Budapest, Hungary

INDEX 26 361

HU ISSN 0324-6329